Irradiated Model Atmospheres for Extrasolar Giant Planets and Secondary Stars of Pre-Cataclysmic Variables

by

Travis S. Barman

(Under the direction of Peter H. Hauschildt)

Abstract

Atmospheric models have been calculated for M dwarf stars found in post-common envelope binary systems and extra-solar giant planets (EGPs) which have very small orbital separations. In such systems, the radiation field from the hotter companion effects the atmosphere of the much cooler M dwarf or planet. The PHOENIX model atmosphere code has been adapted to explicitly include the extrinsic radiation in the solution of either the plane parallel or spherically symmetric radiative transfer equation *and* in the calculation of the temperature structure. The updated PHOENIX code also employs a new modified Unsöld-Lucy temperature correction procedure that is stable and ensures that energy conservation is satisfied even in the presence of strong extrinsic flux.

Irradiated planets located at various orbital separations from either a dM5 or a G2 primary star have been modeled for two extreme cases: one where dust clouds form and remain suspended in the atmosphere, and another where dust clouds form but completely settle out of the atmosphere. The atmospheric structure and emergent spectrum strongly depend on the presence or absence of dust clouds. It has also been demonstrated that neutral sodium is *not* in local thermodynamic equilibrium (LTE) in the outer atmosphere of irradiated EGPs.

Pre-cataclysmic variables (pre-CVs) containing a hot white dwarf (WD) and cool M dwarf have also been modeled. These models demonstrate that dramatic changes can occur in the atmosphere of an M dwarf secondary due to the incident flux from a WD primary. A large temperature inversion, similar in appearance to a chromospheric transition region, forms in the upper atmosphere of the secondary. Also, the effects of irradiation have been shown to vary across the surface of the secondary leading to distinct spectra at different orbital phases and inclinations.

Index words: Stars, Planetary Systems, Radiative Transfer, Atmospheres

Irradiated Model Atmospheres for Extrasolar Giant Planets and Secondary Stars of Pre-Cataclysmic Variables

by

Travis S. Barman

B.S., The University of Georgia, 1996

A Dissertation Submitted to the Graduate Faculty

of The University of Georgia in Partial Fulfillment

of the

Requirements for the Degree

Doctor of Philosophy

Athens, Georgia

2002

Irradiated Model Atmospheres for Extrasolar Giant Planets and Secondary Stars of Pre-Cataclysmic Variables

by

Travis S. Barman

Approved:

Major Professor: Peter H. Hauschildt

Committee: France Allard
Loris Magnani
Heinz-Bernd Schüttler
James Scott Shaw
Phillip C. Stancil

Electronic Version Approved:

Gordhan L. Patel
Dean of the Graduate School
The University of Georgia
May 2002

Acknowledgments

I'd like to thank all y'all!

Table of Contents

Chapter 1

Introduction

For many years astronomers have been obtaining a wealth of information about stellar and substellar objects by comparing observed spectra to synthetic spectra from detailed model atmosphere calculations. Such comparisons are often the only method for inferring the chemical composition and temperatures in a stellar atmosphere. However, nearly all model atmosphere calculations ignore extrinsic radiation and, therefore, are not as useful when studying close binary or planetary systems.

The conditions in a stellar or planetary atmosphere depend primarily on the available energy sources and how the energy is absorbed and reradiated. Many binaries have orbital separations small enough so that irradiation by one binary member is a significant source of energy for the atmosphere of its companion. The effects of irradiation are especially important for objects which receive an *extrinsic* flux that is comparable to or larger than the *intrinsic* flux they produce (i.e. $f \equiv \mathrm{F}_{\mathrm{ext}}/\mathrm{F}_{\mathrm{int}} \geq 1$). For atmospheres with very large values of f, the properties of the irradiated atmosphere become less dependent upon its own internal energy sources and more dependent upon the properties of the external source. Perhaps the most obvious examples of objects which receive more extrinsic flux than they produce are found in our own solar system. Each of the nine planets experience some degree of irradiation by the Sun and, in the case of Jupiter[1], $f \sim 3$. Other examples are Symbiotic binaries

[1] Note that Jupiter actually appears to emit twice as much radiation as it receives from the Sun. However, only $\sim 50\%$ of this radiation is actually intrinsic to Jupiter. In the definition of f, $\mathrm{F}_{\mathrm{int}}$ refers *only* to the flux due to intrinsic energy sources and does not include any reflected or reprocessed radiation.

(Schwank et al., 1997), Algol systems (Claret & Gimenez, 1992), and closely separated red dwarf – white dwarf pairs (Marsh, 2000). This dissertation focuses on modeling the atmospheres for two types of systems where irradiation is important, extra-solar giant planets and pre-Cataclysmic Variables.

1.1 Extrasolar Giant Planets

The existence of planets outside our solar system has preoccupied the imaginations of people for centuries. In 1992, the first extrasolar planets were discovered in a surprising location; orbiting the 6.2-ms pulsar PSR1257+12 (Wolszczan & Frail, 1992). Though far from being a solar system analogue, the pulsar planets indicated that, perhaps, planet formation is not as rare as previously suspected.

Using very precise spectrographs capable of detecting Doppler shifts on the order of 10 m sec^{-1}, astronomers observed hundreds of stars for more than a decade with the hope of detecting planet sized or Brown Dwarf (BD) companions around solar type stars. In 1995, it was finally announced that one star, 51 Pegasi, exhibited a periodic change in radial velocity (RV) due to the gravitational pull of a previously undetected Jupiter-mass companion (Mayor & Queloz, 1995). Thus, 51 Peg b became the first extrasolar *giant* planet (EGP) to be discovered[2].

Numerous precise radial velocity surveys, inspired by the discovery of 51 Peg b, are now being carried out and currently over 2000 late F, G, and K type stars are being monitored. Three surveys underway at the Keck, Lick and Anglo-Australian observatories currently achieve Doppler precision of 3 m sec^{-1} which allows the detection of a 0.5 M_J ($1M_J = 2 \times 10^{30}$ grams, the mass of Jupiter) planet with orbital separation out to 2 AU ($1AU = 1.5 \times 10^{13}$ cm, the average Earth-Sun separation). Over 70 extrasolar giant planets (EGPs) have now been detected with the RV method

[2]The first Brown Dwarf was also discovered in the same year (Oppenheimer et al., 1995).

Table 1.1: Examples of EGPs and their properties.

Star Name	M sin(i) (M$_{jup}$)	Period (days)	semi-major axis (AU)	eccentricity
HD83443b^m	0.35	2.986	0.04	0.08
HD46375	0.25	3.024	0.04	0.02
HD179949	0.93	3.092	0.04	0.00
HD187123	0.54	3.097	0.04	0.01
Tau Boo	4.14	3.313	0.05	0.02
BD-103166	0.48	3.487	0.05	0.05
HD75289	0.46	3.508	0.05	0.01
HD209458	0.63	3.524	0.05	0.02
51Peg	0.46	4.231	0.05	0.01
UpsAndb^m	0.68	4.617	0.06	0.02
HD68988	1.90	6.276	0.07	0.14
HD168746^m	0.24	6.400	0.07	0.00
HD217107	1.29	7.130	0.07	0.14
HD130322	1.15	10.720	0.09	0.05
HD108147	0.35	10.880	0.10	0.56
HD38529	0.79	14.310	0.13	0.12
55Cnc	0.93	14.660	0.12	0.03
GJ86	4.23	15.800	0.12	0.04
HD192263	0.81	24.350	0.15	0.22
HD83443c^m	0.17	29.830	0.17	0.42
GJ876c^m	0.56	30.120	0.13	0.27
HD74156b^m	1.55	51.600	0.28	0.65
HD168443b^m	7.64	58.100	0.29	0.53
GJ876b^m	1.89	61.020	0.21	0.10
HD178911B	6.46	71.500	0.33	0.14
HD16141	0.22	75.800	0.35	0.00
70Vir	7.42	116.700	0.48	0.40
HD82943c^m	0.88	221.600	0.73	0.54
UpsAndc^m	2.05	241.300	0.83	0.24
HD82943b^m	1.63	444.600	1.16	0.41
47UMab^m	2.56	1090.500	2.09	0.06
UpsAndd^m	4.29	1308.500	2.56	0.31
HD74156c^m	7.46	2300.000	3.47	0.40
47UMac^m	0.76	2640.000	3.78	0.00

m – multiple systems
Values taken from `http://exoplanets.org/`.

(see table 1.1 for a list of examples). The results, somewhat surprisingly, indicate that $\sim 1\%$ of solar type stars harbor "51 Peg b-like" planets (also called Pegasi Planets) and that $\sim 7\%$ of solar type stars have Jupiter-mass companions with eccentric orbits ($e > 0.2$) between 0.1 and 4 AU from their parent star (Butler et al., 2001). Even with the small number of EGPs detected thus far, it is reasonable to conclude that our galaxy, with over 200 billion stars, harbors more than a billion planets.

The periodic Doppler shifts that are observed in RV surveys only provide a measure of the orbital motion projected onto the line-of-sight (LOS), and the inclination (i) of the orbital plane is generally not known. Therefore, only a lower limit, $\mathrm{M_p}\sin(\mathrm{i})$, for the planet mass ($\mathrm{M_p}$) is obtained. However, if orbital inclinations are randomly distributed between 0 and $\frac{\pi}{2}$, then only about 1 out of 10 EPGs will have a mass larger than twice $\mathrm{M_p}\sin(\mathrm{i})$ (Burrows et al., 2001). A histogram of $\mathrm{M_p}\sin(\mathrm{i})$ for all currently known EGPs (an updated list is maintained at `http://cfa-www.harvard.edu/planets`) is shown in figure 1.1. The distribution follows a power law ($\mathrm{N} \propto 1/\mathrm{M_p}$) and is strongly peaked at $1\mathrm{M_J}$ (Marcy et al., 2000). Although BDs are now known to be common and the RV method should have detected them, few BD companions (i.e. $13 < \mathrm{M} < 75\mathrm{M_J}$) have been found. The majority of EGPs have orbits with semi-major axis (a) less than 1AU and nearly one third have a less than 0.1AU (see Fig. 1.1). The low number of planets with $a > 1$AU could very well be due to selection effects; the RV method preferentially reveals more massive planets (large radial velocities) with very small orbits (large radial velocities and short periods). However, the excess of EGPs with $a < 0.2$AU and so few with a between 0.2 and 0.6AU can not be explained purely by selection effects since $a < 0.6$AU is easily detected with the current sensitivity of RV surveys (Butler et al., 2001).

Because most EGPs have been discovered orbiting G type main sequence stars and have such small orbital separations, many of these planets are subjected to

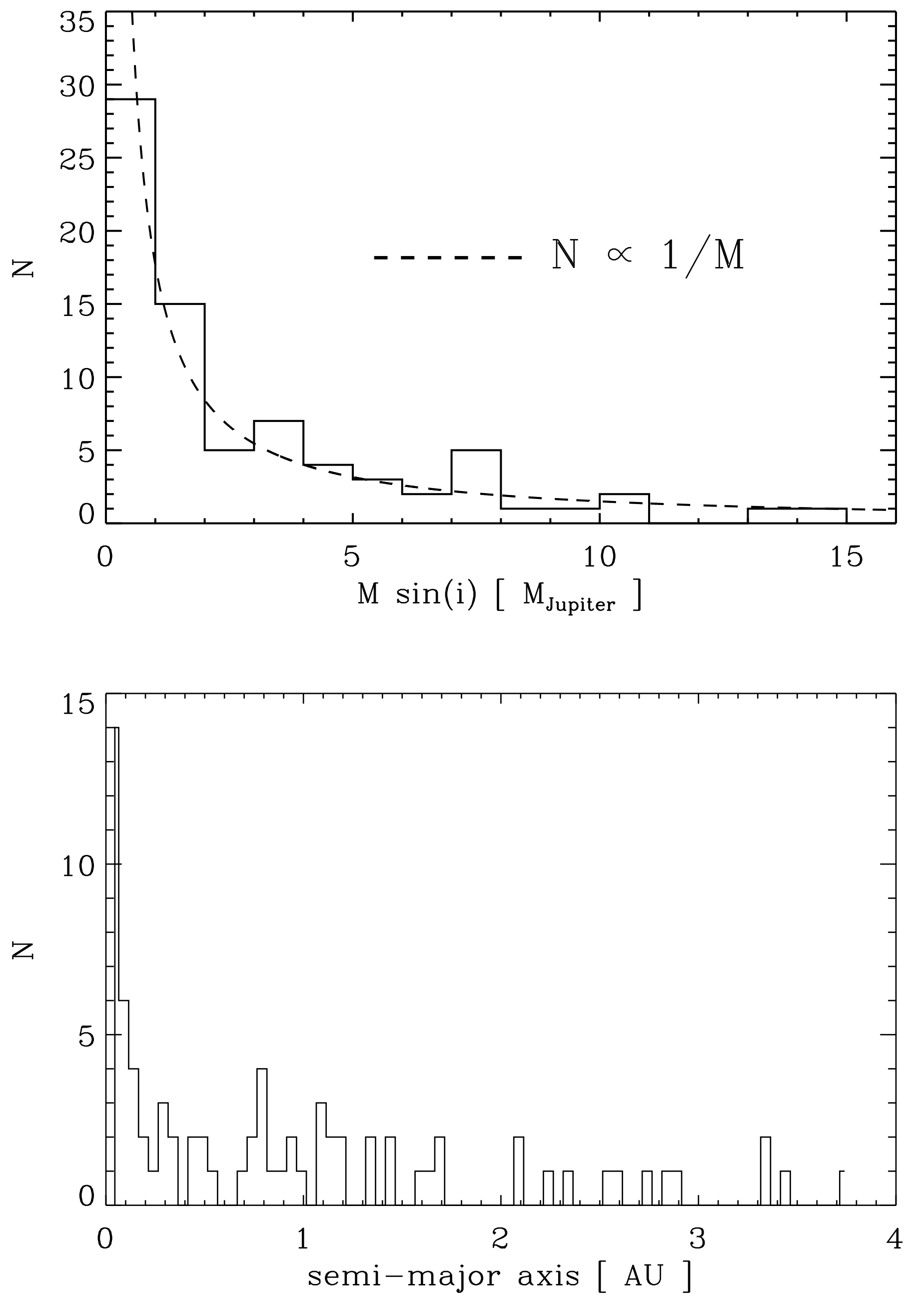

Figure 1.1: Top: mass histogram with best fitting power-law (dashed line). Bottom: orbital separation (semi-major axis) histogram.

intense stellar radiation that is more than 100 times what the Earth receives from the Sun. If EGPs are truly like Jupiter, then the extrinsic luminosity they receive from their parent star is likely to be 10^4 times greater than their intrinsic luminosity. Even if EGPs absorb only half of the incident flux they receive, energy conservation implies that EGPs with $a = 0.05$AU will have dayside surface temperatures greater than 1000K and their bolometric luminosity will be comparable to field BDs ($\mathrm{L/L_\odot} \leq 10^{-2}$). Therefore, EGPs are likely to have atmospheric temperatures and opacity sources (i.e. molecules and, possibly grains) similar to those found in isolated BDs. However, due to the extrinsic nature of the primary energy source, EGPs will have temperature and chemical abundance profiles (as a function of depth) that are distinct from what theory predicts for isolated BDs.

Probably the best studied EGP is HD209458b, the first and, so far, the only one observed to transit its parent star. As an eclipsing system, the orbital plane is nearly edge-on with $\sin(i) \sim 1$. Also, during each transit event, the bolometric flux from the star is reduced by an amount proportional to $\frac{A_p}{A_s}$, where $\mathrm{A_s}$ and $\mathrm{A_p}$ are the surface areas of the star and planet, respectively. Therefore the radius of HD209458b can be measured to high accuracy; $\mathrm{R_P} = 1.347\mathrm{R_J}$, where $\mathrm{R_J}$ ($= 7.15 \times 10^9$cm) is one Jupiter radius (Brown et al., 2001). Using the mass and radius, and assuming a spherical planet, an estimate for the mean density and surface gravity yields values which are comparable to those of Jupiter implying that HD209458b is indeed a gas giant (Charbonneau et al., 1999). However, the large radius of HD209458b is hard to reconcile with the current estimates for the age of HD209458b (2 – 6 Gyrs, Mazeh et al, 2000) and evolution models for Brown Dwarfs and the giant planets of our solar system (which predict a radius roughly 30% smaller).

HD209458b has a short period and orbits a star very similar to our Sun, but with an orbital separation 100 times closer than the Jupiter-Sun distance. It is among the more severe cases of irradiated planets and, therefore, will have very high atmospheric temperatures compared to an isolated Jovian planet. Guillot et al. (1996) suggested that irradiation may act as an insulation mechanism that reduces the normal cooling timescale of irradiated planets, thereby slowing their contraction. More recent calculations indicate that a small amount ($\sim 1\%$) of incident energy must also be dissipated into the planet's interior to fully explain the large radius (Guillot & Showman, 2002). However, a self-consistent evolution model with boundary conditions appropriate for short period EGPs still needs to be calculated (Baraffe et al., 2002).

Over the next two decades, various methods besides RV will begin revealing new planets and new information about previously detected planets. Ground based efforts to measure the stellar light reflected by planets are already underway (Charbonneau et al., 1999; Cameron et al., 1999). KEPLER, a spaced based telescope scheduled to launch in 2006, will simultaneously monitor $\sim 100,000$ stars (105 deg^2 of the sky) to search for transits of solar type stars by earth-sized planets (Koch et al., 2001). Also, several groups are currently searching for gravitational lensing events due to planets (e.g., MOA, MACHO, OGLE, and EROS). A series of space-based infrared interferometers such as SIM (Unwin & Shao, 2000), TPF (Nisenson & Papaliolios, 2001), and Darwin (Ollivier et al., 2000) will be launched in the next 15 years which should provide direct images and spectra of EGPs. As data from these missions become available, there will be a high demand for models of irradiated planets, and comparisons between observed and synthetic spectra will greatly improve our understanding of EPGs. For a more thorough introduction to EGPs and detection methods, the reader is refered to Perryman (2000).

1.2 pre-Cataclysmic Variables

Other types of multiple systems where irradiation is important are highly evolved binary stars. In the standard picture of binary star evolution, two companions evolve off the zero-age main sequence (ZAMS) in a manner similar to isolated stars. The initially more massive star will be the first to evolve off the ZAMS toward the giant branch. As its radius increases, the star becomes a giant and overfills its roche lobe forming a common envelope (CE) around the binary. Theory predicts that the CE will not co-rotate with the binary leading to frictional drag that transfers angular momentum from the binary to the CE. As angular momentum is transferred, the binary orbit shrinks while the CE heats up. Eventually, the CE is ejected producing a planetary nebula[3] (PN) surrounding a detached, closely separated, binary consisting of a white dwarf (WD) or luminous sub-dwarf (sdOB) and a main sequence (MS) companion (Paczynski, 1976). In less than 10^6 years after forming, the PN will disperse. In most cases, the sdOB will evolve into a WD and, depending on the mass of the MS star, the system may further evolve into one of the many types of cataclysmic variables (CVs) or low mass X-ray binaries (LMXBs). Post-CE binaries that are detached and do not transfer mass are often labeled pre-CVs, regardless of whether they can evolve into a CV within a Hubble time. For this work, the pre-CV label will be restricted to detached sdOB+MS or WD+MS binaries that could possibly become a CV within a Hubble time; i.e. those with orbital periods less than 16 days (Hillwig et al., 2000).

The properties of many, but not all, of the known pre-CVs are listed in table 1.2. The majority of pre-CVs have periods longer than 6 hours while the majority of CVs have periods shorter than 6 hours (see fig. 1.2). This dichotomy exists because CVs are old enough for gravitational wave radiation and magnetic breaking to have

[3]Planetary nebula is a misnomer left over from early astronomy and has nothing to do with planets.

Table 1.2: Probable Post-Common Envelope Binaries

Star Name	Period (hr)	M_1 ($M_\odot$)	M_2 ($M_\odot$)	T_{wd} (K)	Semi-Major axis ($R_\odot$)
GD 448	2.473	0.41 ± 0.01	$0.096 \pm .004$	...	0.737
MT Ser	2.717	$0.6 :$	0.2 ± 0.1	$50,000$	0.914
HW Vir	2.801	0.54 ± 0.09	0.16 ± 0.03	$36,500$	0.892
NN Ser	3.122	0.54 ± 0.07	0.12 ± 0.03	...	0.940
GD 245	4.168	0.48 ± 0.02	0.22 ± 0.02	$22,170$	1.163
Feige 36	4.940	$0.5 :$	> 0.42	...	1.426
PG 1224+309	6.208	0.45 ± 0.05	0.28 ± 0.05	$29,300$	1.538
AA Dor	6.277	0.25 ± 0.05	0.043 ± 0.005	$40,000$	1.143
CC Cet	6.823	0.40 ± 0.11	0.18 ± 0.05		1.517
RR Cae	7.289	0.467	0.095	$7,000$	1.569
GK Vir	8.264	0.51 ± 0.04	0.10	...	1.753
KV Vel	8.571	0.55 ± 0.15	0.25 ± 0.06	...	1.966
UU Sge	11.162	0.63 ± 0.06	0.29 ± 0.03	$87,000$	2.456
V477 Lyr	11.321	0.51 ± 0.07	0.15 ± 0.02	...	2.219
V471 Tau	12.508	0.76 ± 0.02	0.73 ± 0.03	$32,400$	3.112
HZ 9	13.544	0.51 ± 0.10	0.28 ± 0.04	$22,000$	2.656
UX CVn	13.769	0.39 ± 0.05	0.42	$28,000$	2.707
PG 1026+002	14.334	0.68 ± 0.23	0.22 ± 0.05	...	2.880
G 203-47	14.714	$0.5 :$	$> 0.2(M3.5)$	...	2.696
EG UMa	16.023	0.38 ± 0.07	0.26 ± 0.04	$13,000$	2.769
RE 2013+400	16.932	0.57 ± 0.1	0.19	$48,000$	3.042
RE 1016-053	18.943	0.61 ± 0.1	0.16	$55,400$	3.293
Abell 65	24.000	...	...	$80,000$	...
IN CMa	24.500	$0.49 - 0.62$	$0.49 - 0.79$	$52,400$	4.236
HD 49798	37.144	1.75 ± 1.0	$1.75 :$	...	6.443
BE UMa	54.988	0.70 ± 0.07	0.36 ± 0.07	$105,000$	7.454
PG 1538+269	60.020	$0.5 :$	> 0.68	$25,200$	8.190
HD 33959C	90.960	$1.0 :$	1.8	...	9.493
Feige 24	101.558	0.47 ± 0.03	0.295 ± 0.035	...	10.065
FF Aqr	220.987	0.5	2.0	...	14.668
V651 Mon	383.784	0.40 ± 0.05	1.8 ± 0.3	$100,000$	28.374

Adapted from the compilation of Hillwig et al. (2000). M_1 and M_2 are, respectively, the masses of the white dwarf and main sequence star. T_{wd} is the effective temperature of the white dwarf and the last column, semi-major axis, is the average orbital separation of the binary. See Hillwig et al. (2000) for references pertaining to each object.

further reduced the size of their orbits. However, pre-CVs have only recently emerged from the CE phase and their orbits have not had enough time to significantly degrade (de Kool & Ritter, 1993).

As is the case for EGPs, the orbital inclination is not easily measured. Fortunately, several methods have been developed for determining the properties of pre-CV members. In a few cases, a gravitational redshift induced by the WD's strong gravitational field can be measured and, when combined with mass-radius relationships from stellar evolution calculations, can be used to determine the WD mass. If the UV or Optical spectrum of the WD is available, then the surface gravity and effective temperature[4] ($T_{\rm eff}$) can be determined from the continuum and the shape of the Lyman or Balmer lines. The WD mass is then obtained by comparing the temperature and gravity values to WD cooling tracks provided by stellar evolution calculations. In some cases, emission lines can help place limits on the inclination which can in turn be used to estimate the individual masses. Once the mass of one component is known, the ratio of the radial-velocity amplitudes is used to determine the mass of the second component. The average masses in pre-CVs are about $0.5M_\odot$ for the WD and about $0.2M_\odot$ for the MS star. With the masses and periods known, the orbital separation can be determined from Kepler's third law. The shortest period pre-CV, GD 448, has a semi-major axis of only $0.74R_\odot$; which is roughly 10 times smaller the than the semi-major axes of the shortest period EGPs.

The WDs found in pre-CVs have effective temperatures ranging from $\sim 10,000$K to 100,000K with the average being 45,000K. Also, WDs are very compact objects with large surface gravities ($\sim 10^8$ cm sec^{-2}) and small radii ($\sim 10^9$ cm). So, despite the high temperatures of pre-CV WDs, their small size prevents them from being very bright. Even Sirius B, which has $T_{\rm eff} = 25,000$K and is the closest WD to

[4]$T_{\rm eff}$ is the temperature of a blackbody that radiates the same integrated energy flux as a particular star.

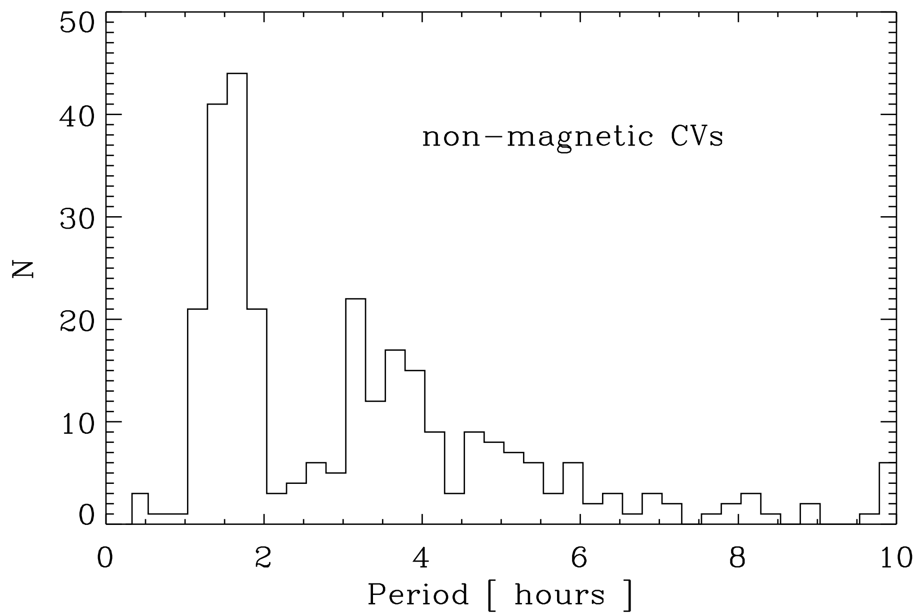

Figure 1.2: Distribution of periods for non-magnetic CVs. The period data is from the compilation of Ritter & Kolb (1998).

Earth, only shines with a visual magnitude of 8.3. For comparison, a WD with $T_{\rm eff} = 50,000$K and a typical WD radius ($\sim 10^9$cm) has a luminosity roughly equal to that of the Sun. For most CVs and pre-CVs, the total flux received by the cool MS star is very close to what the shortest period EGPs receive from their solar type parent star. However, the incident flux from the WD peaks in the UV to EUV rather than in the optical.

The most significant difference between EGPs and post-CE binaries is the intrinsic effective temperature of the irradiated MS star which is generally around 2500K – 3500K. Therefore, in the average pre-CV, the extrinsic luminosity is nearly equal to the intrinsic luminosity of the MS stars, while EGPs can have $F_{\rm ext}/F_{\rm int}$ as large as 10,000. The higher intrinsic effective temperatures in CV secondaries also imply that different opacity sources will be important compared to those found in EGPs (i.e. little, if any, condensation occurs).

The theory of CE and post-CE evolution is still not well understood; partly due to the low number of pre-CV candidates and mostly due to the lack of detailed knowledge about both binary members, especially the irradiated MS star. Nearly all of the pre-CVs listed in table 1.2 are observed to have emission lines originating from the MS star which cannot be attributed to an accretion disk or chromospheric activity (Hillwig et al., 2000, and references therein). It is generally accepted that these lines are induced by irradiation and, therefore, make pre-CVs excellent choices for studying the conditions in irradiated atmospheres. Reliable atmospheric models of pre-CVs that include irradiation will make it possible to better determine the properties (masses, radii, inclination, chemical composition, etc.) of post-CE binaries and improve evolution models.

1.3 Dissertation Outline

The following dissertation is strongly motivated by the need for atmospheric models that may be directly compared to observations of irradiated stellar and substellar binary members. Partial measurements of the conditions within EGP atmospheres are already becoming available and a high demand for theoretical comparisons and predictions already exists. Similarly, a need for models of pre-CVs has existed for many years. Hopefully, this work will help fill some of the gaps in our understanding of irradiation in two, seemingly unrelated, classes of objects – pre-CVs and EGPs.

The basic theory and methods used to model irradiated atmospheres will be described in chapter 2. Chapter 3 explores the properties of a broad range of irradiated EGPs while chapter 4 deals with a specific case, HD209458b. The general properties of the irradiated MS stars in pre-CVs are discussed in chapter 5 along with comparisons to observations of a particular pre-CV, GD 245. A summary of results is presented in chapter 6.

Chapter 2

Modeling Irradiated Atmospheres

Most binary systems have orbital separations that are large enough so that the *only* significant interaction between the two is gravitational. However, in all systems where the dimensions of the components are comparable to their separation, the radiation field of one component will influence that of the other. This "irradiation effect" (also known as the reflection effect) has been recognized, for many decades, to play an important role in close binary star systems (e.g., pre-CVs), our own solar system and, more recently, in extra-solar planetary systems. The first theoretical study of irradiation was performed by Eddington (1926) who pointed out that all of the incident radiation must be absorbed and re-emitted as thermal radiation (or scattered light). Therefore, the "heat-albedo" (also known as the bolometric albedo) is identically one for purely radiative atmospheres. Eddington (1926) also pointed out that the interior of a star should not be altered by irradiation. Most later works that dealt with irradiation focused on the construction of synthetic light curves for close binaries and irradiation was simply treated as a correction to the bolometric flux. For a complete review of the efforts to understand and model the irradiation effect in stars prior to 1985, the reader is referred to the review by Vaz (1985).

In the past 15 years, many improvements have been made in the modeling of binary stars and the construction of synthetic light curves. Recently, model atmospheres have been used to better describe the monochromatic flux (or at least narrow bands) of binary systems (Orosz & Hauschildt, 2000). The treatment of irradiation in model atmospheres has also progressed steadily over the years and several important achievements have been made. The first convective non-grey irradiated atmospheres were produced by Nordlund & Vaz (1990) who demonstrated that, for convective atmospheres, the same entropy at depth must be maintained if irradiated and non-irradiated atmospheres are to describe the night and day sides of the same star. A consequence of entropy matching is that the heat-albedo will be less than one and will depend on the efficiency of convection. Nordlund & Vaz (1990) also demonstrated that the presence of absorption lines in the incident spectrum and the orientation of these lines with respect to those in the spectrum of the irradiated star can play an important role in determining the atmospheric structure. The first irradiated atmospheres below 4000K were calculated for cool M dwarfs ($3000 - 3500$K) located very close to a $10,000$K blackbody (Brett & Smith, 1993) (here after the BS93 models). The BS93 models confirmed the basic results of Nordlund & Vaz (1990) and also demonstrated that horizontal energy flow is likely to be important in irradiated atmospheres.

Since the discovery of EGPs in 1995, there have been several studies of irradiation in the atmospheres of Jovian (i.e. Jupiter-like gas giants) atmospheres. An early investigation into the properties of EGPs for various masses and ages near primaries of different spectral types, using the gray approximation, showed that strong irradiation can alter the evolution of EGPs leading to a larger radius (as a function of age) compared to isolated EGPs (Saumon et al., 1996). Several works demonstrated that EGPs will have atmospheric structures that are very different from isolated gas giants and that large amounts of reflected light will dominate the optical spectrum (Seager & Sasselov, 1998; Goukenleuque et al., 2000). Also, a broad range ($100 - 1700$K) of EGP models were produced by Sudarsky et al. (2000) using ad hoc temperature-pressure profiles.

Many of these earlier model calculations were limited to plane-parallel geometry and, in some instances, did not satisfy energy conservation. In addition, these earlier model atmosphere calculations suffered from inaccurate and incomplete opacity sources. Opacity distribution functions (ODFs) or straight mean (SM) opacities were often used. These crude opacities were scaled to give the correct wavelength integrated opacity but were insufficient for high resolution spectrum synthesis. As a result, both the impinging radiation and the spectrum of the irradiated star lacked many important atomic and molecular features. Over the past decade, large atomic and molecular linelists have been steadily produced and calculations of detailed line-blanketed models for broad ranges in temperature are now possible.

This work attempts to overcome the inadequacies of previous efforts by (1) taking advantage of the most up-to-date and extensive set of opacities currently available for the modeling of both the extrinsic and intrinsic radiation fields, (2) developing a temperature correction procedure that allows energy conserving models to be calculated, (3) explicitly including the incident flux in the solution of the atmosphere problem in a self-consistent (i.e. energy conserving) manner, (4) employing spherical geometry for certain cases, and (5) producing high resolution spectra that can be directly compared to observations.

2.1 The General Model Atmosphere Problem

The general model atmosphere problem involves a self-consistent solution of many coupled physical and chemical problems with the ultimate goal of describing all of an atmosphere's properties at any given time. The solution to such a complex problem is beyond our present capabilities and requires simplifying approximations which make the problem more tractable while still providing insight into the real situation. Analytic solutions to model atmospheres exist for only extremely simplified cases that usually do not come close to describing any real atmosphere (though are still useful for pedagogical and testing purposes). Numerical simulations, therefore, provide us with our only means of producing realistic models that can be directly compared to observations.

The current, state-of-the-art, model atmosphere codes treat the atmosphere as a one-dimensional collection of homogeneous semi-infinite plane parallel slabs or spherically symmetric concentric shells. The plane parallel approximation is considered to be appropriate if the mean free path of a photon is much smaller than the thickness of the atmosphere which is, in turn, much smaller than the overall radius. For the objects considered below (e.g., EGPs and M dwarfs) these criteria are often satisfied. However, the spherically symmetric approximation will become important for calculating the transmitted spectrum for eclipsing EGPs (e.g., HD209458b); this will be discussed further in chapters 3 and 4.

The structure of a model atmosphere is often governed by two assumptions. First, the atmosphere is assumed to be in hydrostatic equilibrium and, as such, must have a pressure gradient to support itself. Therefore,

$$\nabla P(r) = -\rho(r) g, \tag{2.1}$$

where P is the gas pressure, ρ is the density, r is the radial coordinate (with origin at the center of the star or planet), and g is the gravitational acceleration ($g(r) = GM/r^2$). Second, the atmosphere is assumed to be in thermal equilibrium and conserves energy. Therefore, the gradient of the flux must be zero;

$$\begin{aligned} \nabla \left[F(r)_{\text{radiative}} + F(r)_{\text{convective}}\right] = 0 \\ \Longrightarrow F(r) = \left[F(r)_{\text{radiative}} + F(r)_{\text{convective}}\right] = \text{constant}. \end{aligned} \tag{2.2}$$

The flux constancy of the atmosphere is also used to define an *effective* temperature of the atmosphere, $\sigma \mathrm{T}_{\text{eff}}^4 = F$. Both T_{eff} and g are often used as model parameters.

The complexity of the model atmosphere problem is greatly reduced if one assumes the material in each layer is in *local thermodynamic equilibrium* (LTE).

In the LTE limit, the chemical equilibrium, ionization fraction and level populations for each species are completely determined by the local gas temperature and electron pressure at a specific layer. Decoupling the local state of the material from the depth dependent radiation field can be a very bad approximation in a variety of different environments (e.g., novae, white dwarfs, supernovae). However, in conditions where the level populations and ionization of atoms and molecules are mostly determined by collisional processes, the LTE assumption is valid. This assumption will be tested in chapter 5 for a particular EGP.

2.1.1 Radiative Transfer

The time independent one dimensional plane parallel radiative transfer equation (PPRTE) and the spherically symmetric radiative transfer equation (SSRTE) are:

$$\begin{aligned} &\text{PPRTE:} \qquad && \mu\frac{dI_\nu}{dr} = \chi_\nu(S_\nu - I_\nu) \\ &\text{SSRTE:} \qquad && \mu\frac{\partial I_\nu}{\partial r} + \frac{1-\mu^2}{r}\frac{\partial}{\partial \mu}I_\nu = \chi_\nu(S_\nu - I_\nu) \end{aligned} \tag{2.3}$$

with the following definitions:

- $\mu = \cos\theta$, where θ is the angle between I_ν and the vector normal to the surface.
- I_ν is the specific intensity with frequency ν and direction μ.
- χ_ν is the extinction coefficient.
- $d\tau_\nu = -\chi_\nu dr$. τ_ν is the optical depth and r is the physical depth with origin at the center of the object. Note that r increases as τ decreases.
- S_ν is the source function.
- B_ν is the Planck function.
- $J_\nu = \frac{1}{2}\int_{-1}^{1} I_\nu d\mu$ is the mean intensity.

The solution to either the PPRTE or the SSRTE is carried out along many characteristic rays at discrete values of τ and many different frequency points. Since the source function depends on the specific intensity, the RTE is often solved iteratively by applying successive corrections to the intensity (or the mean intensity) until a desired accuracy is achieved. The ability to converge upon the correct solution depends heavily on the iteration scheme used, and a classical Λ-iteration will not work (Mihalas, 1970). By far the most efficient method is the accelerated lambda iteration (ALI) method (Cannon, 1973; Olson & Kunasz, 1987; Rybicki & Hummer, 1991; Hauschildt, 1992).

Since the RTE depends on the opacity (χ_ν), the equation of state (EOS) and RTE must be solved simultaneously subject to the constraints mentioned above (eqs. 2.1 and 2.2). Thus, the entire model atmosphere problem must also be solved by iteration. Once the mass, radius, $T_{\rm eff}$ and chemical abundances are specified, the model atmosphere problem is well defined and a specific situation may be modeled. At the beginning of the first model iteration, an initial guess for the temperature structure is given or, if one is not available, obtained from the grey approximation. With this temperature structure, the EOS and RTE are solved and the energy conservation constraint is tested. If the total energy is not conserved within a prescribed accuracy, a correction to the temperature at each layer is made so that the source function produces the correct flux. The process is repeated until the temperature corrections are small and the total energy is well conserved. The overall iteration scheme is shown in figure 2.1.

2.2 The PHOENIX Model Atmosphere Code

`ATLAS` (Kurucz, 1996), `TLUSTY` (Hubeny, 1988), `UMA` (Gustafsson et al., 1975), and `PHOENIX` (Hauschildt & Baron, 1999) are just a few of the popular atmosphere codes

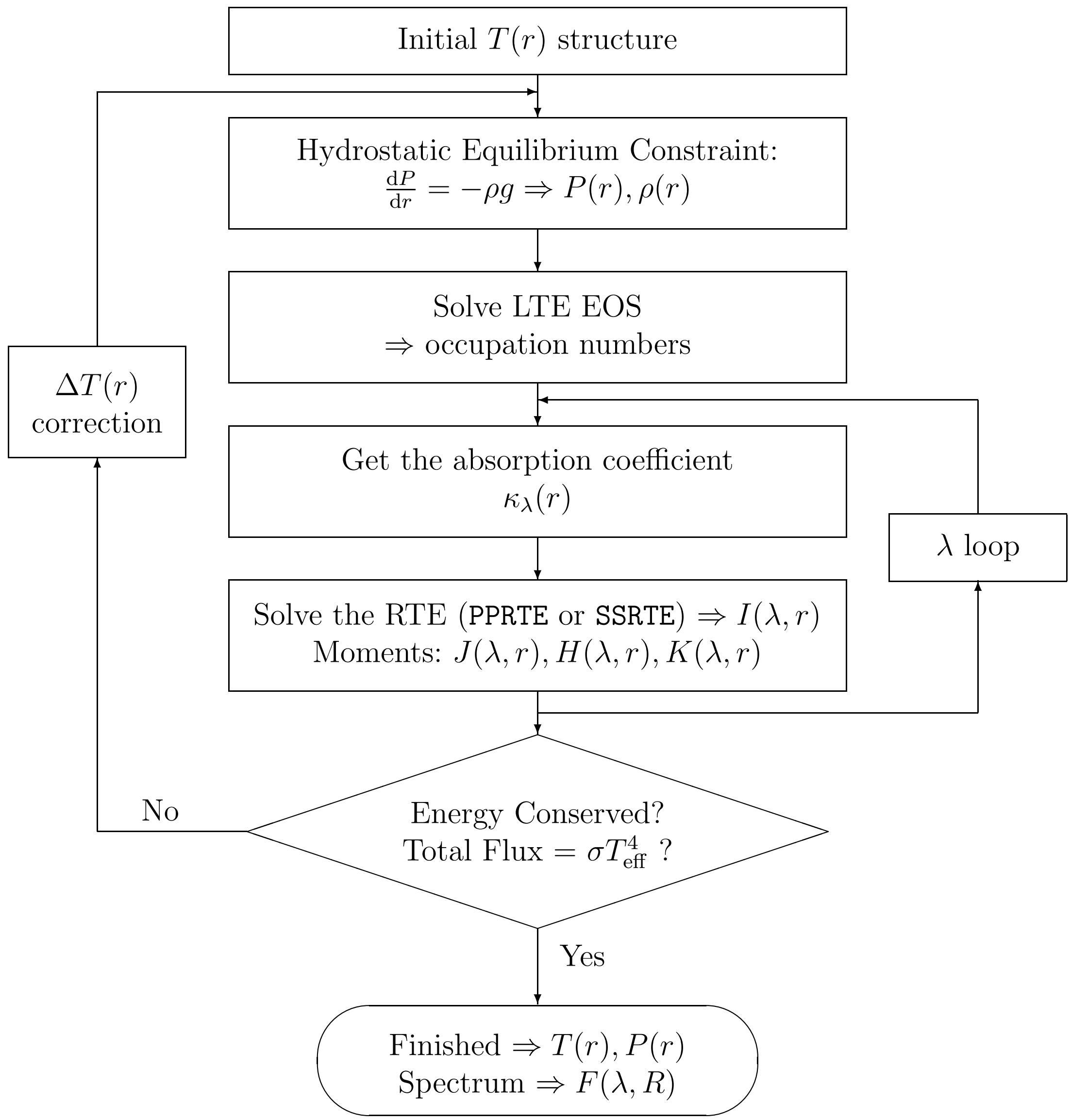

Figure 2.1: A flowchart describing the basic method for solving the LTE model atmosphere problem (adapted from Schweitzer, 1999). Note that r is the radial coordinate with $r = 0$ at the center and $r = R$ at the surface.

currently used in astrophysics today. Each of these codes follow the same physical recipe for building model atmospheres but vary greatly in assumptions, technique, ingredients, and generality. `PHOENIX` is the only code which is general enough to construct atmospheric models for objects across the entire Hertzsprung-Russel (H-R) diagram in either LTE or non-LTE. The flexibility of `PHOENIX`, therefore, makes it a natural choice for modeling irradiated atmospheres.

`PHOENIX` solves the plane parallel or spherically symmetric RTE with the ALI method on a standard optical depth grid (τ_{std} defined at either 5000Å or 1.2μm) with, typically, 50 layers. The PPRTE is solved along 8 characteristics while the SSRTE is solved along 124 characteristics. Roughly 50,000 frequency points from 10Å to 1000μm are used for a model calculation. When producing a synthetic spectrum for comparison to observations, the resolution is increased to any desired value over the wavelength region of interest.

`PHOENIX` includes 40 of the most important atomic elements from H to La (atomic numbers 1 through 57) as well as their important ions. The atomic data for the energy levels and bound-bound transitions are from Kurucz (1994) and Kurucz & Bell (1995), and the photoionization cross sections are from Mathisen (1984) and Verner & Yakovlev (1995). The molecular opacities include H_2O (Partridge & Schwenke, 1997), TiO (Schwenke, 1998), all diatomics from Kurucz (1993), and all lines from the HITRAN and GEISA databases (Rothman et al., 1992; Husson et al., 1992). Collision induced absorption (CIA) opacities are also included for H_2, N_2, Ar, CH_4, and CO_2 according to (Gruszka & Borysow, 1997, and references therein). At very low effective temperatures ($T_{\mathrm{eff}} < 2500$K, Allard et al., 2001), dust grains are included assuming an interstellar size distribution with diameters ranging from 0.00625 to 0.24μm. The number densities for each grain species are calculated using the method of Grossman (1972) and the Gibbs free energies of formation from the

JANAF database (Chase et al., 1985). The total number of atomic and molecular lines currently available in `PHOENIX` (version 11) is ~ 700 million.

All lines in LTE are treated with a direct opacity sampling (dOS) method. `PHOENIX` does *not* use pre-computed opacity sampling tables, but instead dynamically selects the relevant LTE background lines from master linelists at the beginning of each iteration at several depth points. The total contribution of every selected line within a search window is used to compute the total line opacity at *arbitrary* wavelength points. This method allows detailed and depth dependent line profiles to be used during each iteration. Lines are selected from the master linelist if they are stronger than a threshold $\Gamma \equiv \chi_l/\kappa_c$, which is typically set to 10^{-4}. χ_l is the extinction coefficient at the line center, and κ_c is the total continuous absorption coefficient, both calculated at three representative standard optical depths ($\tau_{\rm std} = 10^{-4}, 10^{-2}, 10$). The profiles of these lines are assumed to be depth-dependent Voigt or Doppler profiles (for very weak lines). Test calculations have shown that the details of the line profiles and the threshold Γ do not significantly affect either the model structure or the synthetic spectra for sufficiently small values of Γ (Schweitzer, 1995; Schweitzer et al., 1996).

2.3 Modifications Needed for Irradiation

The focus of this work is on the structure of irradiated atmospheres and their spectral energy distributions. The problem of producing synthetic binary light curves will not be discussed here and, therefore, some sacrifices in the treatment of the geometry in favor of more detail in the construction of the model atmospheres will be made. Also, since the irradiation effect is important in a wide variety of binary systems, the irradiated object will simply be referred to as the *secondary* and the source of

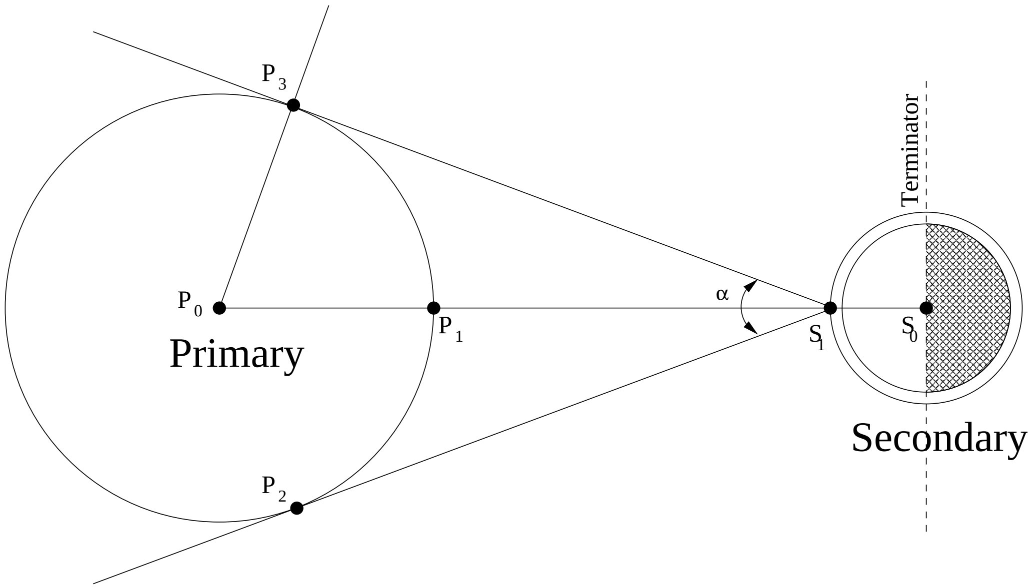

Figure 2.2: Illustration of a secondary irradiated by a primary at the substellar point (S_1). The shaded and unshaded regions on the secondary indicate the night and day sides respectively. See text for more details. This figure is not to scale.

the irradiation as the *primary*. In the following sections, the modifications made to `PHOENIX` in order to model the irradiation effect will be described.

2.3.1 Boundary Conditions

The solution of the RTE is a two-point boundary value problem in the spatial coordinate. For most stellar and substellar atmosphere calculations it is assumed that, at large optical depth, the diffusion approximation holds and defines the lower boundary condition. Also, it is usually sufficient to assume that the object is alone in the universe, and so $I_\nu(\tau = 0, \mu) = 0$ for $\mu < 0$ (i.e. all incoming intensities at the surface are zero).

For a close binary, the traditional *isolated* upper boundary condition is no longer valid and must be replaced by a boundary condition that accounts for the incoming radiation originating from the nearby companion. Thus, for irradiated atmospheres, the upper boundary condition (at $\tau = 0$) becomes,

$$\int_{0}^{2\pi} d\phi \int_{-1}^{0} I_\nu(\phi, \mu)\mu d\mu = F_\nu^{\rm inc}(\tau = 0), \tag{2.4}$$

where $F_\nu^{\rm inc}$ is the monochromatic flux from the primary incident upon the secondary surface. In the case of plane-parallel, extrinsic radiation incident at angles $\mu_{\rm inc}$ and $\phi_{\rm inc}$, $I_\nu(\phi, \mu) = I_\nu^{\rm inc}\delta(\phi - \phi_{\rm inc})\delta(\mu - \mu_{\rm inc})$. From equation 2.4, $I_\nu^{\rm inc} = F_\nu^{\rm inc}$. If the incoming radiation is assumed to be isotropic, then $I_\nu^{\rm inc}(\phi, \mu) = I_\nu^{\rm inc} = \frac{1}{\pi}F_\nu^{\rm inc}$.

Most stellar and substellar objects are well approximated by spheres. Therefore, the radiation from the primary may be treated as if it originated from a point source located at the center of the primary (Wilson, 1990). Figure 2.2 illustrates the irradiation of the point on the secondary closest to the primary, S_1 (the substellar point). The flux (ergs sec^{-1} cm^{-2} Hz^{-1}) received by the secondary at S_1 is $\mathrm{F}^{\rm inc} = (\frac{R_\star}{d})^2 F_\star$, where $R_\star$ is the radius of the primary, $F_\star$ is the flux from the primary surface, and d is the distance from the primary center (P_0) to S_1. Even though the total incident flux may be approximated as if it originated from a point source, the incident angle for the incident intensities will vary over a range equal to the angular size (α) of the primary measured at S_1 (see figure 2.2). For example, intensities originating from near the primary limb (P_3 or P_2) will have incident angles at S_1 equal to $\alpha/2$ and, due to the well known limb darkening effect, these intensities will differ from those originating from P_1. For the systems considered in this work, $\alpha < 10^\circ$ and so this effect will be small. Also, since it is generally not possible to resolve individual surface elements of the secondary (except for objects in our own solar system), we observe the flux averaged over the entire visible hemisphere. Therefore, effects due to angular extension of the primary will not be observable and are ignored here.

Figure 2.3 illustrates the situation for a latitude θ, at point S_2, located somewhere between the substellar point and the terminator (the plane separating the *day* and

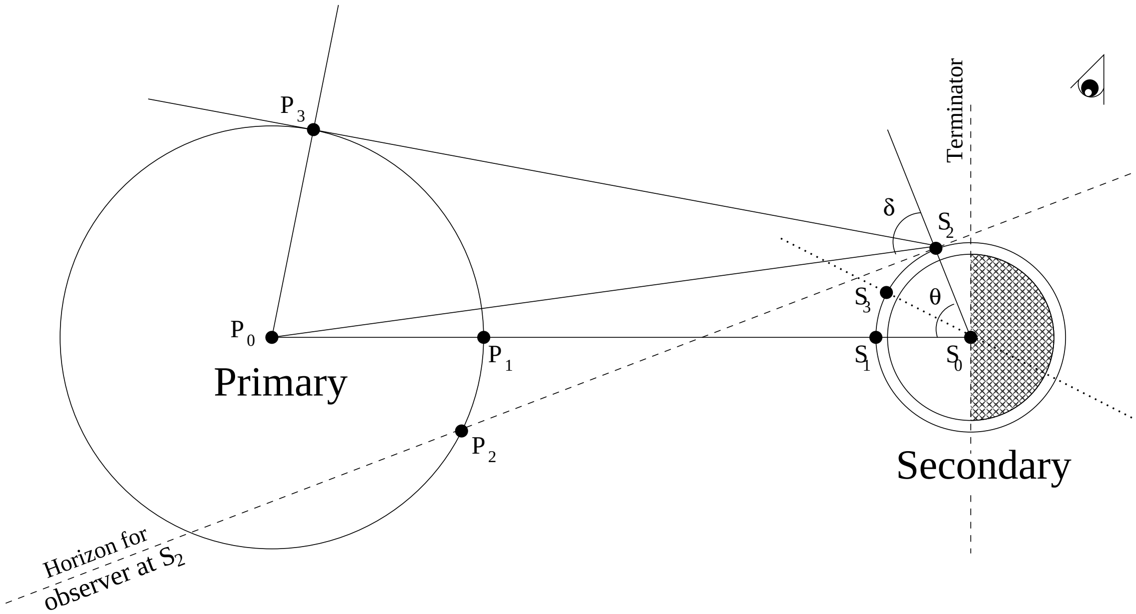

Figure 2.3: Similar to figure 2.2, but illustrating the irradiation of a point (S_2) on the secondary close to the terminator (vertical dashed line). The dotted line intersecting the Secondary is the dividing line for the hemisphere visible to an observer shown, schematically, in the upper right hand corner. See text for more details. This figure is not to scale.

night sides of the secondary). Only radiation incident at an angle δ, measured from the surface normal at S_2, is intercepted by the secondary. If we assume $\theta \approx \delta$, then the distance between P_0 and S_2 is given by, $d^2 = R_s^2 + a^2 - R_s a \cos(\theta)$, where R_s is the radius of the secondary and a is the distance between the primary and secondary centers. The flux directed radially towards the center of the secondary is simply,

$$\mathrm{F}^{\mathrm{inc}} = \left(\frac{R_\star}{d}\right)^2 F_\star \mu. \tag{2.5}$$

Note that, at high latitudes (θ near 90°), a small portion of the primary will be below the horizon of an observer at S_2. In most cases, this penumbra effect is small and will not be considered in the models presented below.

In some situations, energy may be efficiently redistributed across the surface of the secondary (e.g., by winds inside the atmosphere and convection). In this case, a single model that reproduces the “average” structure of the atmosphere can be used to approximate the entire surface, or portions of the surface. From equation 2.5, the total energy received by the secondary (per second) is simply, $(\pi \mathrm{R}_s^2)\mathrm{F}^{\mathrm{inc}}(\mu = 1)$. If this energy is uniformly redistributed over the day hemisphere, then the secondary effectively receives, on average, $\mathrm{F}^{\mathrm{inc}}_{\mathrm{avg}} = \frac{1}{2}\mathrm{F}^{\mathrm{inc}}(\mu = 1)$. Similarly, if the energy is redistributed over the entire sphere, then $\mathrm{F}^{\mathrm{inc}}_{\mathrm{avg}} = \frac{1}{4}\mathrm{F}^{\mathrm{inc}}(\mu = 1)$. Defining a redistribution factor Q, which has a value between 1 and $\frac{1}{4}$, allows the average incident flux to be written generally as,

$$\mathrm{F}^{\mathrm{inc}}_{\mathrm{avg}} = Q\left(\frac{R_\star}{d}\right)^2 F_\star. \tag{2.6}$$

Note that $Q = 1$ implies no redistribution and $\mathrm{F}^{\mathrm{inc}}_{\mathrm{avg}} = \mathrm{F}^{\mathrm{inc}}(\mu = 1)$.

2.3.2 Temperature Corrections

Given the iterative nature of the model atmosphere problem, it is necessary to apply a correction to the source function at the end of each iteration so that the radiative equilibrium constraint is satisfied. One powerful and simple technique for determining the correction is the Unsöld-Lucy (U-L) procedure. The following derivation closely follows that of Lucy (1964) which was intended for plane parallel LTE atmospheres with the traditional "isolated" upper boundary condition.

The derivation begins with the time independent spherically symmetric transfer equation,

$$\mu\frac{\partial}{\partial r}I_\nu + \frac{1-\mu^2}{r}\frac{\partial}{\partial \mu}I_\nu = (\kappa_\nu + \sigma_\nu)\rho(S_\nu - I_\nu), \tag{2.7}$$

where κ_ν and σ_ν are the absorption and scattering coefficients, repsectively. The remaining quantaties are defined above in section 2.1.1.

The moments of the transfer equation are obtained by applying the operators $\frac{1}{2}\int\limits_{-1}^{1} d\mu$ and $\frac{1}{2}\int\limits_{-1}^{1} \mu d\mu$ to equation 2.7. These moments are:

$$-(\kappa_\nu + \sigma_\nu)\rho H_\nu = \frac{\partial}{\partial r}(K_\nu) + \frac{(3K_\nu - J_\nu)}{r} \quad \text{and} \tag{2.8}$$

$$\frac{\partial}{\partial r}(r^2 H_\nu) = -(\kappa_\nu + \sigma_\nu)\rho r^2 (J_\nu - S_\nu), \tag{2.9}$$

where H_ν is the Eddington flux ($H_\nu = \frac{1}{2}\int\limits_{-1}^{1} I_\nu \mu d\mu$) and K_ν is the second moment of the radiation field ($K_\nu = \frac{1}{2}\int\limits_{-1}^{1} I_\nu \mu^2 d\mu$).

Integrating over frequency and inserting the mean opacities,

$\kappa_P = \frac{1}{B}\int\limits_0^\infty \kappa_\nu B_\nu d\nu$ – Planck mean

$\kappa_J = \frac{1}{J}\int\limits_0^\infty \kappa_\nu J_\nu d\nu$ – absorption mean

$\kappa_H = \frac{1}{H}\int\limits_0^\infty (\kappa_\nu + \sigma_\nu) H_\nu d\nu$ – flux mean

equations 2.8 and 2.9 become [1]

$$\begin{aligned} -\rho\kappa_H H &= \frac{\partial}{\partial r}(K) + \frac{(3K - J)}{r} \quad \text{and} \\ \frac{\partial}{\partial r}(r^2 H) &= -\rho\kappa_P r^2 (\frac{\kappa_J}{\kappa_P} J - B). \end{aligned} \tag{2.10}$$

Note that the approximate expression for the source function, $S_\nu = (\kappa_\nu B_\nu + \sigma_\nu J_\nu)/(\kappa_\nu + \sigma_\nu)$, has been assumed.

The first equation in 2.10 may be transformed into a first order linear equation by introducing the variable Eddington factor, $f = \frac{K}{J}$. The equations in 2.10 are straight forward to solve by introducing an integrating factor, q. Expressed in the following way,

$$\ln(r^2 q) = \int\limits_{r_c}^{r} \frac{(3f - 1)}{r' f} dr' + \ln({r_c}^2), \tag{2.11}$$

q is often called the *sphericality* function which was first introduced by Auer (1971). After applying the integration factor, the equations in 2.10 become

[1] Note that the subscript ν has been dropped to indicate wavelength integrated quantities.

$$\frac{\partial}{\partial \tau}(qf\mathcal{J}) = q\frac{\kappa_H}{\kappa_P}\mathcal{H} \quad \text{and}$$
$$\frac{\partial}{\partial \tau}(\mathcal{H}) = (\frac{\kappa_J}{\kappa_P}\mathcal{J} - \mathcal{B}), \tag{2.12}$$

where $\mathcal{J}= r^2 J$, $\mathcal{H}= r^2 H$, $\mathcal{B}= r^2 B$, and $\partial\tau = -\rho\kappa_P \partial r$. The moment equations have now been reduced to functions of only one independent variable, the Planck mean optical depth τ.

Let $\Delta\mathcal{B}(\tau)$ be the correction to the source function such that, upon the next iteration, the correct target flux, H_{target}, is obtained at each layer. The moment equations then become

$$\frac{\partial}{\partial \tau}(q'f'\mathcal{J}') = q'\frac{\kappa'_H}{\kappa'_P}\mathcal{H}_{\text{target}} \quad \text{and}$$
$$\frac{\partial}{\partial \tau}(\mathcal{H}_{\text{target}}) = (\frac{\kappa'_J}{\kappa'_P}\mathcal{J}' - \mathcal{B} - \Delta\mathcal{B}), \tag{2.13}$$

where $'$ denotes quantities to be determined at the end of the next iteration.

One of the benefits of introducing the means defined above is that their ratios do not change much from one iteration to the next. Therefore, one may assume that $\frac{\kappa'_H}{\kappa'_P} = \frac{\kappa_H}{\kappa_P}$ and $\frac{\kappa'_J}{\kappa'_P} = \frac{\kappa_J}{\kappa_P}$. Using these approximations and further assuming $f = f'$, we may subtract the equations in 2.13 from those in 2.12 obtaining two equations with just two unknowns:

$$\frac{\partial}{\partial \tau}(qf\Delta\mathcal{J}) = q\frac{\kappa_H}{\kappa_P}\Delta\mathcal{H} \quad \text{and}$$
$$\frac{\partial}{\partial \tau}(\Delta\mathcal{H}) = (\frac{\kappa_J}{\kappa_P}\Delta\mathcal{J} + \Delta\mathcal{B}), \tag{2.14}$$

where $\Delta\mathcal{J} = \mathcal{J} - \mathcal{J}'$ and $\Delta\mathcal{H} = \mathcal{H} - \mathcal{H}_{\text{target}}$. By explicitly assuming $f = f'$, we are also assuming that $f = \frac{\Delta\mathcal{K}}{\Delta\mathcal{J}}$, a fact that will become important later.

Solving the first equation in 2.14 for $\Delta\mathcal{J}$ gives

$$\Delta\mathcal{J}(\tau) = \frac{1}{q(\tau)f(\tau)}\left(q(0)f(0)\Delta\mathcal{J}(0) + \int_0^\tau q(\tau')\frac{\kappa_H(\tau')}{\kappa_P(\tau')}\Delta\mathcal{H}(\tau')d\tau'\right). \tag{2.15}$$

Inserting $\Delta\mathcal{J}$ into the second equation in 2.14 and solving for $\Delta\mathcal{B}$ yields an expression for the correction to the source function;

$$\Delta\mathcal{B}(\tau) = \frac{d\Delta\mathcal{H}}{d\tau} + \tag{2.16}$$

$$\frac{\kappa_J}{\kappa_P}\left(q(0)f(0)\Delta\mathcal{J}(0) + \int_0^\tau q(\tau')\frac{\kappa_H(\tau')}{\kappa_P(\tau')}\Delta\mathcal{H}(\tau')d\tau'\right)\frac{1}{q(\tau)f(\tau)}.$$

Instead of computing the gradient of the flux, it is simpler to use the fact that

$$\frac{d\Delta\mathcal{H}}{d\tau} = \frac{d\mathcal{H}}{d\tau} = \frac{\kappa_J}{\kappa_P}\mathcal{J} - \mathcal{B}. \tag{2.17}$$

Using the second Eddington approximation, $2\mathcal{H}(0) = \mathcal{J}(0)$, and inserting equation 2.17 into equation 2.16, the correction to the source function becomes,

$$\Delta\mathcal{B}(\tau) = \frac{\kappa_J}{\kappa_P}\mathcal{J}(\tau) - \mathcal{B}(\tau) + \tag{2.18}$$

$$\frac{\kappa_J}{\kappa_P}\left(2q(0)f(0)\Delta\mathcal{H}(0) + \int_0^\tau q(\tau')\frac{\kappa_H(\tau')}{\kappa_P(\tau')}\Delta\mathcal{H}(\tau')d\tau'\right)\frac{1}{q(\tau)f(\tau)}.$$

All quantities on the right hand side of equation 2.18 are available upon completion of each iteration and, so, the correction to the source function may be determined. In practice, however, applying a correction to the gas temperature is more convenient than applying a correction to the source function directly. Using the Stefan-Boltzmann law and differentiating $\mathcal{B}$ with respect to T gives the temperature correction at each layer;

$$\Delta T(\tau) = \frac{\Delta\mathcal{B}(\tau)}{4\sigma T(\tau)^3 r^2}. \tag{2.19}$$

The expression, $\frac{\kappa_J}{\kappa_P}\mathcal{J} - \mathcal{B}$, is always small at large optical depth where the gas pressures and densities are high and $S \to B$. Therefore, the first term on the right hand side of 2.18 only generates a correction in the optically thin parts of the atmosphere. The second term is most important in the optically thick regions and also ties the thermal structure to the prescribed target flux.

In the presence of irradiation, the atmosphere's upper boundary is altered to account for the incident flux as described in section 2.3.1. Requiring strict energy conservation implies that all of the energy received by the secondary must be reradiated into space either as a contribution to the thermal flux or as reflected light. As a result, the target flux ($H_{\rm target}$) is now given by:

$$H_{\rm target} = H^{\rm ext}(\tau) + \sigma T_{\rm int}^4 \tag{2.20}$$

where $H_\nu^{\rm ext}(\tau)$ is the extrinsic Eddington flux ($H_\nu^{\rm ext} = \frac{1}{4\pi}F_\nu^{\rm inc}$) that has penetrated down to optical depth τ and $\sigma T_{\rm int}^4$ is the total flux due solely to the secondary's intrinsic energy source.

The U-L temperature correction procedure derived above is formally correct even in the case of strong irradiation (so long as the correct target flux is supplied). However, for the reason described below, the correction scheme can become unstable when $H_{\rm ext}(\tau) \gg \sigma T_{\rm int}^4$. With a few modifications, stability can be achieved.

The first modification concerns the Eddington approximation used to relate ΔJ with ΔK. If the total intensities are separated into intrinsic and extrinsic components then, similarly, the moments of the radiation field may also be separated into intrinsic and extrinsic components; $J = J_{\rm ext} + J_{\rm int}$, $K = K_{\rm ext} + K_{\rm int}$ and $H = H_{\rm ext} + H_{\rm int}$. Since the radiation from the primary is constant, the extrinsic components will also be constant from one iteration to the next apart from changes that will occur in the opacities (due to changes in T). Therefore, ΔJ becomes $\Delta J = J_{\rm int} - J'_{\rm int}$ and likewise for ΔK and ΔH. Thus, in the case of irradiation, equation 2.14 should involve only intrinsic mean intensities ($\mathcal{J}_{\rm int}$). Also, since we used f to relate $\Delta\mathcal{J}$ with $\Delta\mathcal{K}$, f must also involve only intrinsic quantities. Therefore f, in equation 2.18, should be replaced by $f_{\rm int} = (\frac{\Delta J}{\Delta K})_{\rm int}$ and assume that $f_{\rm int} = f'_{\rm int}$.

The second modification is slightly more subtle and involves κ_H (defined above). The second correction term in equation 2.18 applies a "*torque*" on the temperature structure in a direction governed solely by the sign of ΔH; if $\Delta H(\tau) = H(\tau) - H_{\rm target}(\tau) < 0$, then the temperature is too cool and must be increased. This is true because all other quantities besides ΔH in the second term are normally positive. In the irradiated case, this is not always true, especially for κ_H.

In the presence of large extrinsic flux, the total flux ($H_{\rm total} = H_{\rm int} + H_{\rm ext}$) may be negative since $|H_{\rm ext}| \gg H_{\rm int}$ and $H_{\rm ext} < 0$, which will lead to $\Delta H < 0$. In the case of cool secondaries, both the intrinsic flux and the opacities peak in the IR while the extrinsic flux peaks in the optical or ultra-violet. It is, therefore, possible that the total flux may be negative while $\int\limits_0^\infty (\kappa_\nu + \sigma_\nu) H_\nu d\nu$ is positive. A situation where $H < 0$, $\Delta H < 0$ and $\kappa_H < 0$ is illustrated in figure 2.4. If this occurs, the second term on the right hand side of equation 2.18 will lead to corrections in the wrong direction causing instabilities.

The solution to this problem is straight forward if the following changes are considered. As was done for ΔJ and ΔK, $\kappa_H H$ may be separated into intrinsic and extrinsic components:

$$\kappa_H H = \kappa_H^{\rm int} H_{\rm int} + \kappa_H^{\rm ext} H_{\rm ext} \tag{2.21}$$

where

$$\kappa_H^{\rm int} = \frac{1}{H_{\rm int}} \int\limits_0^\infty (\kappa_\nu + \sigma_\nu) H_\nu^{\rm int} d\nu \tag{2.22}$$

$$\kappa_H^{\rm ext} = \frac{1}{H_{\rm ext}} \int\limits_0^\infty (\kappa_\nu + \sigma_\nu) H_\nu^{\rm ext} d\nu. \tag{2.23}$$

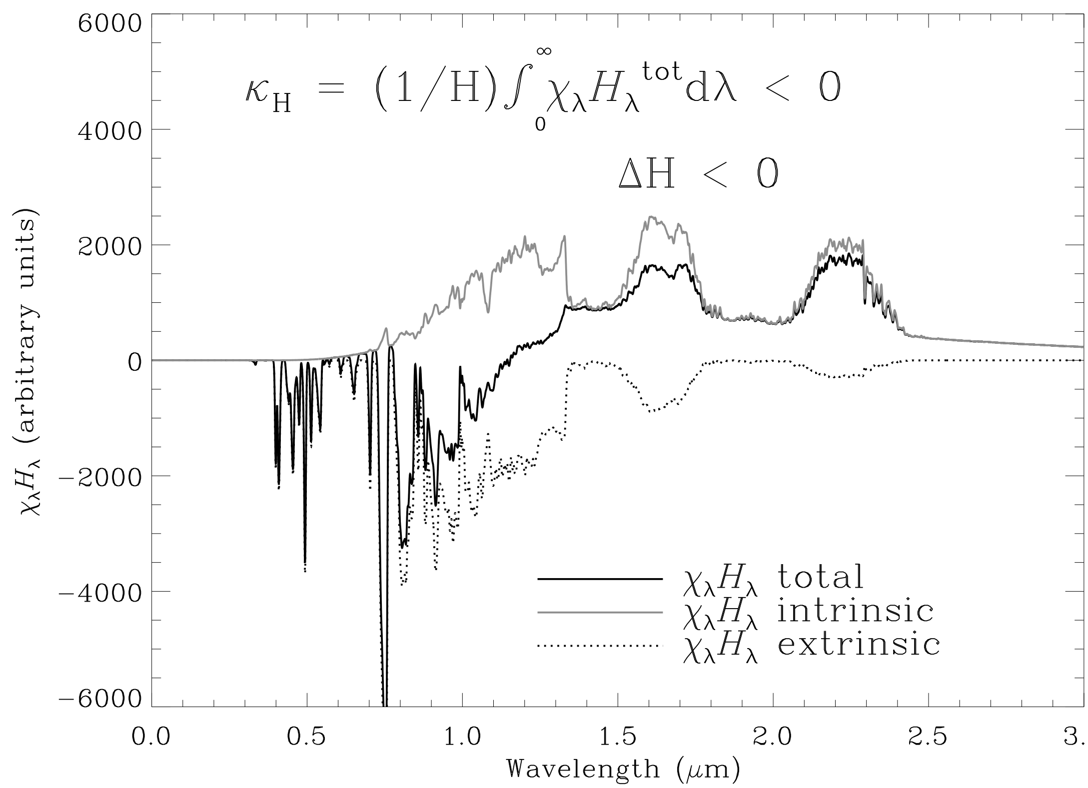

Figure 2.4: A comparison between the total, extrinsic and intrinsic flux-weighted opacities measured at $\tau_{\rm std} = 1.0$. The figure is for illustrative purposes only, and does not necessarily represent the conditions in a real atmosphere. In this situation, $H < 0$, $\Delta H < 0$ and $\kappa_H < 0$. When this occurs, a temperature correction will be generated in the wrong direction.

It is also plausible to assume that $(\kappa_H^{\rm ext} H_{\rm ext}) \approx (\kappa_H^{\rm ext} H_{\rm ext})'$, in which case, the integrand in equation 2.18 becomes,

$$\int_0^\tau q(\tau') \frac{\kappa_H^{\rm int}(\tau')}{\kappa_P(\tau')} \Delta H(\tau') d\tau', \tag{2.24}$$

where $\Delta H = H_{\rm int} - H_{\rm target}$. $\kappa_H^{\rm int}$ will always be positive (since always $H_{\rm int} > 0$), and the correction should be generated in the proper direction. Note that κ_J in the second equation of 2.14 could be reduced in a similar manner to $\kappa_J{}^{\rm int}$, however testing has shown that this usually does not lead to any major improvements.

On a practical note, when solving the radiative transfer equation, the entire radiation field is considered (intrinsic and extrinsic) and the total intensities are normally solved for. In order to implement the modifications introduced above, the radiative transfer equation must be solved *twice* per global iteration; once without the extrinsic radiation field and a second time with the extrinsic radiation. The difference between the monochromatic intensities with and without the extrinsic radiation gives the intrinsic intensities. Once the separate intensities are known, the separate moments of the radiation field may be calculated and the temperature corrections determined.

For $\tau < 1$, the second correction term in 2.18 becomes more important with increasing external radiation and the modifications are crucial for the U-L procedure to work. For large external flux and an initial guess that is far from the correct structure (but reasonably close by most standards), the unmodified U-L scheme will produce large oscillating temperature corrections and usually will not converge while the modified scheme converges nicely (i.e. energy is conserved to the prescribed accuracy) . Even when the correct solution is used as the initial guess, the unmodified scheme moves away from the correct solution and stabilizes on a different structure which doesn't satisfy radiative equilibrium.

2.4 An Example: Jupiter

The Galileo spacecraft was launched in 1989 and arrived at Jupiter in December, 1995. Galileo's primary objectives were to investigate the chemical composition and structure of Jupiter's atmosphere, study the dynamics of the magnetosphere, and to study the Jovian satellites. The Galileo probe, which was launched into Jupiter's atmosphere by the orbiting spacecraft, contained numerous tools for measuring the properties of the atmosphere. The atmospheric structure instrument (ASI) was designed to measure the temperature, pressure, and density during the probes descent. The net flux radiometer (NFR) measured the long range cloud properties while a nephelometer (NEP) measured the cloud properties in the direct vicinity of the probe. These instruments (and others) provided the first in-situ observations of a non-terrestrial planetary atmosphere. Previous earth-bound and spacecraft IR measurements were only capable of inferring the structure of the upper atmosphere (0.1 mbar to 1 bar) and no measurements were possible down in the lower atmosphere ($P_{gas} > 1$ bar) below the cloud decks.

2.4.1 Comparison To The Galileo Data

Despite the fact that Jupiter is 5.2 times farther from the Sun than the Earth is, irradiation plays an important role in determining the conditions in the upper Jovian atmosphere. A stratosphere, dominated by solar radiation which is mostly absorbed by methane, exists above $P_{gas} = 10$ mbars. A temperature minimum occurs at roughly 100 mbars followed by a temperature rise down into the deeper atmospheric layers which are dominated by convection.

Using the `PHOENIX` atmosphere code, along with the modifications described above, a model of Jupiter's atmosphere was calculated assuming a solar metal abundance, $T_{eff} = 128$K, mass equal to $1M_J = 2 \times 10^{30}$ g, radius equal to $1R_J = 7 \times 10^9$ cm, and including solar incident radiation at the correct Jupiter-Sun separation (5.2 AUs $= 7.5 \times 10^{13}$ cm). A comparison between the model structure and the temperature-pressure data provided by ASI is shown in figure 2.5 along with a similar non-irradiated model (i.e. same physical parameters less the irradiation).

The most striking feature of the ASI data is the large temperature rise in the thermosphere ($P_{gas} < 10^{-6}$ bars). This feature has yet to be explained by any atmospheric model. Gravity waves (Hickey et al., 2000) and acoustic waves

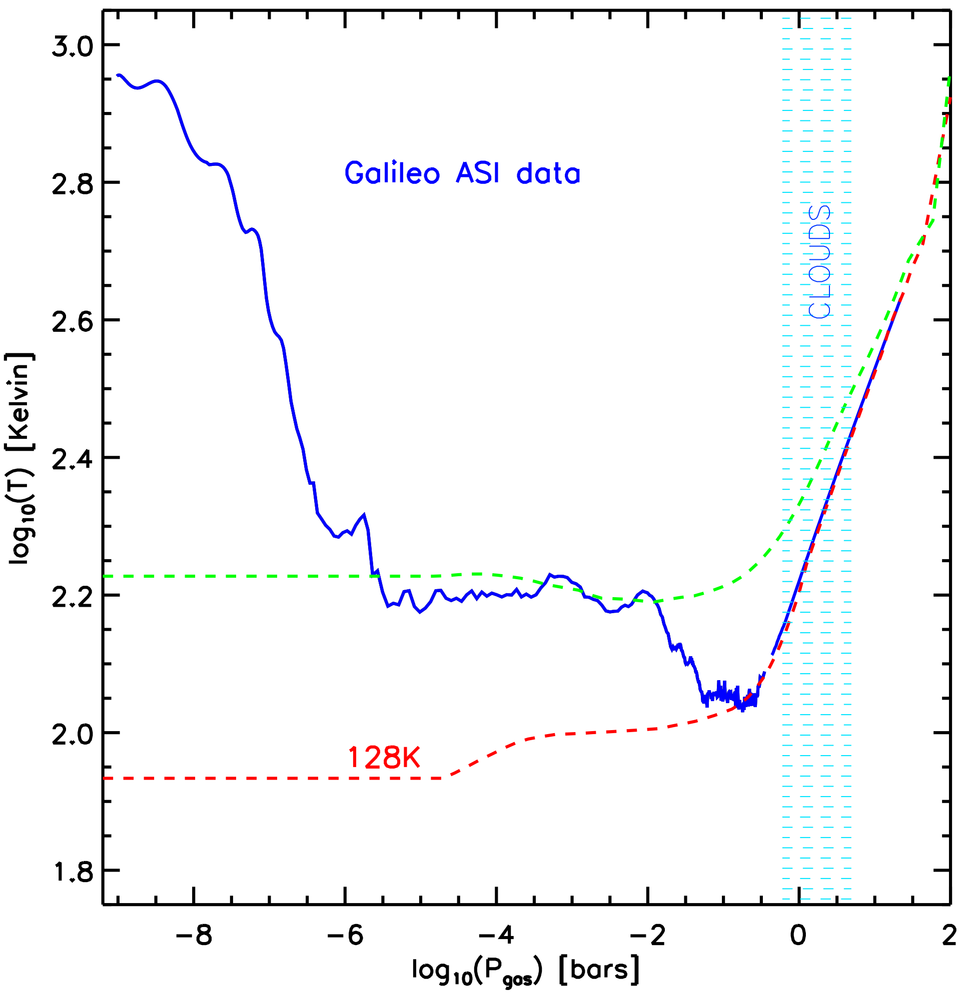

Figure 2.5: A comparison between the Galileo ASI probe data (solid line), a non-irradiated model atmosphere (lower dashed line), and an irradiated model atmosphere (top dashed line). The vertical shaded area indicates the location of cloud structures detected by the probe. See text for details of the model calculation.

(Schubert et al., 2001) are being explored as possible heating mechanisms. The irradiated model reproduces the general behavior of the ASI data below the thermosphere and predicts the correct isothermal region. However, the irradiated model is hotter for much of the atmosphere with $P_{gas} > 10^{-2}$ bars, and the temperature minimum is much lower in the ASI data than in the irradiated model. A non-irradiated model, with the same physical parameters reproduces the temperature structure of the lower atmosphere almost perfectly (see lower dashed line, fig. 2.5). The discrepancy is likely due to clouds that are not included in either the irradiated or non-irradiated model.

The probe entered the atmosphere at a rather atypical region (known as a 5μm hot spot) that contained relatively little particulate matter and few cloud structures. The NEP and NFR, which tested for the presence of clouds, only measured the region below $P_{gas} = 0.46$ bars. The NEP detected slight cloud features near 1.34 bars (Ragent et al., 1998). The NFR, however, detected a cloud deck at 0.6 bars, where many models have predicted an NH_3 cloud (Stromovsky et al., 1998). The cloud region detected by the probe is shown in figure 2.5. The differences between the two models and the ASI data shows the importance of irradiation and clouds. The limiting effect of dust in irradiated EGP atmospheres will be investigated in chapter 3.

Despite the differences between the irradiated model and the ASI data, the results show that `PHOENIX` is capable of modeling planetary atmospheres. Note that clouds will be irrelevant for the pre-CVs studied in chapter 5.

Chapter 3

Irradiated Planets[1]

3.1 Introduction

Many indirect detections of substellar objects in close orbit around stars of spectral type later than F have been made since 1996. However, currently there are few observations that can be useful for constraining the large parameter space (e.g., chemical composition, albedo, age, and inclination) for any of these so called extra-solar giant planets (EGPs). The transits observed for HD209458b by Henry et al. (2000) and Charbonneau et al. (2000) have helped constrain the gross physical parameters of HD209458b (radius, mass, mean density, etc.) but not any of the atmospheric properties. There is great hope that the handful of ambitious space and ground based projects planned for the next decade will be capable of making direct photometric observations of EGPs and possibly measurements of EGP spectral features. Until then, we must rely on atmospheric modeling to provide insight into the basic properties of these objects to guide the observers while we wait patiently for their observations.

An early work by Saumon et al. (1996) investigated the properties of EGPs for various masses and ages near primaries of different spectral type but approximated the reflected and thermal flux as gray bodies. More recently there have been several radiative equilibrium models produced for the purpose of predicting certain observables for 51 Pegasi b (Seager & Sasselov, 1998) and τ Boo (Goukenleuque et al.,

[1] Barman, T. S., Hauschildt, P. H., and Allard, F. 2001, *The Astrophysical Journal*, 556, 885. Reprinted here with the permission of publisher.

2000). Also, a broad range (100 – 1700K) of EGP models were studied and loosely classified by Sudarsky et al. (2000) using ad hoc temperature – pressure profiles. In this paper, we present equilibrium models for several scenarios well within the known parameter space for EGPs. We have investigated the variations of the thermal structures and emergent flux as functions of both the spectral type of the primary and the orbital separation. We also address the importance of spherical versus plane parallel radiative transfer. Our emphasis in this paper is not on any one particular EGP, but instead on the basic understanding of these objects and the effects of their close proximity to a stellar companion.

3.2 Model Construction

We have used our multi-purpose atmosphere code `PHOENIX` (version 10.9) to generate the models discussed below. Most details of the radiative transfer method may be found in Hauschildt & Baron (1999), but, for clarity, we repeat some of the basic features and discuss a few changes needed for irradiated models. `PHOENIX` solves either the full spherically symmetric or plane parallel radiative transfer equation (PPRTE) using an operator splitting (OS) technique. For the majority of the calculations presented here, we have chosen plane parallel geometry and assumed hydrostatic equilibrium. However, we will discuss the importance of spherical geometry in section 3.4.4. All models are subject to an energy conservation constraint such that the total Flux (convective and radiative) is constant at each layer. Each model atmosphere spans a range of optical depth ($\tau_{\rm std}$ defined at 1.2μm) from 0 at the top of the atmosphere down to 100 at the deepest layer. Convection is treated according to the Mixing Length Theory from the onset of the Schwarzschild criterion with mixing length parameter, $\alpha = 1$.

The usual boundary conditions for an isolated star are that the inward directed flux at the surface should be zero ($\mathrm{I}_\nu^\downarrow(\tau_{\mathrm{std}} = 0, \mu) = 0$, where $-1 \leq \mu = \cos(\theta) \leq 0$) and that the diffusion approximation holds at the bottom of the atmosphere. For a close binary, the situation is clearly different. At the surface of the secondary, the boundary condition on $\mathrm{I}_\nu^\downarrow$ is determined by the incident flux ($\mathrm{F}_\nu^{\mathrm{inc}}$) given by:

$$2\pi \int_{-1}^{0} \mathrm{I}_\nu^\downarrow(\mu)\mu d\mu = \mathrm{F}_\nu^{\mathrm{inc}}(\tau_{\mathrm{std}} = 0) \tag{3.1}$$

where

$$\mathrm{F}_\nu^{\mathrm{inc}}(\tau_{\mathrm{std}} = 0) = \left(\frac{R^\star}{a}\right)^2 \mathrm{F}_\nu^\star \tag{3.2}$$

In the equations above, $\mathrm{I}_\nu^\downarrow(\mu)$ refers to the inward directed intensities along direction μ, $R^\star$ is the radius of the primary, a is the surface to surface primary-secondary separation, and $\mathrm{F}_\nu^\star$ is the monochromatic flux from the primary. For $\mathrm{F}_\nu^\star$, we use a synthetic spectrum taken from a previous `PHOENIX` calculation (Hauschildt et al., 1999; Allard et al., 2000). For the models presented below, we have made the simplifying assumption that the impinging radiation field is isotropic, meaning that $\mathrm{I}_\nu^\downarrow(\mu)$ at the surface is the same for all μ (i.e., $\mathrm{I}_\nu^\downarrow(\mu) = \mathrm{I}_\nu^\downarrow$). We have also assumed that the flux is *not* globally redistributed over the planet's surface. A more detailed discussion of these last two issues may be found in section 3.4.4.

As was done in the work on irradiated M Dwarfs by Brett & Smith (1993), all of the incident radiation from the primary is re-radiated outward by the secondary in the form of reflected flux ($\mathrm{F}^{\mathrm{ref}}$) and as a contribution to the thermal flux ($\mathrm{F}^{\mathrm{therm}}$). This constraint is required by energy conservation and implies that the integrated flux at the surface is equal to $\sigma \mathrm{T}_{\mathrm{int}}^4 + \mathrm{F}^{\mathrm{inc}}$. Throughout this paper, $\mathrm{T}_{\mathrm{int}}$ refers to the effective temperature of the planet in the *absence* of irradiation and $4\pi {\mathrm{R_p}}^2 \sigma \mathrm{T}_{\mathrm{int}}^4$ equals the planet's intrinsic luminosity where $\mathrm{R_p}$ is the planet's radius. The intrinsic luminosity is an age dependent quantity which represents the energy released by the planet as it cools and contracts. T_{int} also relates irradiated planets to isolated planets in which case T_{int} is identical to the more commonly used T_{eff}.

The "effective temperature" (T_{eff}), which is customarily defined as the temperature a black body would have to have in order to radiate the total flux, has important physical and observational significance for isolated stellar and substellar objects. However, for irradiated planets (and stars) T_{eff} loses some of its connection to the fundamental properties of the planet because it is difficult to separate, by observation, those photons which are thermally radiated by the planet from those which originated from the primary and are merely reflected by the planet. We shall only use T_{eff}, with its customary definition, to describe non-irradiated objects. When describing irradiated objects, we will define another quantity which describes the equilibrium temperature of the planet's day side;

$$\sigma \mathrm{T}_{\mathrm{eq}}^4 = \sigma \mathrm{T}_{\mathrm{int}}^4 + (1 - A_B)\mathrm{F}^{\mathrm{inc}}, \tag{3.3}$$

where A_B is the Bond albedo. Since the reflected flux is not directly related to the equilibrium thermal structure of the atmosphere, it has been omitted from equation 3.3 and, therefore, distinguishes T_{eq} from T_{eff}. It is also important to realize that T_{eq}, as defined above, represents the equilibrium state at a given age and allows for the possibility that the intrinsic luminosity has not reached zero. T_{int} will only be important for young (or more massive) planets when the primary is a solar type star. However, for planets orbiting M dwarfs, T_{int} can be a significant contribution to T_{eq}. While T_{eq}, which likely varies across the planet's day side, tells us little about the interior or the non-irradiated face of the planet it does provide a useful measure of the effects on the thermal structure of the planet's day side. It is also important to realize that T_{int} is not necessarily the equilibrium temperature of the planet's night side since energy may be carried over from the day side.

To produce an irradiated atmospheric model, we chose the structure of a converged non-irradiated model taken from Allard et al. (2001) as the initial structure of an irradiated atmosphere located $\sim$ 5AU from the primary. At this distance, the impinging radiation produces only small changes in the structure of the upper layers and convergence is achieved after only a few iterations. This new model is then used as the initial structure for an irradiated atmosphere located at $\sim$ 2.5AU from the primary. This process of moving the planet closer to the primary is repeated until the desired orbital separation is reached. Each intermediate calculation is iterated until the changes to the temperature structure are less than 1 K at every depth point and energy conservation is satisfied to within a few percent. Models obtained in this way will have structures, at the deepest layers, similar to the initial non-irradiated model chosen from Allard et al. (2001), and thus depend on $\log(g)$, and the assumed value of $T_{\rm int}$.

The opacity setups used for the EGPs are identical to the "AMES-Cond" and "AMES-Dusty" models of Allard et al. (2001) which refer to two limiting cases. AMES-Cond refers to the situation when dust forms in the atmosphere at locations determined by the chemical equilibrium equations, but has been entirely removed from the atmosphere by efficient gravitational settling. Dust formation, therefore, acts only to remove refractory elements and reduce the number of certain molecules but does *not* contribute to the overall opacity. The opposite case, AMES-Dusty, ignores settling altogether. Dust forms based on the same criteria as in the AMES-Cond models yet remains present to contribute to the opacity. The Cond model may be thought of as "clear skies", and the Dusty model as "cloudy skies".

The opacities include H_2O and TiO lines by Partridge & Schwenke (1997), CH_4 lines from the HITRAN and GEISA databases (Rothman et al., 1992; Husson et al., 1992), and H_2, N_2, Ar, CH_4, and CO_2 collision induced absorption (CIA) opacities according to (Borysow et al., 1997a,b; Borysow & Frommhold, 1986a, 1987a, 1986b; Borysow & Tang, 1993; Samuelson et al., 1997; Borysow & Frommhold, 1986c, 1987b; Gruszka & Borysow, 1997, and references therein). To include dust grains, we have assumed an interstellar size distribution with diameters ranging from 0.00625 to 0.24μm and the chemical equilibrium equations incorporate over 1000 liquids and crystals. We follow the prescriptions of Grossman (1972) and use Gibbs free energies of formation from the JANAF database (Chase et al., 1985) to compute the number densities for each grain species. The condensation equilibrium is directly incorporated into the chemical equilibrium equations to account, self-consistently, for the depletion of refractory elements as a function of gas temperature and pressure. With this approach, any changes to the structure brought on by irradiation will be automatically accounted for in the chemical equilibrium equations.

3.3 Results

We have divided our study into two separate cases: one for which the primary star is a dM5 ($T_{\mathrm{eff}} = 3000$K, see Leggett et al. (2000); Allard et al. (2000)) and another where the primary is a G2 solar type star ($T_{\mathrm{eff}} = 5600$K, see Hauschildt et al. (1999)). For the former case, one finds few observed objects in the literature (e.g. Gl876B). However, surveys for additional objects have begun (Delfosse et al., 1999) . In the last decade, most of the observations have been spent searching for objects that fall into the second group, and, to date, there are roughly 50 planets known to be in orbit around solar type stars. For both of these cases, we consider different effective temperatures and several orbital separations. Below, we present the structures and spectra for each case and discuss the effects caused by the impinging radiation.

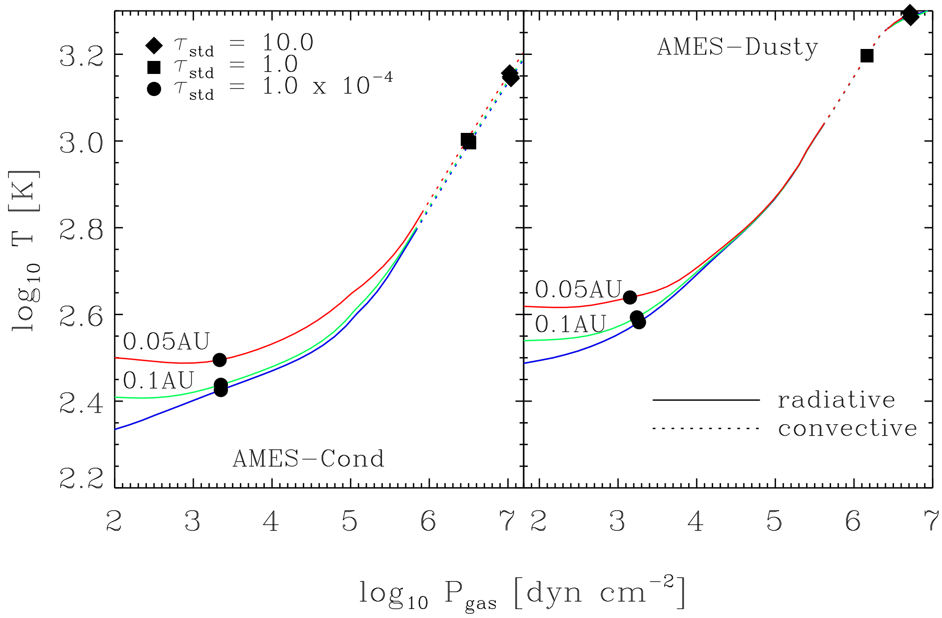

Figure 3.1: Temperature structures for the non-irradiated and irradiated planet (T_{int} = 500K, $\log(g)$ = 3.5) when located 0.1 and 0.05AU from a dM5 (T_{eff} = 3000K). AMES-Cond is shown on the left and AMES-Dusty on the right. The lowest curve in each panel is the non-irradiated structure. The filled symbols refer to different optical depths (τ) at $\lambda = 1.2\mu$m.

3.3.1 EGPs Around M Dwarfs

Gl876B was the first planetary companion found orbiting an M dwarf. This was an important discovery given that M dwarfs constitute nearly 70% of all stars in the galaxy (Henry, 1998). Gl876B is also one of the nearest EGPs (only 5 pc away) making it a promising candidate for direct imaging by future adaptive optics and interferometry missions (Marcy et al., 1998). Our first group of irradiated models is intended to represent objects, like Gl876B, which have cool stellar primaries. We begin with a planet having T_{int} = 500K, R_p = $1R_{jup}$ and $\log(g)$ = 3.5 located very close to a dM5. Both planet and primary have solar compositions.

In Figure 3.1, we show the temperature structure of the non-irradiated planet compared to irradiated thermal structures at 0.1 and 0.05AU for both the AMES-

Cond and AMES-Dusty cases. The outermost regions are significantly altered by the radiation from the dM5 resulting in a generally flatter temperature profile. Without dust opacity (the AMES-Cond model), the impinging radiation is capable of heating the lower layers of the planet thereby reducing the temperature gradient. Above the photosphere ($\tau_{\rm std} < 10^{-4}$), the largest temperature increase occurs and a very slight temperature inversion forms at 0.05AU. Dust opacity generally produces a hotter atmosphere at all depths with a smoother spectral energy distribution. For more details on the effects of dust in non-irradiated atmospheres, see Allard et al. (2001). It is important to stress that the solution of the chemical equilibrium equations is based on the final temperature structure and thus incorporates the irradiation effects.

In the AMES-Dusty models, Fe, Mg_2SiO_4, $MgSiO_3$ and $CaMgSi_2O_6$ and $MgAl_2O_4$ are the dominant dust species which form a cloudy region extending from roughly $\tau_{\rm std} = 1.0$ to the top of the atmosphere. Below this region ($\tau_{\rm std} > 1.0$) is a complicated mixture of various other condensates. In Figure 3.2, the concentrations of the dominant dust species are shown for the irradiated and non-irradiated planets. There is little change in the abundance of the condensates brought on by the impinging radiation from the dM5.

The spectra for the irradiated and non-irradiated planets are shown in Figure 3.3. The isolated AMES-Dusty planet produces a very smooth spectrum in the optical as is expected for an atmosphere dominated by grain opacity. In the IR, several distinct molecular bands are present: CH_4 at 1.6μm, 2.1 – 2.5μm, and 3.0 – 4.0μm, and H_2O between 2.5 and 3.0μm. The reflective properties of the dust between the near-UV and the near-IR is clearly shown in the spectrum of the irradiated AMES-Dusty planet. Even at 0.1AU, the planet reflects a considerable amount of radiation in the optical bands compared to the non-irradiated planet. However, the ratio (ϵ) of the planet flux to that of the incident flux is quite small. Averaged over 4500 to 5200Å,

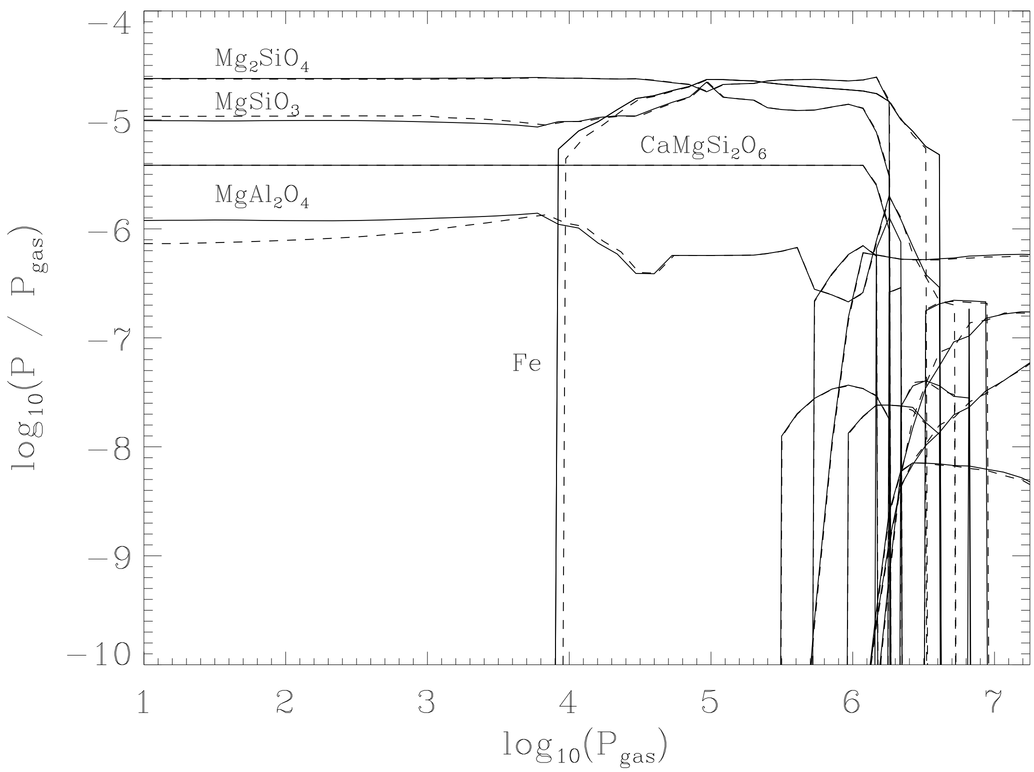

Figure 3.2: Concentrations of several important condensates for the irradiated (solid lines) AMES-Dusty (T_{int} = 500K, log(g) = 3.5) planet when located 0.05AU from a dM5. For comparison, the non-irradiated concentrations are also shown (dashed line).

ϵ is about 10^{-7} for the AMES-Dusty at 0.05AU. In the IR, the flux also increases and the molecular bands become progressively shallower as the planet approaches the primary. The increase in flux at infrared wavelengths is *not* due to reflection, but is entirely a thermal effect.

The effects of irradiation on the spectrum of the 500K AMES-Cond planet are also shown in Figure 3.3. Distinct molecular bands, primarily due to water and methane, are clearly visible for $\lambda > 1\mu$m. These bands are sensitive to the temperature at various depths. The methane absorption (at $\sim 1.8\mu$m, $2.2 - 3.0\mu$m and 3.1 – 4.0 μm) probes the deeper layers and indicates that, up to 0.1AU, little change in the temperature has taken place in the photosphere. Once 0.05AU separation has

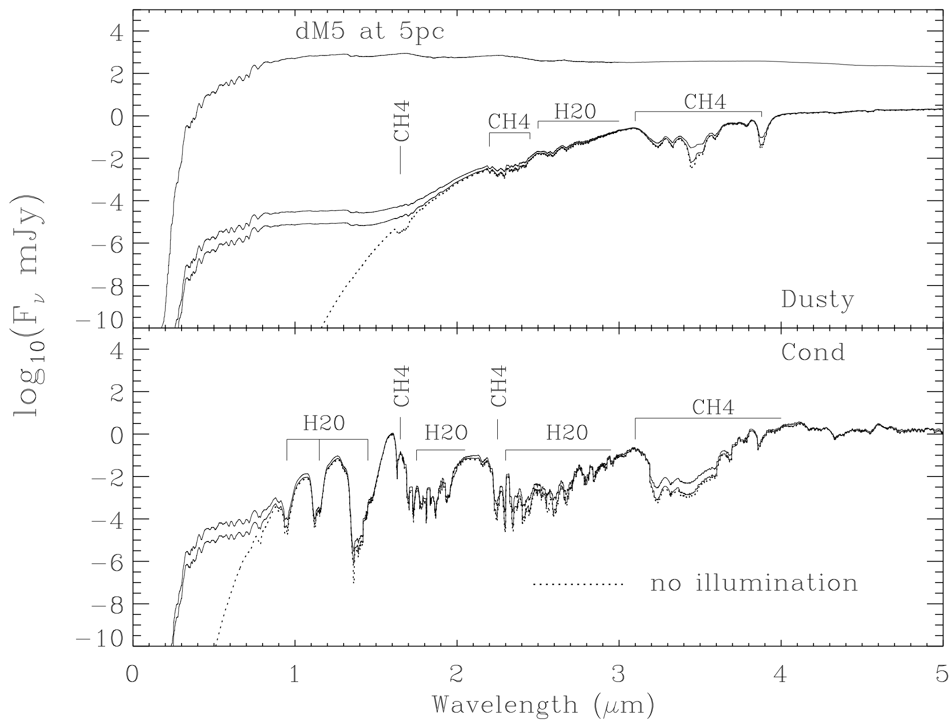

Figure 3.3: Above are the spectra corresponding to the structures shown in Fig. 3.1. For comparison, the spectrum of the dM5 used as the source of irradiation is also shown. All fluxes have been scaled appropriately for the size of the planet (or primary) and have been scaled to a distance of 5 parsecs. AMES-Dusty is shown on top and AMES-Cond on the bottom panel. Note that all spectra have been heavily smoothed reducing the resolution from ~ 1Å to ~ 50Å.

been reached, the irradiation has produced a much larger temperature rise resulting in nearly an order of magnitude increase in the emerging flux at 3.5μm. Similarly, the water bands (at 0.9μm, 1.1μm and 1.4μm) probe the upper layers and are sensitive to the irradiation even at 0.1AU. The AMES-Cond model also produces a reflected component in the UV and optical regions, though less dramatic than in the Dusty model when compared to the non-irradiated planet's intrinsic flux. In this case, $\epsilon = 3.6 \times 10^{-6}$ at 0.05AU, which is roughly 10 times that seen in the Dusty model.

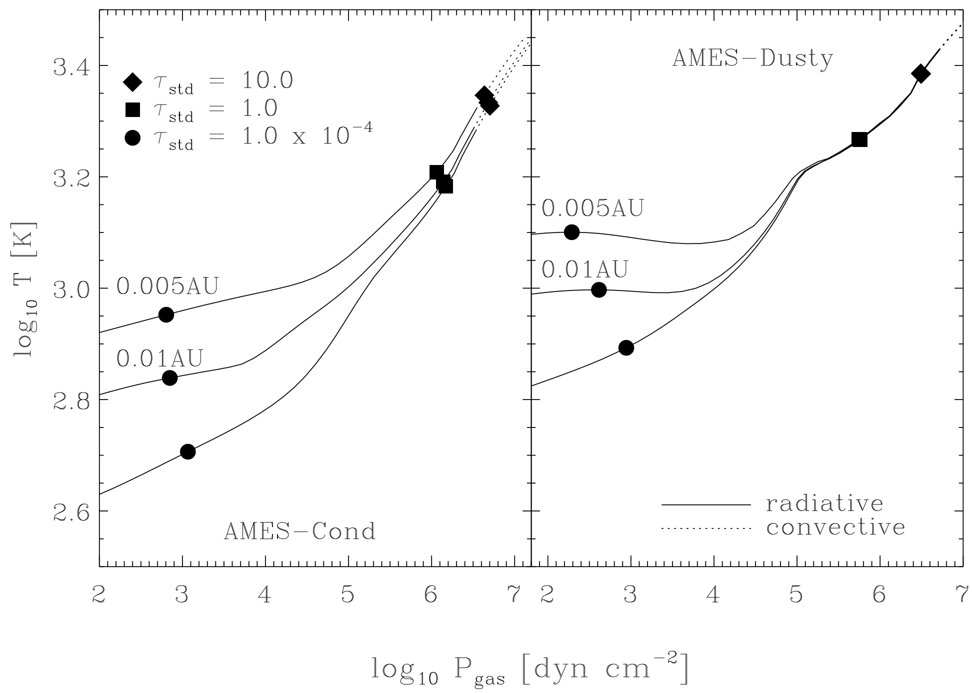

Figure 3.4: Same as Fig. 3.1, but now for the younger non-irradiated and irradiated planet (T_{int} = 1000K, $\log(g)$ = 3.5) when located 0.01 and 0.005AU from a dM5. AMES-Cond is shown on the left and AMES-Dusty on the right. As in Fig. 3.1, the lowest curve in each panel is the non-irradiated structure. The filled symbols refer to different optical depths (τ) at $\lambda = 1.2\mu$m.

It is quite possible that many of the young EGPs have T_{int} closer to that of an L or T dwarf. To investigate this possibility, we have modeled an EGP with T_{int} = 1000K (all other parameters are the same as for the above 500K planet) irradiated by the same dM5 used above. The results are qualitatively similar but weaker, for both the Cond and Dusty situations, than those of the previous cooler planets. So, in order to explore the regime where irradiation effects become important, we must study these planets at even smaller orbital separations. Figures 3.4 and 3.5 demonstrate the effects of irradiation on the structure and spectrum, respectively, for the 1000K AMES-Dusty and AMES-Cond models. As with the cooler dusty planet, the inner regions are not affected by the irradiation even at 0.005 AU ($\sim 1R_\odot$), a separation

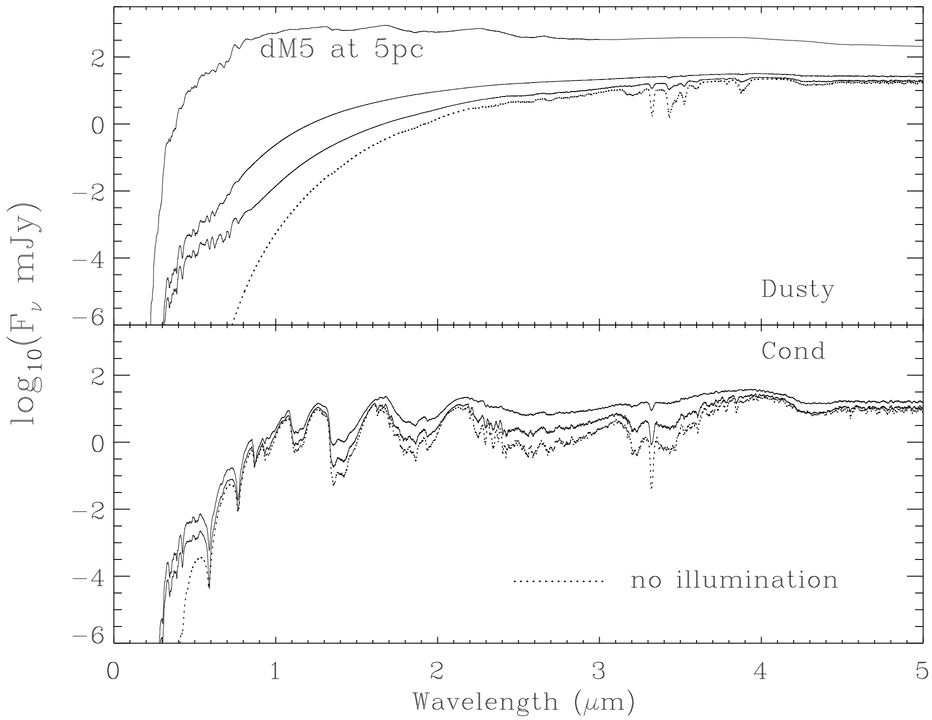

Figure 3.5: Above are the spectra for the structures shown in Fig. 3.4. For comparison, the spectrum of the dM5 is also shown. All spectra have been scaled as indicated in Fig. 3.3.

more common in cataclysmic variables. The AMES-Dusty spectrum (Fig. 3.5) is featureless in the IR for separations < 0.01AU, but many of the absorption lines present in the dM5 are now reflected in the optical spectrum of the planet. The AMES-Cond planet experiences a significant temperature increase at all photospheric layers (Fig. 3.4) and a suppression of the convective zone also seen in the cooler AMES-Cond planet. The spectra (Fig. 3.5) show several orders of magnitude increase in the flux for the methane and water bands at 0.01AU with many reflected atomic features in the optical when the Cond planet is at 0.005AU from the primary.

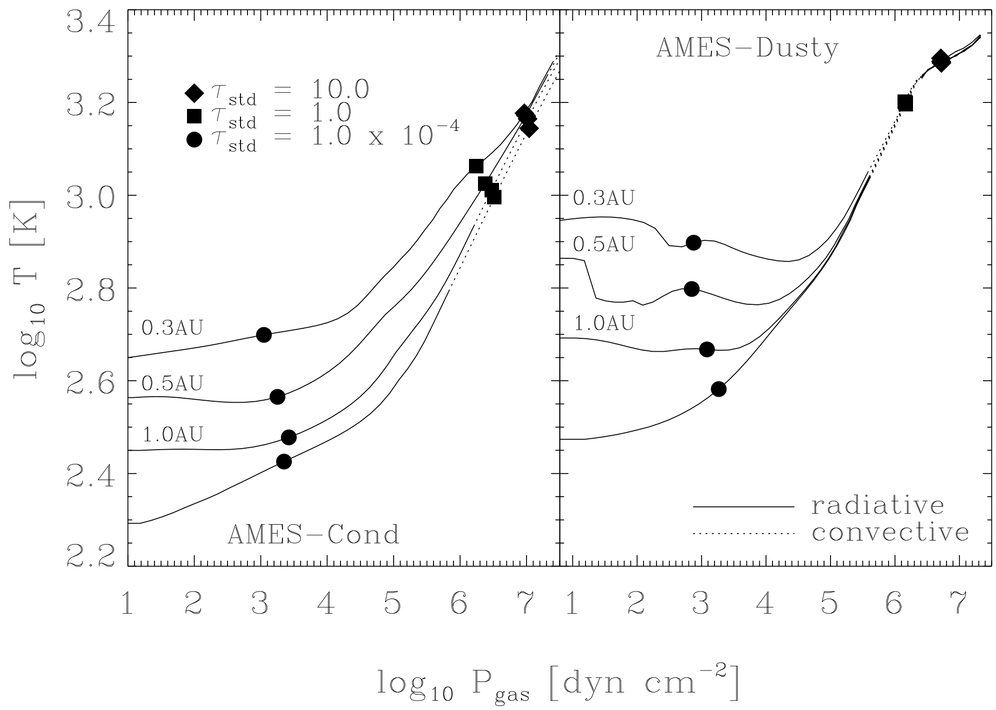

Figure 3.6: Structures for the non-irradiated and irradiated (T_{int} = 500K, $\log(g)$ = 3.5) planet when located 1.0, 0.5 and 0.3AU from a G2 primary.The filled symbols refer to different optical depths (τ) at $\lambda = 1.2\mu$m.

3.3.2 EGPs Around Solar Type Stars

Many EGPs have been discovered orbiting solar type stars (e.g., 51 Peg b), and have already received much attention in the literature in both observational and theoretical studies. Recent works include models of 51 Peg b (Goukenleuque et al., 2000), HD209458b (Seager & Sasselov, 2000) and a study of EGP photometric and polarization properties (Seager et al., 2000). We have taken a slightly more general approach; we do not focus on any one particular known object. We have chosen, instead, a planet with T_{int} = 500K and a young planet with T_{int} = 1000K orbiting an object similar to the Sun as average representatives of most currently known EGPs orbiting F, G, and K stars.

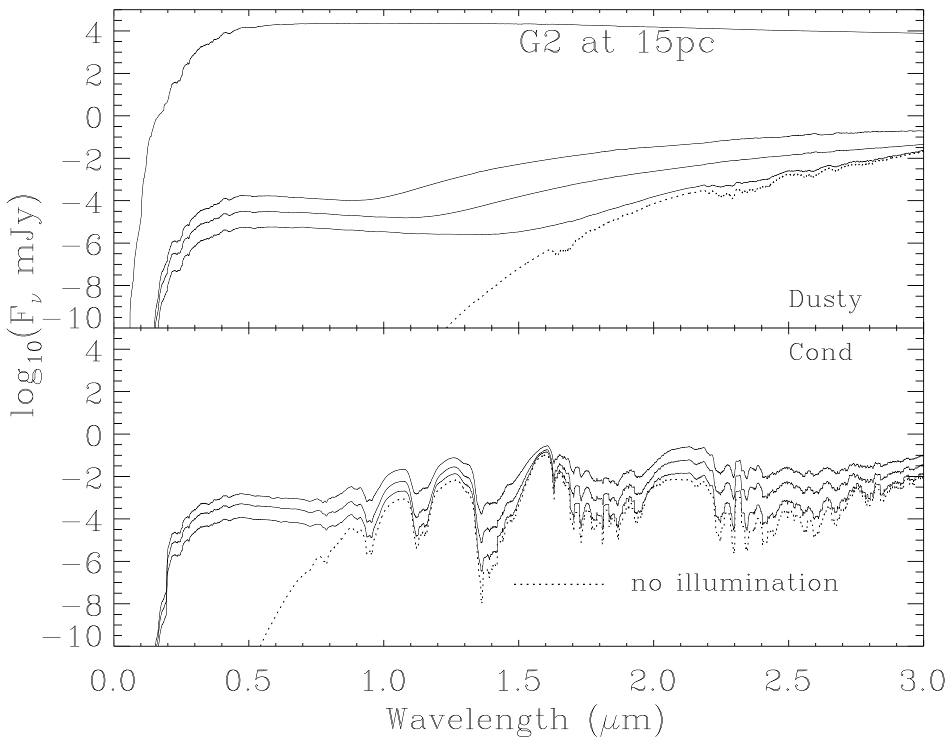

Figure 3.7: Spectra for the structures shown in Fig. 3.6. All spectra have been scaled and smoothed as indicated in Fig. 3.3. In both panels, the lowest spectrum (dotted line) corresponds to the non-irradiated planet.

Figure 3.6 demonstrates the effects of impinging radiation from a G2 primary on the 500K AMES-Cond and AMES-Dusty atmospheric structure for several separations. As in the dusty cases presented above, the inner part of the AMES-Dusty atmosphere is unaffected by the irradiation. However, regions around $\tau_{\rm std} \sim 10^{-4}$ show a dramatic rise in temperature as the planet is moved from 1.0 to 0.3AU. At 0.3AU, the Dusty model reaches $T_{\rm eq} = 767$K and the temperature in the upper atmosphere ($\tau_{\rm std} < 10^{-4}$) has more than doubled. Also at 0.3AU, the AMES-Cond model reaches $T_{\rm eq} = 735$K and, for regions near $\tau_{\rm std} = 1$, the temperature has risen by over 150K. Even the deepest layers feel the presence of the primary. The temperature at $\tau_{\rm std} = 10$ increases by 100K, and the boundary between the radiative and convective zone, which was well above $\tau_{\rm std} = 1$ at 1.0AU, has retreated to nearly

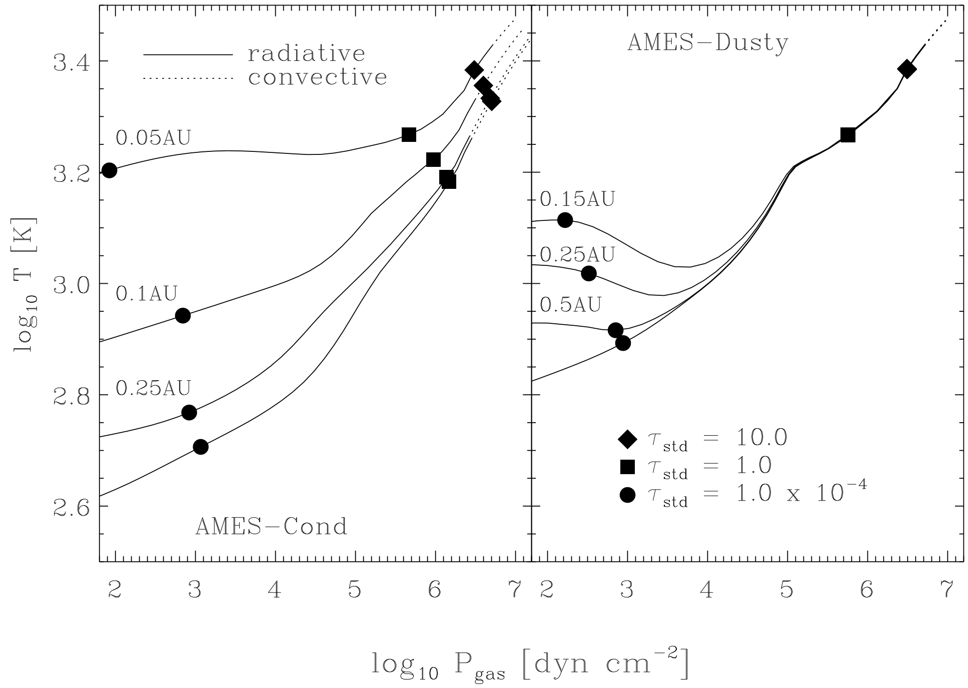

Figure 3.8: Structures for the non-irradiated and irradiated (T_{int} = 1000K, $\log(g)$ = 3.5) planet when located near a G2 primary. AMES-Cond is shown on the left for 0.25, 0.10 and 0.05AU separations and AMES-Dusty is shown on the right for 0.5, 0.25, and 0.15AU separations. The filled symbols refer to different optical depths (τ) at $\lambda = 1.2\mu$m.

τ_{std} = 50. Large concentrations of dust species are still capable of forming in the upper atmosphere. In the AMES-Dusty model, at 0.15AU, there still remains a thick cloudy region with concentrations similar to those seen in the 500K planet near a dM5 (see Fig. 3.2). The only major difference being Fe which extends to the upper regions where $\log(P_{gas}) \sim 1.0$ dynes cm^{-2}.

The optical and IR regions of the spectrum for each orbital separation are shown in Figure 3.7 where the differences between the AMES-Dusty and AMES-Cond models can clearly be seen. The dusty models produce very smooth spectra except for the reflected features in the optical bands. The dust is entirely responsible for the reflection effects in this case. As the dusty planet is brought closer to the G2,

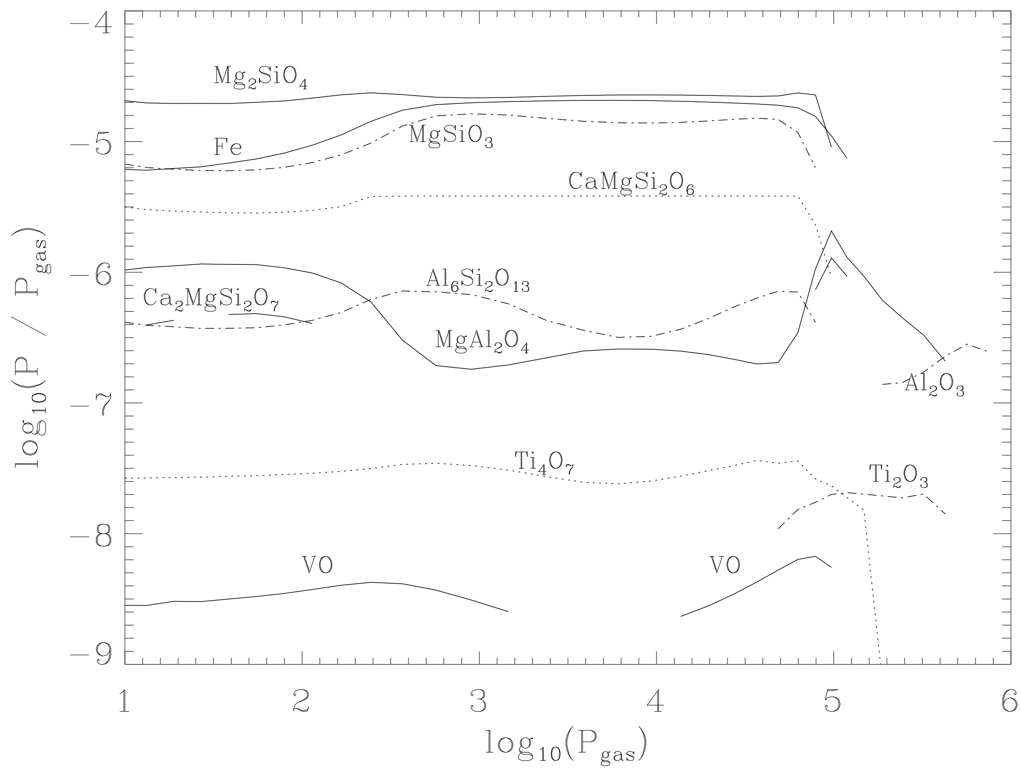

Figure 3.9: Concentrations of several important condensates for the irradiated AMES-Dusty (T_{int} = 1000K, log(g) = 3.5) planet when located 0.15AU from a G2 primary.

the few absorption features (primarily CH_4) seen in the non-irradiated planet completely disappear. At 0.5AU, very little change has taken place for $\lambda > 7000$Å in the Cond model spectrum and the water and methane bands remain strong. However, for $\lambda \leq 7000$Å, a large amount of reflected light is already present even at 0.5AU. As the planet is brought closer to the primary, the reflected light around 5000Å steadily increases. Nearly all ($\sim$ 95%) of the light reflected by the Cond model is due to Rayleigh scattering by the two most abundant species, H_2 and He. At 0.3AU nearly 10^7 times more light emerges from the planet around 5000Å, however it remains very faint compared to the incident radiation with $\epsilon = 2 \times 10^{-7}$ between 4500 and 5200Å.

The younger T_{int} = 1000K planet behaves in a similar manner as in the cases near a dM5 presented in section 3.3.1. The structure of the AMES-Cond planet, displayed in Figure 3.8, shows a significant suppression of the convective zone (below $\tau_{\rm std} = 10$ at 0.05AU) and the temperature has increased by a factor of 3 at $\tau_{\rm std} = 10^{-4}$. The Dusty model also shows a large temperature inversion above $\log(\mathrm{P_{gas}}) = 3.0$ dynes cm^{-2}. As can be seen in Figure 3.9, the Dusty model at 0.15AU exhibits a complex mixture of cloud species throughout the atmosphere. Fe, Mg_2SiO_4, and $MgSiO_3$ are the most prominent species except for the deeper layers where $CaMgSi_2O_6$ begins to dominate. The spectra, shown in Figure 3.10, display similar results as in the previous cases. However, at 0.05AU, the molecular bands have nearly disappeared in the Cond model and the once broad Na I and K I doublets (5890 and 7680Å) are extremely weak. Figure 3.11 shows, in more detail, the steady reduction in equivalent width of both lines for the AMES-Cond models. The decrease in equivalent width is almost entirely due to the changes in thermal structure shown above. At 0.05AU, the Cond planet has reached $\mathrm{T_{eq}} = 1752$K.

3.4 Discussion

3.4.1 Importance of Self-consistent Models

Many previous studies have used the structures of non-irradiated planets with $\mathrm{T_{eff}} = \mathrm{T_{eq}}$ and simply computed a spectra (or albedos) which included the incident flux and neglected the effects on the structure and chemical composition (Marley et al., 1999). This procedure will, however, result in gross errors in the emergent flux from the optical to infrared. In Figure 3.12, we compare the thermal spectrum of the self-consistent irradiated (AMES-Cond, $\mathrm{T_{int}} = 1000$K) planet at 0.065AU from a G2 star to that of a non-irradiated AMES-Cond model with an equal amount of thermal flux (i.e., $\mathrm{T_{eff}} = \mathrm{T_{eq}}$). Based on the irradiated spectrum without the reflected component, we estimate that $\mathrm{T_{eq}} = 1560$K. The non-irradiated model significantly underestimates the flux in the water and methane bands and overestimates the flux

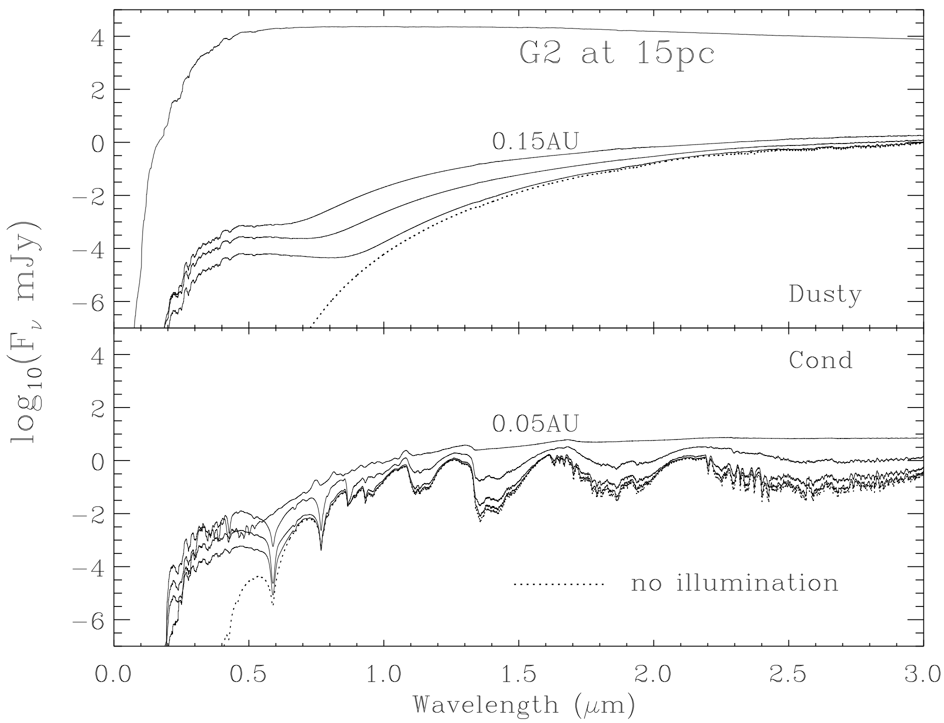

Figure 3.10: Spectra for the structures shown in Fig. 3.8. All spectra have been scaled and smoothed as indicated in Fig. 3.3. In both panels, the lowest spectrum (dotted line) corresponds to the non-irradiated planet.

in the regions outside the molecular bands. Also, the non-irradiated model overestimates the amount of reflected light blueward of 6000Å by $\sim 35\%$. Atomic features are also affected as can be seen for the Na I D line (Fig. 3.12) where the equivalent width is overestimated in the non-irradiated model even when the reflected light is included in the spectrum calculation. The differences between the structures (see Fig. 3.13) are just as striking. As might be expected, the non-irradiated model is still cooler (by 350K) than the irradiated model in the upper atmosphere ($\tau_{\rm std} \sim 10^{-4}$). At deeper layers the two structures actually intersect and, at $\tau_{\rm std} \sim 10$, the non-irradiated model is *hotter* than the irradiated model by roughly 350K. An even more apparent difference is the location of the boundary between the radiative and convective regions. In the non-irradiated model, the convective zone reaches layers

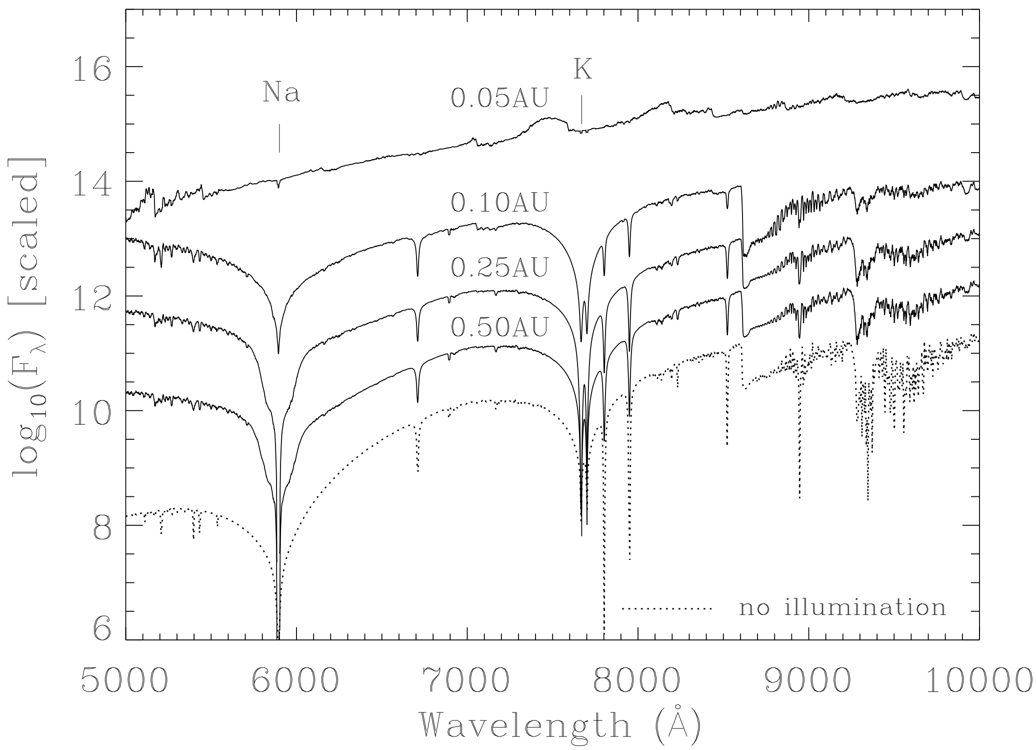

Figure 3.11: Same AMES-Cond spectra as in Figure 3.10 but focusing on the Na and K doublet features. The spectra have been arbitrarily scaled for comparison.

above $\tau_{\rm std} = 1.0$ while in the irradiated case, the convective zone has retreated to layers below $\tau_{\rm std} = 10.0$. These differences, between a non-irradiated structure with $T_{\rm eff} = T_{\rm eq}$ and a structure based on a self-consistent inclusion of the impinging radiation, will have significant consequences for any interior and evolution calculations of irradiated planets.

3.4.2 Limiting Effects of Dust

The question of how much energy is redistributed by "weather patterns" is extremely important, and affects the upper boundary condition for irradiated models. To answer this question, 3D dynamical models of grain growth and diffusion would be needed. In this work, we explore the limiting effects of these patterns with Cond models, corresponding to clear skies, and Dusty models corresponding to cloudy

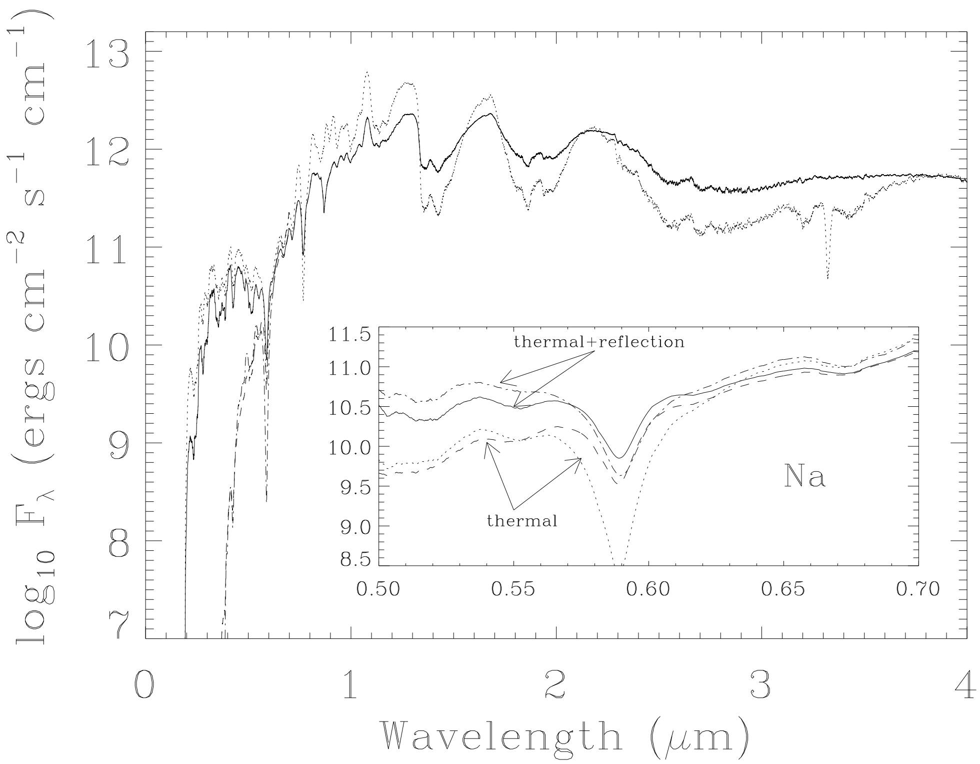

Figure 3.12: The spectrum for our 1000K AMES-Cond planet located at 0.065AU from a solar type primary is shown above with (solid line) and without (dashed line) the reflected component. Based on the irradiated spectrum without the reflected component, we estimate that $T_{eq} = 1560K$. We also show a non-irradiated (AMES-Cond, $T_{eff} = T_{eq}$) model with (dashed-dotted line) and without (dash line) a reflected component. Clearly the hotter non-irradiated model is a poor substitute for the true irradiated case.

skies. We find that irradiated Cond and Dusty models yield systematically different thermal spectra. The infrared spectra of Dusty and Cond planets around M dwarfs are affected by the impinging radiation only for extremely small orbits. However at separations around 0.05AU from a G2 star, the substellar point (the point on the planet closest to the star) will have a nearly featureless spectrum even in the Cond limit. The lack of spectral features is a consequence of the structure becoming nearly isothermal and is not a result of any significant decrease in abundances.

The emergent flux from both our irradiated and non-irradiated models indicates that Cond atmospheres are brighter at optical wavelengths than Dusty atmospheres.

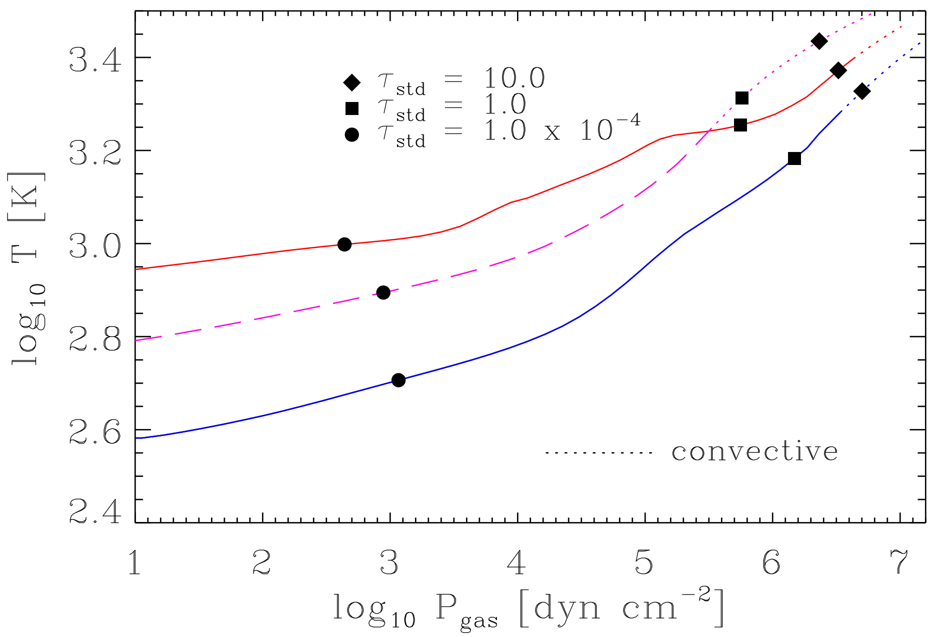

Figure 3.13: The structures for our 1000K AMES-Cond planet located 0.065AU from a solar type primary (top solid line) is compared to a non-irradiated structure of an AMES-Cond planet with $T_{\rm eff} = T_{\rm eq} = 1560$K (dashed line). The errors which result from assuming a non-irradiated structure are quite apparent at *all* depths. For comparison, the non-irradiated 1000K AMES-Cond planet is also shown (bottom solid line). The filled symbols refer to different optical depths (τ) at $\lambda = 1.2\mu$m.

In general, Cond models are much brighter than the Dusty cases simply because the dust opacity blocks most of the thermal radiation (for more details, see Allard et al., 2001). When incident radiation is present, the dust grains reflect large amounts of light while continuing to block most of the *intrinsic* optical flux. Irradiated Cond atmospheres remain very transparent and allow large amounts of flux to emerge from the deep hotter layers. When this intrinsic thermal radiation is combined with the reflected flux, the irradiated Cond model appears brighter than the Dusty model.

The fraction of the stellar light reflected by our Cond model (at 0.05AU from a G2) around 4900Å is less than 5×10^{-6}. This is well below the results published by Cameron et al. (1999) and the upper limit published by Charbonneau et al. (1999). Also, the strong color dependence of Rayleigh scattering causes the reflected optical

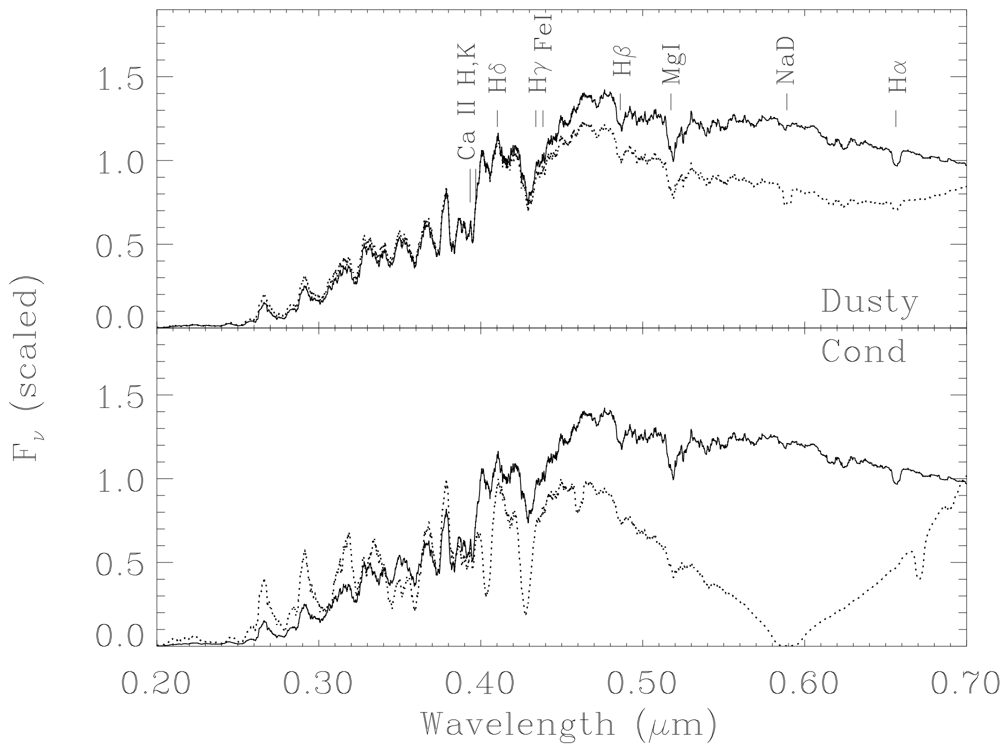

Figure 3.14: The optical spectrum of a T_{int} = 1000K planet (dotted line) located at 0.15AU from a G2 primary is compared to the incident stellar spectrum (solid line). The top panel shows the comparison for a Dusty atmosphere and the Cond case is shown in the lower panel. The fluxes have been normalized to one at 4000Å to facilitate the comparison.

light (scattered by H_2 and He) in the Cond models to be considerably different from the optical spectrum of the primary. However, the reflected light in the Dusty atmospheres is due almost entirely to Mie scattering which is a fairly grey process. The result is a near reflected copy of the stellar optical spectrum. A comparison between the stellar light and the reflected optical spectrum for a T_{int} = 1000K planet located at 0.15AU from a G2 primary can be seen in Figure 3.14. For wavelengths less the 4500Å, the reflected light in the Dusty model matches closely the stellar light. At redder wavelengths, the two spectra differ not only in the slope of the continuum, but also in the depth of Hα and the Na I doublet at 5890Å. The Cond model has a very different optical spectrum with the redder wavelengths being dominated by an extremely broad Na I doublet (5890Å). In general, the two spectra have little in common. Recent attempts have been made (Cameron et al., 1999; Charbonneau et al., 1999) to observe a Doppler shifted copy of the stellar light reflected by the planet orbiting τ Boo. Figure 3.14 suggests that planets in the Cond limit would be poor candidates for such techniques. Dusty planets, however, are clearly better choices and observations at shorter wavelengths may be more fruitful. In either case, observations similar to those of Cameron et al. (1999) and Charbonneau et al. (1999) could help determine the Cond or Dusty nature of EGPs.

3.4.3 Energy Redistribution

Clearly the fraction of the irradiated face seen by an observer depends on orbital phase and inclination. In addition, the planet's atmospheric structure will likely vary across the planet's surface. Guillot et al. (1996) claimed that one could assume that the radiation received by the planet's day side is quickly redistributed over the entire planet surface. However, a recent calculation by Guillot (2000) indicates that this redistribution may take place over longer time-scales ($\sim 10^5$ seconds) than previously thought. This would imply that there exists, in those planets which are tidally locked, a large temperature difference between the day and night sides. Furthermore, if such a difference existed, the structure of the irradiated face would vary as a function of latitude and longitude and should approach the structure of the non-irradiated face for regions near the terminator[2]. Therefore, it is unlikely that an irradiated planet can be characterized by a single 1-D plane parallel model atmosphere. Though it is reassuring that our results agree qualitatively with those of previous studies (Seager & Sasselov, 1998; Seager et al., 2000; Goukenleuque et al., 2000), to accurately predict the spectrum and reflected light as a function of inclination and phase will require, at the very least, many 1-D models each accounting

[2]The terminator is the line dividing night and day on a planet.

for the different amounts of energy deposited on the planet's day side at various longitudes and latitudes. We are currently working on a sequence of non-isotropic irradiated models which include only the incident flux that a certain latitude[3] would receive. With such a sequence, we would be capable of modeling the reflected light for any phase and inclination.

Many of the recent studies (Marley et al., 1999; Seager & Sasselov, 2000; Seager et al., 2000; Goukenleuque et al., 2000; Sudarsky et al., 2000) have made the assumption that the planet receives an amount of energy equal to $\pi R_p^2 F^{inc}$ which is quickly redistributed (Guillot et al., 1996) over the entire planet surface. As a result, these previous works have essentially included the minimum amount of external flux ($\frac{1}{4}F^{inc}$) that could be received by a planet at a given separation. If the more recent calculation by Guillot (2000) is correct and global redistribution is inefficient, then the models in these previous studies would be valid only for separations larger than what the authors had originally intended and only for a specific ring around the substellar point. In our calculations, we have assumed no redistribution and therefore have included a much larger amount of external flux (F^{inc}). Despite the assumption of an isotropic external radiation field, we feel that our models adequately represent the substellar point where this assumption is more reasonable.

3.4.4 Transmission Spectra

In the recent study by Seager & Sasselov (2000) an attempt was made to model the transmitted flux of HD209458b (recently shown to be an eclipsing system) through the upper regions of the planet's atmosphere. Seager & Sasselov (2000) assumed that the structure at the poles (and along the terminator) was the same as that given

[3]For this purpose, we assume that the symmetry axis is a line connecting the planet and primary. In this context, lines of constant latitude would refer to concentric rings about the substellar point.

by their fully irradiated model. However, the planet receives only a small amount of incident flux at the terminator and only in the upper atmosphere. In the absence of strong energy redistribution, the terminator would have a structure more closely resembling that of the non-irradiated face.

For a transmission study, one must calculate the stellar flux passing through a thin region at the top of the planet's atmosphere ($\sim 0.01\mathrm{R}_p$ thick) which includes latitudes above 82°. While, in general, EGPs are adequately described by plane parallel geometry, as one approaches the limb, the plane parallel assumption becomes increasingly less accurate. Using plane parallel geometry to calculate the transmitted spectrum assumes that the stellar flux passes through a region of constant thickness and height (a slab). In reality, the flux is passing through a section of a sphere encompassing the limb, in which case, rays entering at different latitudes will pass through different amounts of the planet's atmosphere. A simpler and more accurate way of calculating the transmitted flux is to solve the spherically symmetric radiative transfer equation (SSRTE) and take, as the transmitted flux, the average intensities for direction cosines which pass through this band. The main advantage over the plane parallel solution is that the correct geometry is automatically built into the SSRTE. When solving the SSRTE, the atmosphere is modeled as a discrete number of concentric shells surrounding the interior (or core). The transfer equation is then solved along characteristics which are divided into two categories: those which reach the core (core intersecting) and those which do not (tangential). Along a given characteristic, the direction cosine is now a function of depth whereas in the plane parallel case it is constant. Also, the diffusion approximation must hold at the inner boundary for the core intersecting characteristics but *not* for the tangential characteristics. The solution along the tangential characteristics which pass through the outer most shells is all that is needed to calculate the transmitted flux and will already account for the curvature of the limb.

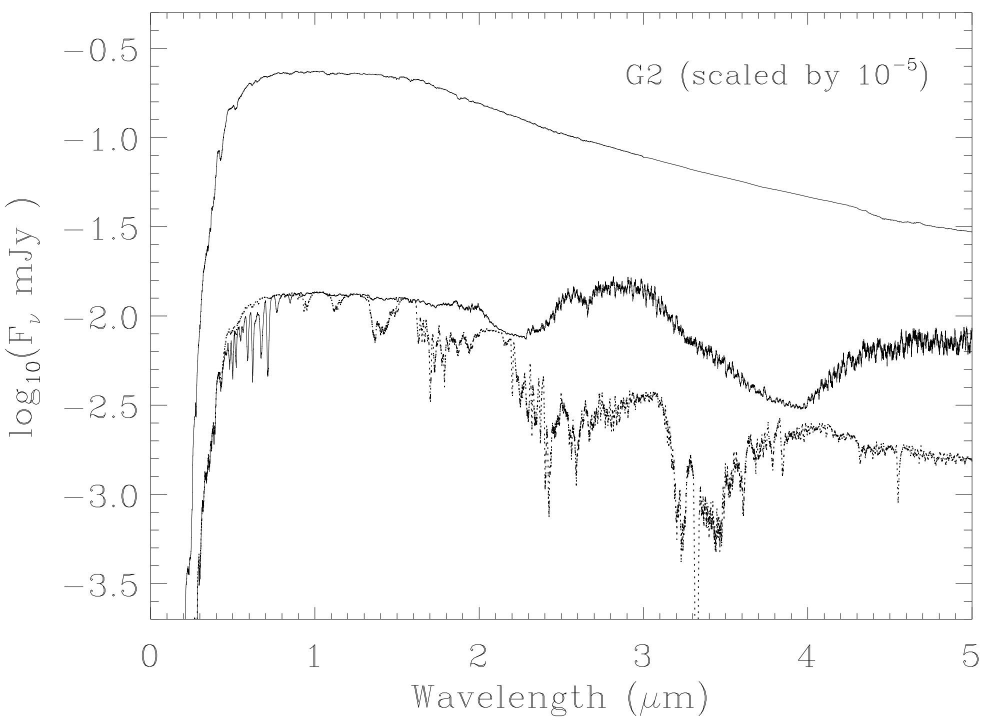

Figure 3.15: The transmitted flux through the limb of a 1000K AMES-Cond planet located 0.05AU from a G2 primary. The second spectrum(full line) is the transmitted flux through our irradiated atmosphere. The bottom spectrum(dotted line) is the transmitted flux through our non-irradiated atmosphere. All spectra have been scaled to 15pc. For comparison, the spectrum of a G2 (top line scaled by an additional 10^{-5}) is also shown. If the deposited energy is not globally redistributed on short time-scales, then the transmitted flux should be closer to the non-irradiated case. Reality is likely to be somewhere in between.

Consider again the 1000K AMES-Cond planet located 0.05AU from a G2 primary and imagine that we observe the planet at (or near) inferior conjunction. Under such conditions one would observe a brighter planetary limb due to the transmitted stellar flux. In a spherically symmetric geometry, the effect emerges from the model in a very natural and physical manner. In Figure 3.15, we compare the transmitted flux for two different structures: our fully irradiated AMES-Cond structure ($T_{eq} = 1633$K) and the non-irradiated model ($T_{eff} = 1000$K). In both cases, the planet leaves its mark on the stellar flux as it passes through the planetary limb in the form of much stronger absorption features than seen in the unpolluted stellar spectrum. The transmitted spectrum based on the irradiated structure peaks at 3μm, but the non-irradiated planet (see Fig. 3.10) is still 100 times brighter in this region and over 10^5 times fainter than the primary. In both cases, the planet's limb is $\sim 10^3$ times brighter between 4500 and 5000Å than the planet's night side. However, the disk of the G2 dominates the optical spectrum and is $\sim 10^6$ times brighter than the planet's limb.

3.5 Conclusions

In this paper we have presented atmospheric models of planets in the presence of strong impinging radiation from primaries of different spectral type and at various orbital separations. We have also studied the effects of irradiation in two limiting cases: efficient settling (accounting for the depletion of elements by condensation) and complete cloud coverage.

Irradiation has only small effects on the atmospheres of planets with dM primaries except for extremely close orbits. For an object like Gl876B, which orbits a dM4 at 0.2AU, it is unlikely that any irradiation effects will be observed. However, for planets in the Cond limit orbiting G2 primaries, the effects are non-negligible. The upper layers of the atmospheres are significantly heated by the impinging radiation even at 0.5AU in both the Cond and Dusty limits. The inner layers of the Cond models also experience considerable heating and a suppression of the radiative-convective boundary. The innermost layers of the Dusty models are essentially unaffected by the irradiation even for close orbits. These results will have strong implications for interior and evolution calculations. The heating of the inner layers in the Cond limit can bring the temperatures at the bottom of the atmosphere close to those in the Dusty limit. This would suggest that, in certain situations, the interior models would no longer depend on the Dust-Cond uncertainty published by Chabrier et al.

(2000). However, it is still important that detailed interior and evolution models be calculated which use irradiated atmospheres to set upper boundary condition.

The existence of "weather patterns" on EGPs in the form of strong zonal winds and clear, cloudy or partly cloudy skies, will greatly influence the effects caused by irradiation. Our models indicate that an EGP with significant cloud coverage will reflect a copy of the stellar optical light while EGPs with clear skies will have very different reflected spectra. We have also found that young EGPs with clear skies are actually brighter in the optical than cloudy EGPs despite the more efficient reflective properties of dust. In general, our models indicate that observations would need to be sensitive to variations in the planet+star spectrum on the order of 10^{-5} to 10^{-6} in order to disentangle the reflected or transmitted flux.

It is apparent from observations of Jupiter and the other Jovian planets that clouds are *not* homogeneously distributed over the surface and that complex weather patterns persists. There is also evidence (from Galileo) that, unlike our simplified dusty models, clouds form in thin decks and any condensation occurring at the uppermost layers would soon "rain" out onto the lower atmosphere possibly instigating a cascade of diffusive settling (Encrenaz, 1999). A self-consistent treatment of this behavior is currently being added to `PHOENIX` and results for both irradiated and non-irradiated atmospheres will be presented in future papers. Until these results are available, the models presented above are representatives of clear (AMES-Cond) and completely cloudy (AMES-Dusty) skies. It is possible to combine our Dusty and Cond models to investigate the intermediate "partly cloudy" cases.

Though it is unlikely that any of the models produced thus far are exact representations of a currently known EGP, one may hope that our predictions and those of others will aid observers in making the much needed detailed observations of EGPs.

Chapter 4

Non-LTE Effects of Na I in the Atmosphere of HD209458b[1]

4.1 Introduction

HD209458b is the first extra-solar giant planet (EGP) observed to transit its parent star (Charbonneau et al., 2000; Henry et al., 2000) and, consequently, its mass (0.69 $M_{\rm Jupiter}$) and radius (1.35 $R_{\rm Jupiter}$) are known to a high degree of accuracy. These results leave little doubt that HD209458b is a gas giant. and its special orbital inclination has drawn a great deal of attention from observers and theorists over the past year. Recently, an increase in the sodium absorption (relative to the continuum) at 5893Å was observed with the Hubble Space Telescope (HST) during several transits of HD2094598 (Charbonneau et al., 2002). The additional sodium absorption is believed to be due to Na D absorption in the EGP's atmosphere as stellar light passes through the planetary limb. This observation marks a major turning point in the study of EGPs, for now we have direct evidence of an atmosphere around HD209458b and a measurement of one chemical species (Na). According to Charbonneau et al. (2002), the HST observations suggest that either the EGP atmosphere has a low concentration of neutral atomic Na (due to photoionization, molecular formation, or an overall low metallicity) or that high altitude clouds exist and reduce the amount of stellar flux transmitted though the EGP limb.

[1] Barman, T. S., Hauschildt, P. H., Schweitzer, A., Stancil, P. C., Baron, E. and Allard, F. 2002, *The Astrophysical Journal*, 569, L51. Reprinted here with the permission of publisher.

Table 4.1: Model parameters for HD209458(b)

radius	1.35 $R_{Jupiter}$	1.146 $R_{\odot}$
mass	0.63 $M_{Jupiter}$	1.05 $M_{\odot}$
T_{eff}	1800 K	6000 K
[Fe/H]	0.00	0.00
semi-major axis	0.045 AU	

In this letter, we offer an alternate explanation for the observed Na absorption and explore the possibility that the Na D feature is altered by nonlocal thermodynamic equilibrium (NLTE) effects brought on by the impinging stellar radiation field and insufficient collisional thermalization. If true, NLTE effects would offer a natural explanation for the apparently low sodium absorption observed in the HD209458b without the need for excessive ionization, a reduced metallicity, or extremely high altitude clouds. Below we will present theoretical predictions for NLTE Na D doublet line profiles for the transmitted spectrum of an irradiated EGP atmosphere and provide stringent limits on the non-LTE effects.

4.2 Model Construction

The construction of the model atmospheres presented below follows the procedure outlined in Barman et al. (2001) (here after BHA). In order to make a direct comparison with HD209458b, we have adopted the best-fit values for the radius, mass, and orbital separation of HD209458b and its parent star published by Brown et al. (2001) and Mazeh et al. (2000) (see table 4.1). We have also assumed that the total flux received by the planet has been uniformly distributed over the planet's dayside. Therefore, the incident flux has been weighted by 0.5, whereas in the BHA models, no redistribution was assumed. The intrinsic effective temperature of the model (i.e. the effective temperature of the planet in the absence of irradiation) is 500K. However, this intrinsic temperature has little effect on the structure of the outer atmosphere which is completely determined by the incident flux. With this redistribution, our models represent an upper limit to the equilibrium effective temperature which is about 1800K. We further assume that the planet has a solar composition with an opacity setup identical to the “AMES-cond” models of BHA and Allard et al. (2001). In this situation, dust grains form in the atmosphere at locations determined by the chemical equilibrium equations but their opacity contribution is ignored, mimicking a complete removal of the grains by efficient gravitational settling. Therefore, the models in this study represent cloud free atmospheres.

We model the transmitted flux, which passes through the limb of the planet's atmosphere, by solving the spherically symmetric radiative transfer equation (SSRTE) suitably adjusted to account for the incident radiation. The incident flux is taken from a separate calculation which reproduces the observed spectrum of HD209458. The SSRTE has a significant advantage over the plane-parallel solution because a geometry more appropriate (and more accurate) for the upper atmosphere is already incorporated. When solving the SSRTE, the atmosphere is modeled as a discrete number of concentric shells surrounding the interior (or “core”). The solution along characteristic rays that pass through the outer most shells is all that is needed to calculate the transmitted intensities and automatically accounts for the curvature of the limb. The total transmitted flux is obtained by integrating over the planet limb:

$$F_{trans,\lambda} = \int_{R_{\min}}^{R_{\max}} I_\lambda(r) 2\pi r dr \tag{4.1}$$

where r is the perpendicular distance from the planet center to a tangential characteristic ray. $R_{\max}$ is the planet radius at $\tau_{\text{std}} = 0$ (τ_{std} is the optical depth at 1.2μm) and R_{min} is chosen such that for $r \geq R_{\min}$,

$$\left[\frac{I(r)}{I^\star(r)}\right]_{\lambda=5880\text{Å}} \geq 0.1, \tag{4.2}$$

where $I^{\star}$ is the incident stellar intensity. The lower limit in equation 4.2 ensures that the transmitted intensities are well sampled and light from the core region is excluded. Note that both $R_{\rm max}$ and $R_{\rm min}$ are determined by the simulation and depend on the resulting structure of the model atmosphere. The only prescribed radius is $R_{\rm p} = r(\tau_{\rm std} = 1)$, which is equal to the planet radius given in table 4.1. Typically, with the limit set by equation 2, we find that the thickness of the limb ($H = R_{\rm max} - R_{\rm min}$) is roughly $0.07R_{\rm p}$.

4.2.1 Na in non-LTE

When a gas is assumed to be in LTE, the level populations for each species depend entirely upon the gas temperature and electron pressure and are given by the Saha-Boltzmann distribution. In general, the LTE assumption is a matter of computational convenience and is not expected to be valid in most cases, especially in the optically thin regions of an atmosphere. However, it is often assumed that LTE is achieved in very late type stars (even Brown dwarfs) despite the fact that this assumption has not been thoroughly tested. Departures from LTE have previously been investigated for Ti I (Hauschildt et al., 1997) and CO (Schweitzer et al., 2000) for cool M dwarfs and for CH_4 in the Jovian planets (Appleby, 1990). These earlier works found that, for these particular species, NLTE effects were small.

Due to the close proximity of HD209458b to its parent star, the planet's atmosphere is subjected to intense stellar radiation. This inherently *nonlocal* source of radiation dramatically alters the conditions of the outer atmosphere compared to an isolated EGP. In addition, the cool atmospheres of EGPs are dominated by strong opacity sources like H_2O and CH_4 and, therefore, have intensities that differ greatly from those of a blackbody. When combined with the relatively low pressures of the outer atmosphere, these conditions very likely will lead to departures from LTE which may play an important role in determining the atmospheric structure and resulting spectrum. If LTE is to be achieved in EGP atmospheres, then the collisional rates must be large enough to compensate for the deviations of the radiative rates from their LTE values. Unfortunately, a limitation of all NLTE models is a lack of well determined collisional cross-sections for interactions with important species like H_2, He, and H. However, it is unlikely, given the low thermal velocities, that these particles could restore LTE completely. In fact, the effects of collisions with hydrogen on the Na D profile in M dwarfs with chromospheres are fairly small and electron collisions dominate despite the fact that $N_H/N_e \sim 10^6$ (Andretta et al., 1997).

The Na I model atom used in this work includes 53 levels, and 142 primary transitions (all bound-bound transitions with $\log(gf) > -3.0$) were included in the solution of the statistical equilibrium equations. For details of the method used to solve the rate equations, see Hauschildt & Baron (1999). As in Hauschildt et al. (1997) for Ti I, electron-impact bound-free collisional rates are approximated by the formula of Drawin (1961) and bound-bound collisional rates are based on the semi-empirical formula of Allen (1973) with permitted transitions determined from Van Regemorter's (1962) formula. For the ground-state photoionization cross sections, we have used the Opacity Project data of Bautista et al. (1998). We have also assumed complete redistribution.

We have constructed four model atmospheres and resulting transmitted spectra for HD209458b. The first irradiated model (A) only includes collisions with electrons, where the source of free electrons is primarily the ionization of potassium. Even in an irradiated EGP atmosphere, the number density of electrons is very small ($N_e/N_{\mathrm{H2}} \sim 10^{-8}$) and the temperatures are too low for electronic collisions to be important. Model A, therefore, can be considered a lower limit for the collisional rates. The second irradiated model (B) has the same parameters as model A, except that collisions with H_2 are also included. In order to place a secure upper limit on the

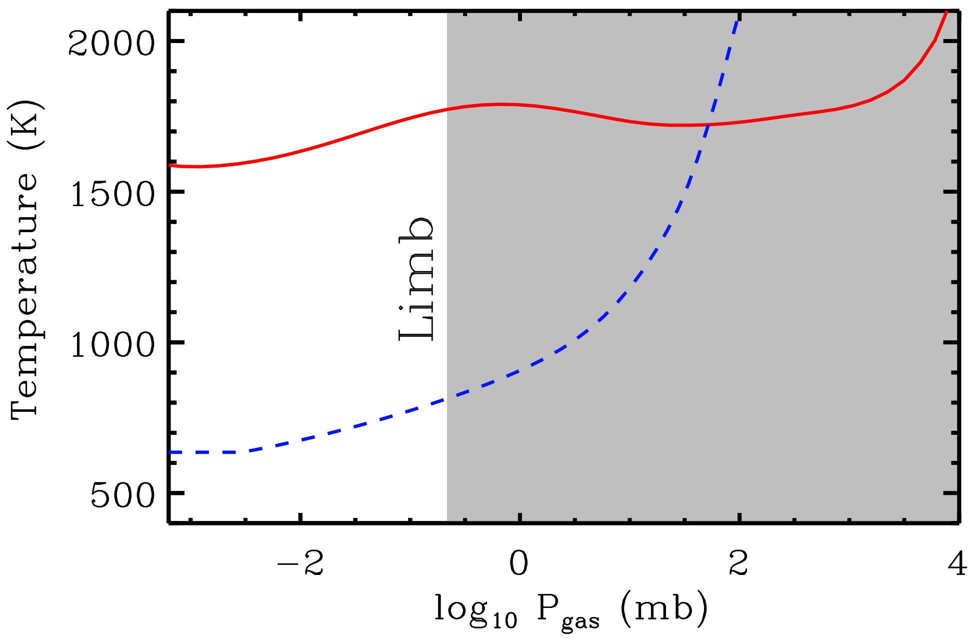

Figure 4.1: The temperature pressure profiles for the irradiated (solid line) and non-irradiated (dashed line) models. The unshaded area indicates the limb region for the irradiated models.

effects of collisions with H_2, we have treated H_2 as if it had the same rate coefficients as an electron. Assuming identical cross-sections implies that the rate coefficients scale with $(\mu)^{-\frac{1}{2}}$, where μ is the reduced mass of the collision partners. Therefore, we are overestimating the H_2 collisional rates by more than an order of magnitude. The remaining two models (C and D) represent *non*-irradiated atmospheres with the same effective temperature as the irradiated models ($\sim$ 1800K) and include the same lower (model C) and upper (model D) limits for the collision rates. Each of these model atmospheres was produced from a self-consistent solution of the SSRTE, chemical equilibrium equations, and the NLTE rate equations. We did not prescribe the temperature structure or mixing ratios for any of the species.

4.3 Results

The temperature-pressure profiles for models A and C are shown in figure 4.1. Note that, the profile for model B is identical to that of model A and model D has the same profile as model C. The gas pressures in the limb region are very low, ranging from 0.004mb to 0.2mb. As is to be expected, the non-irradiated models look nothing like the irradiated models which have temperatures nearly 1000K higher in the outer atmosphere (Barman et al., 2001; Goukenleuque et al., 2000; Seager & Sasselov, 1998). There were no significant changes to the temperature-pressure profiles in any of the four NLTE models compared to the LTE structures.

Departures of the level populations from LTE, for a particular species, are usually described by the departure coefficients, $b_i = n_i^\star/n_i$, where $n_i^\star$ is the NLTE population density for level i and n_i is the LTE value (Mihalas, 1970). In figure 4.2, we show the b_i's for the ground state (3s) and the first excited states ($3\mathrm{p}_{\frac{1}{2}}$, $3\mathrm{p}_{\frac{3}{2}}$) of the neutral sodium atom for several different physical conditions within the EGP atmosphere. The largest departures are seen in model A where the 3s (ground state) and 3p levels are both underpopulated by many orders of magnitude, especially in the limb region. The main reason for such large departures is that we have only included collisions with electrons and, in such a cool atmosphere, the number density of electrons is ~ 8 orders of magnitude below that of the dominant species, H_2. Consequently, there are essentially no collisions in model A to thermalize the level populations in the Na atom thus allowing the radiative rates to dominate and drive the system out of LTE. Also, since the upper atmosphere is dominated by a large external radiation source (which happens to peak near the Na D doublet, ~ 5000Å), the mean intensity of the line is much larger than the thermal source function which implies a strong decoupling of the radiation field from the local conditions. Furthermore, the ratio of the line source function to a blackbody is roughly given by the ratio of the departure coefficients of the upper (3p) and lower (3s) levels for the transition (Bruls et al., 1992). From figure 2, we see that the line source function is far from a blackbody for the majority of the upper atmosphere (since $b_{3p}/b_{3s} \gg 1$).

An obvious question to ask is whether the system will return to LTE if collisions with the dominant species (H_2) are included. Model B, which has the same parameters and temperature profile as model A, includes collisions with both electrons *and* H_2 (but assuming that H_2 has the same rate coefficients as an electron). In effect, we have increased the importance of electronic collisions by more than 8 orders of magnitude. As is expected, the departure coefficients are closer to one, but the level populations in the limb are still far from the LTE values. However, since $b_{3p}/b_{3s} \sim 1$ for most of the atmosphere, NLTE effects will only be important in model B for $\tau_{\rm std} < 10^{-4}$. The real situation is likely to be somewhere between models A and B.

We also show departure coefficients for non-irradiated models (C and D) with $T_{\rm eff}$ equal to the equilibrium effective temperature of the irradiated atmospheres (1800K) for both collisional rate limits. Despite the absence of any extrinsic radiation and much lower temperatures in the upper layers, the non-irradiated atmospheres still have departures from LTE, though generally less significant than those found in the irradiated atmospheres. Model C (the near collision free limit), has departures from LTE similar to those of the collision dominated irradiated model (B) for the ground state but with an over populated 3p level. With increased collisional rates, Na I has nearly returned to LTE for most of the atmosphere in model D with departures still present in the top most layers whereas in the irradiated case both levels were greatly underpopulated even in the collision dominated model (B).

The effects on the Na D line profiles are quite dramatic for model A (see figure 4.3). In this case, the lack of thermalization reduces the line transfer to nearly a pure scattering case. As a result, the doublet appears completely in emission. However, in model B, as the collisional rates are increased, the line wings return to their LTE

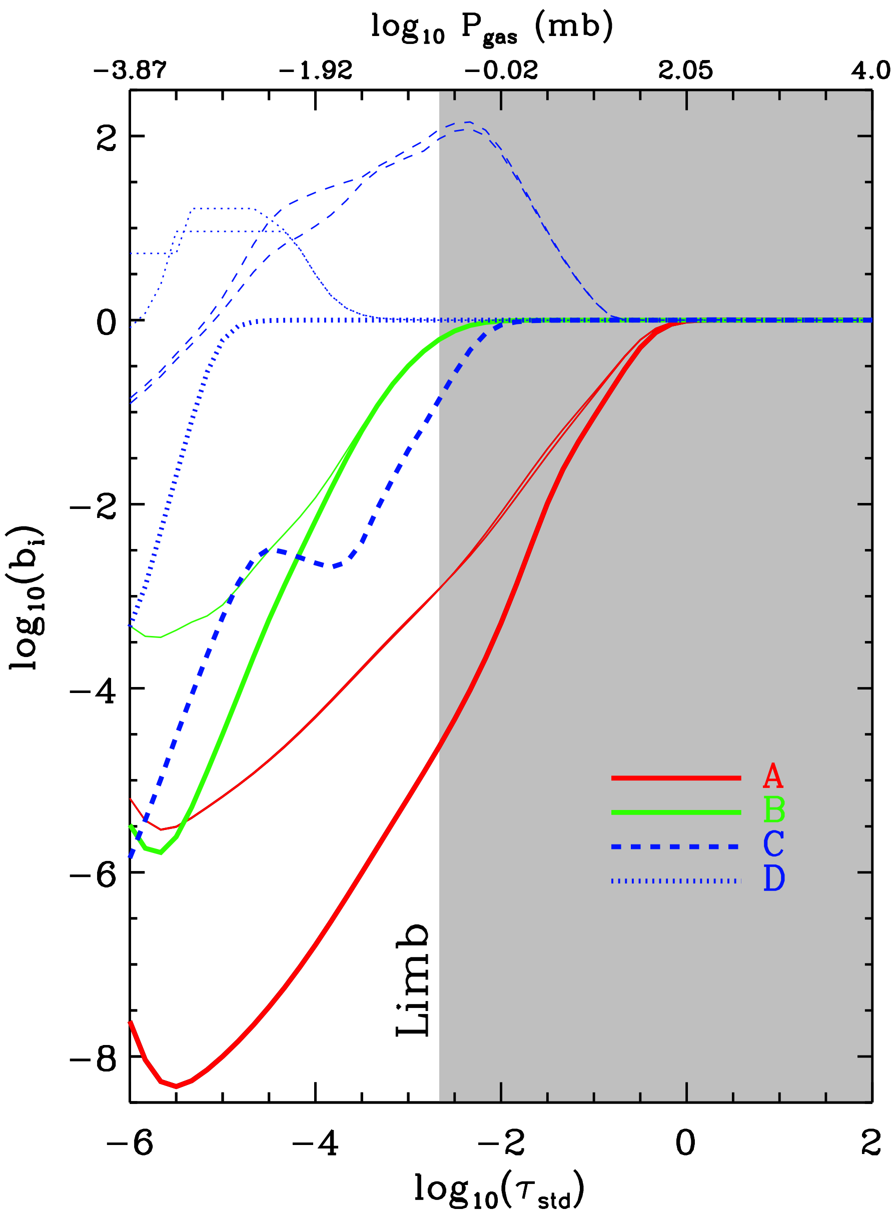

Figure 4.2: The departure coefficients for neutral sodium in the atmosphere of HD209458b as a function of the radial optical depth at 1.2μm($\tau_{\rm std}$) and pressure (top axis). Model A demonstrates departures for an irradiated atmosphere including only collisions with free electrons. Model B is the same as A, but includes collisions with H_2 assuming that H_2 has the same rate coefficients as an electron. Model C shows the departures in a non-irradiated atmosphere (where $T_{eq} = T_{\rm eff}$) with collisions treated as in Model A. Model D is the same as C but with collisions treated as in Model B. Thick lines refer to the 3s level (ground state) and thin lines indicate the 3p levels (for $J = 1/2$ and $J = 3/2$). The unshaded region is the portion of the atmosphere where stellar flux is transmitted (Limb) in the irradiated case.

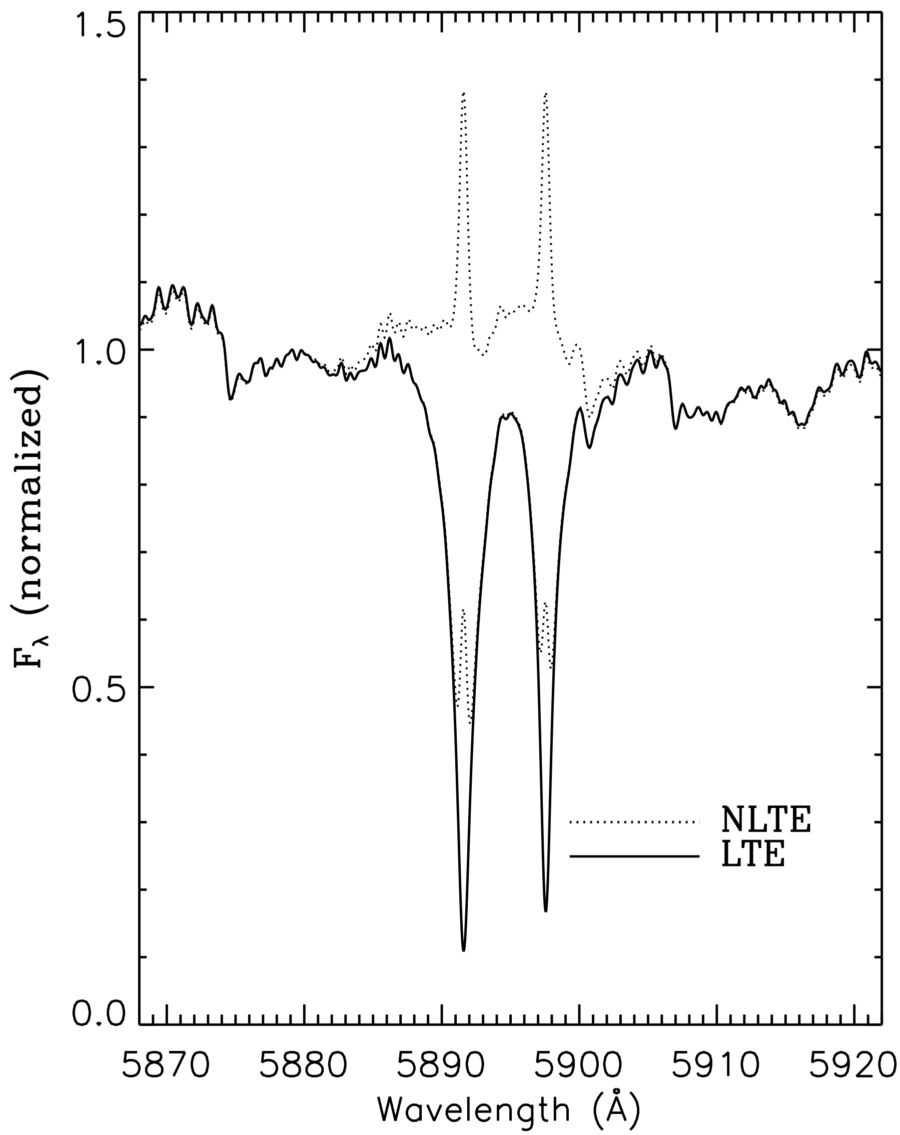

Figure 4.3: The Na D doublet for Model A (top dotted line), Model B (lowest dotted line), and when assuming LTE (solid line). The flux has been normalized to one at 5880Å.

shape while the line cores are reversed. The data analysis of Charbonneau et al. (2002) does not directly reveal the Na line profile produced by the planet atmosphere. Instead, their work shows that a deeper transit is observed in the Na band implying additional Na absorption by the planet limb. Given the current sensitivity of the observations, a core reversal feature like the one shown in our model B would be buried in the noise and manifest itself as simply a smaller equivalent width. The Na absorption in model B would result in a transit deeper than in the continuum bands but not as deep as implied by the LTE model. The fact that Na D absorption (and not emission) has been observed in the transmitted spectrum of HD209458b rules out our model A indicating that some thermalization does occur in the limb region. However, it is unlikely that the collisional rates are as large as those in our model B suggesting that the equivalent width of the Na D doublet will be substantially reduced by NLTE effects.

The reduced equivalent width predicted by our model is *not* due to photoionization of Na. In the majority of the limb, only 3% is ionized and the neutral Na concentration is nearly constant with $N_{\rm Na}/N_{\rm H2} \sim 10^{-5.5}$. Na is only significantly ionized ($\gg 5\%$) at the very top of the atmosphere where $P_{\rm gas} < 1\mu$bar. The shallow ionization depth of Na is due to the strong UV opacity provided by metals (e.g., atomic Mg, Al, Ca, Fe, and Ni) which effectively shield Na from the incident ionizing photons. The ionization predicted by our models (even 3%) is far greater than what is obtained from an LTE calculation but does not significantly affect the line profile. However, if the planet's atmosphere is substantially cooler than in our model, then additional condensation and settling could further deplete the atmosphere of metals and allow greater ionization of Na to occur. We also find that only a very small amount of Na is in molecular form and that neutral Na is nearly 3 orders of magnitude more abundant than NaCl (the most abundant Na bearing molecule). Furthermore, condensation of Na via NaCl grains is unlikely. The reduced equivalent width and central core emission is purely a radiative transfer effect.

4.4 Conclusions

The recent HST observations provided the first direct measurement of the conditions inside the atmosphere of HD209458b. However, even under the best circumstances, determining the concentration of any species based solely upon one absorption feature is problematic, especially if this feature forms in the upper regions of an atmosphere where pressures are low and NLTE effects are greatest. Our models clearly show that Na is far from being in LTE in the upper atmosphere of HD209458b and the observed Na absorption can be explained with a solar metallicity atmosphere which is cloud free or has only very low lying clouds. It is likely that other important species (e.g., CO and CH_4) are in NLTE, and we plan to test the LTE assumption for a wide variety of atomic and molecular species in a future work. Hopefully the Na D doublets and other alkali metal lines will be useful diagnostics in the study of EGP atmospheres. However, only with detailed NLTE calculations including well determined collisional rates will we have a chance at constraining the physical conditions in the atmosphere of HD209458b.

Chapter 5

Irradiated pre-CV secondaries

Post-common envelope binaries (PCEBs), already introduced in chapter 1, are composed of a hot WD (or sdOB) and a main sequence star, often a cool M dwarf (dM). Contrary to EGPs, PCEBs are easy to observe and many have a spectrum that clearly shows evidence of irradiation. The most frequently observed consequences of irradiation are emission lines (e.g., hydrogen Balmer lines) that are out of phase[1] with the radial velocity, are at maximum strength near superior conjunction (phase 0, illuminated face visible), and are at minimum strength near inferior conjunction (phase 0.5, non-illuminated face visible). Such a phase dependence is a clear indication that the emission, at least partially, originates from the illuminated surface of the secondary. The WD and M dwarf have roughly the same brightness in the optical to near-IR. Therefore, the Balmer emission lines from the secondary overlap with the normal absorption features of the WD leading to line profiles in the combined WD+dM spectrum that have reversed cores. In some cases, the emission from the secondary is strong enough so that no absorption wings remain, and the combined line profiles appear completely in emission. Table 5.1 lists a few examples of CV and pre-CV systems for which effects attributed to irradiation have been observed.

In addition to irradiation induced emission lines, CVs display H and He emission lines that are *not* related to irradiation and, depending on the type of CV, originate

[1]Phase is t modulo the period, where t is some time during the orbit of a binary. The period is the time for the secondary or primary to make one complete orbit. Phase 0 is usually chosen to coincide with superior conjunction (i.e. when the primary is between the observer and the secondary).

Table 5.1: Properties of CV and pre-CV systems

	White Dwarf			Red Dwarf								
Object	T_{eff}(K)	R($R_\odot$)	M($M_\odot$)	T_{eff}	R	M	type	P(hrs)	a($R_\odot$)	i	dist(pc)	refs.
GD 245	22,170	0.015	0.48	3560	0.27	0.22	M3-5	4.17	1.17	69	61	1
GD 448	19,000	0.0125	0.41		0.13	0.096	M5-6	2.47	0.74	29.3		2,3
PG 1224+309	29,300		0.40-0.45			0.28	M4-5	6.21	1.5	77	300	4
Z Cha	15,600	0.014	0.84	2700	0.17	0.13	M5	1.78	0.74	81	128	5
HT Cas	12,000		0.76			0.076	M5	1.90	0.73	80	120-224	6
QQ Vul	20,000		0.54		0.35	0.30	M4	3.7	1.14	65		7

References: (1) Schmidt et al. (1995); (2) Marsh & Duck (1996); (3) Maxted et al. (1998); (4) Orosz et al. (1999); (5) Wade & Horne (1988); (6) Marsh (1990); (7) Catalán et al. (1999).

from an accretion disk or near the WD surface. Unlike the emission lines from the secondary, emission lines from an accretion disk are double peaked and have a phase dependence that not only depends on the inclination[2] of the system, but also depends on the extension of the disk and where in the disk the lines form. Also, the additional emission lines in CVs are heavily broadened due to the large rotational velocities of the WD and accretion disk (which can exceed 100 km sec^{-1}) while lines originating from the secondary are often very narrow.

Despite these differences between the various types of CV emission lines, many overlap making it difficult to determine from which part of the CV they originated and what fraction of the line flux is from the WD, disk or M dwarf. Also, the emission from the WD or accretion disk is very bright and often completely overwhelms the emission lines produced by the illuminated hemisphere of the secondary. Therefore, probing the effects of irradiation on CV secondaries by measuring emission lines is difficult, if not impossible.

While CVs are excellent objects for studying accretion, pre-CVs are much better suited for observing the effects of irradiation. Since the WD in a pre-CV does not accrete material from the secondary, any observed emission lines will most likely originate from the secondary and will either be due to irradiation or chromospheric activity. If the emission line strength from a pre-CV varies with a phase dependence similar to the one described above, then some or all of the emission line comes from the illuminated face of the secondary. Chromospheric activity, on the other hand, exists on all sides of an M dwarf and should not vary with phase.

In the following sections, models of irradiated pre-CV secondaries are presented for a variety of orbital separations, secondary spectral types, and WD effective temperatures. The changes in the atmospheric structure, the chemical composition,

[2]Inclination (i) is the angle between the line-of-sight and the normal to the orbital plane.

and the spectrum are discussed. Also, a comparison is made between synthetic and observed spectra for a particular pre-CV, GD 245.

5.1 Modeling Irradiated pre-CV Secondaries

The physical conditions present in PCEBs are extremely different from those found in EGPs (compare tables 1.1, 1.2, and 5.1). Recall that the primary of an EGP (a solar type star) has a radius roughly 10 times larger than that of its secondary (the planet) whereas, in the case of a WD+dM pair, the situation is reversed! The hot WD primary has a radius roughly 10 times *smaller* than the cool dM secondary. Also, the orbital separations in CV and pre-CV systems are 10 times smaller (about twice the Earth-Moon distance) than the separations in the shortest period EGPs. Despite these differences, modeling the irradiated secondary in CV or pre-CV binaries is similar to modeling an irradiated planet. The only major difference concerning irradiation is the source(s) of extrinsic radiation.

In addition to the observational advantage mentioned above, focusing on pre-CVs rather than CVs has another benefit that is directly related to the modeling of irradiation. In most (non-magnetic) CVs, an appreciable amount of the total flux from the system comes from a hot accretion disk, a bright spot, and a boundary layer. Therefore, the disk adds additional sources of irradiation which make the total incident radiation field received by the M dwarf atmosphere strongly asymmetric about the line of centers. A total incident radiation field of this kind can no longer be approximated by a point source. Also, a sizable fraction ($\sim 20\%$) of the secondary will be shaded by the disk which surrounds the primary in a CV. These complications are difficult to model and are beyond the scope of this work, which will only consider irradiation in pre-CVs. Since the WD in a pre-CV does not accrete material from the secondary, no accretion disk or accretion streams will be present, leaving the WD as the only possible source of radiation incident on the surface of the secondary.

The most recent study of irradiation in PCEBs investigated the effects for M dwarfs ($3400 < T_{\rm eff} < 3800$K) located near a 10,000K blackbody (Brett & Smith, 1993). This work greatly improved our understanding of irradiation, but was limited by (1) using insufficient opacity sources, (2) using a blackbody for the external source, and (3) producing only very low resolution synthetic spectra. Consequently, these previous models were inadequate for direct comparison to any observed spectrum of a CV or pre-CV. The models presented below have been calculated without any of these limitations.

The incident flux from the WD primary is *not* assumed to be that of a black body but, instead, is taken from the grid of model atmospheres calculated by Barman et al. (2000). This grid was calculated for 1 solar mass WDs with $\log(g) = 8.0$ (cgs units) and for solar, 10^{-2}, and 10^{-4} solar metal abundances. These WD atmospheres were modeled as plane parallel slabs and include line-blanketing from the elements H through Ca, Kr through Nb, and Cs through La for a total of 40 neutral atomic species. A large number of these elements and their ions were allowed to depart from their LTE level populations. On average, the models include 5500 NLTE levels and 50,000 primary NLTE transitions, roughly half of what is currently available in PHOENIX. These models represent significant improvements over earlier works which were calculated in the LTE approximation. In general, the models have been successful at reproducing the observed spectra of many WDs (e.g., U Gem and VW Hydri).

The model calculations, for both the primary and the secondary, include more than 50,000 wavelength points between 10Å and 1000μm with a resolution of about 1Å from the UV to the near-IR. The opacity setup used to calculate the irradiated and non-irradiated model atmospheres for the M dwarf secondaries presented below is identical to that used in the NextGen model atmosphere grid of Hauschildt et al. (1999). With this setup, the atomic and molecular line opacity is treated with a "direct opacity sampling" (dOS) method which dynamically selects the important lines from a large master list at the beginning of each iteration. This line list includes, among many other species, TiO with more than 12 million lines from the strongest bands for the most important TiO and TiO isotopes (Jørgensen, 1994). The details of the dOS method and a complete list of the opacity sources included are described in Hauschildt et al. (1999).

5.2 Results

A variety of WDs and dMs at different orbital separations that sample parameters similar to the most commonly observed pre-CV systems have been modeled. The first system considered is a typical pre-CV consisting of a $1M_{\odot}$ 20,000K WD with $\log(g) = 8.0$ located near a $0.2M_{\odot}$ 3000K M dwarf with $\log(g) = 5.0$ (roughly equivalent to a dM5). Both the WD and M dwarf have been modeled as plane-parallel slabs. The majority of WDs have atmospheres containing mostly H and He and, unless they are accreting material from a metal rich companion (e.g., as occurs in CVs), have extermely low metal abundances. Because it is assumed that no metal enrichment via mass transfer has taken place in pre-CVs, only metal poor WD atmospheres have been selected from the grid of models published by Barman et al. (2000). Therefore, the WD atmospheres used in this study have a metal abundance 2 orders of magnitude below that of the M dwarf which is assumed to have a solar composition. Note that, for most isolated WDs, a 10^{-2} solar metal abundance is still very large compared to observations. However, the changes in the overall spectrum of a WD for metalicities below 10^{-2} times solar are too small to significantly change the irradiation effects in the M dwarf atmosphere.

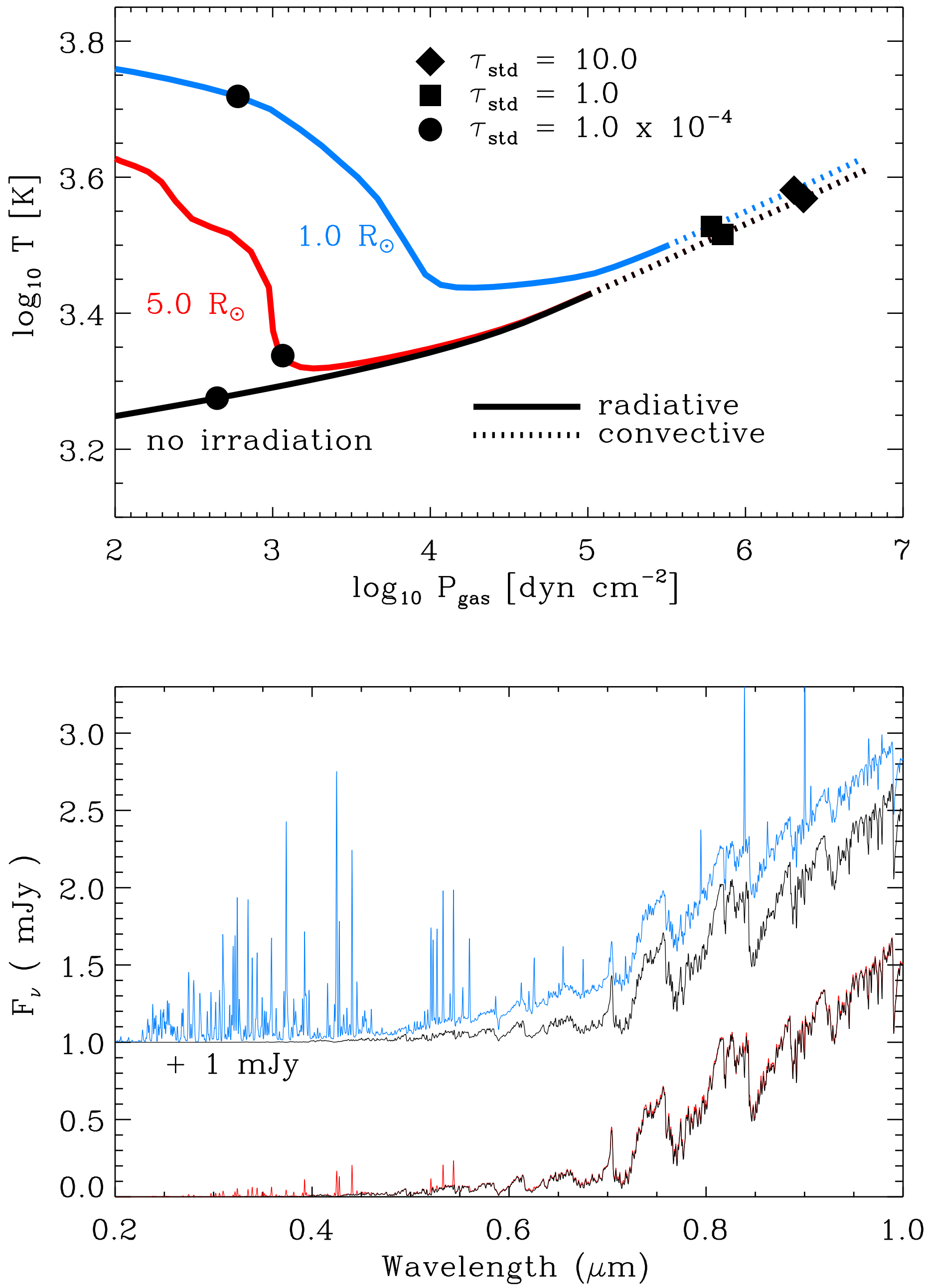

Figure 5.1: Top: the atmospheric structures and corresponding spectra for a (3000 K) M dwarf irradiated by a (20,000 K) WD at orbital separations of 5.0 and 1.0 $R_\odot$. Notice the inverted temperature profile in the irradiated models and the resulting emission lines in the spectra (Bottom). Note that the spectra for the M dwarf at 1 $R_\odot$ has been shifted up by 1 mJy.

The impact of the incident radiation on the M dwarf atmosphere is made most apparent by the changes to the temperature structure. In the top panel of figure 5.1, the non-irradiated M dwarf structure is compared to the structures of two irradiated models: one with an orbital separation of 5 $R_{\odot}$ and a second with an orbital separation of only 1 $R_{\odot}$. When the M dwarf is located 5 $R_{\odot}$ from the WD, little change occurs in the majority of the atmosphere except for a large temperature inversion in the very optically thin regions ($\tau_{\rm std} < 10^{-4}$) of the atmosphere. However, at 1 $R_{\odot}$, a significant temperature increase occurs throughout the atmosphere, even at large optical depths. Also, convection is slightly suppressed and the radiative-convective boundary is moved closer to $\tau_{\rm std} = 1.0$. The corresponding spectra are shown in the bottom half of figure 5.1. At 5 $R_{\odot}$, the M dwarf spectrum shows little change in the IR and only a few weak emission lines in the optical. However, at 1 $R_{\odot}$, the large temperature inversion has noticeable effects on the M dwarf spectrum. The irradiated M dwarf shows a dramatic increase in the infrared pseudo-continuum and a forest of narrow emission lines appear at ultraviolet through optical wavelengths.

The general shapes of the T-P profiles in figure 5.1 are qualitatively similar to those published by Brett & Smith (1993) (here after BS93). However, in the regions of low gas pressure, the temperatures predicted by the BS93 models are lower than those shown in figure 5.1 by more than a 1000K. At the bottom of the atmosphere ($P_{\rm gas} \approx 10^7$ dynes cm^{-2}), the temperatures predicted here are very similar to those in the BS93 models. These differences are likely due to the use of "straight mean" molecular opacities and a lack of any atomic opacity in the BS93 models. Note that, when the BS93 models were produced, reliable molecular line lists were only just becoming available and thus the use of SM opacities was quite common. However, large molecular line lists have been steadily produced over the past few years and have been incorporated into `PHOENIX`.

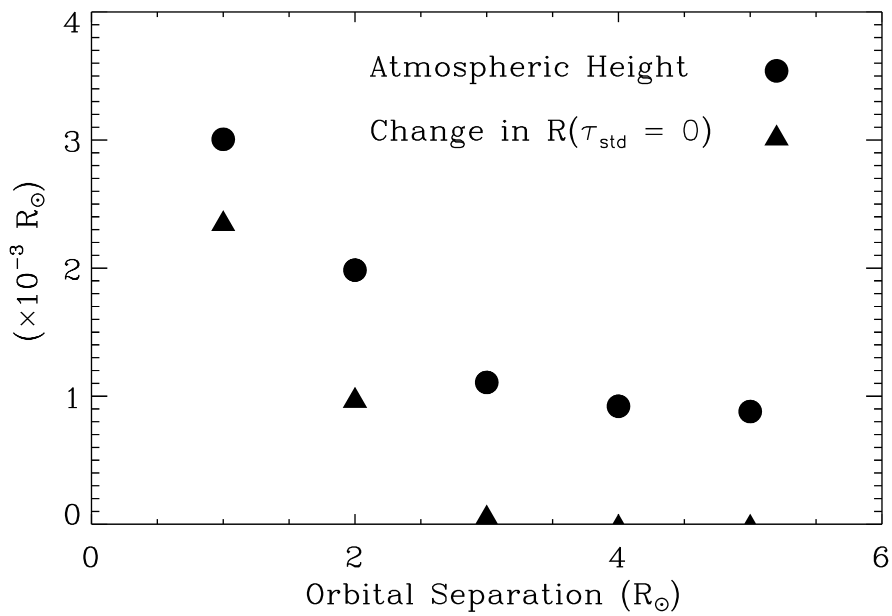

Figure 5.2: The atmospheric height for a 3000K M dwarf irradiated by a 20,000K WD at different orbital separations. The height of the atmosphere is defined as the difference between the radius at $\tau = 0$ and at $\tau = 100$.

As pointed out by BS93, the temperature rise at large depth (i.e. large $P_{\rm gas}$) is due to extrinsic radiation penetrating down to and being absorbed at the top of the convection zone. In a purely adiabatic convection zone, the energy transport is determined by the adiabatic temperature gradient, $\left(\frac{d\ln T}{d\ln P}\right)_{\rm add}$. Since the atmosphere is assumed to be in thermal equilibrium, each layer in the convection zone must transport a constant total energy ($\propto T^4_{\rm int}$). Thus, a temperature increase at the top of the convection zone must lead to a similar increase in temperature at all other layers in the convection zone so that $\left(\frac{d\ln T}{d\ln P}\right) = \left(\frac{d\ln T}{d\ln P}\right)_{\rm add}$ (assuming that the temperature changes are small enough so that $\left(\frac{d\ln T}{d\ln P}\right)_{\rm add}$ remains the same). Qualitatively, this can be thought of as the absorbed incident energy being "convected" down to deeper layers. As can be seen in figure 5.1, the presence of convection in an irradiated atmosphere can lead to a very different adiabat (and, consequently, a very different entropy in the core) from that of the non-irradiated star. Since the entropy of stellar or substellar object is strongly correlated to its age and it is likely that the material below the photosphere is well mixed, the irradiated and non-irradiated model atmospheres must have the same entropy at depth if they are to represent the same object (Vaz & Nordlund, 1985; Brett & Smith, 1993). Entropy matching can be achieved by reducing $T_{\rm int}$ of the irradiated model. The amount that $T_{\rm int}$ is reduced is a measure of the energy that is horizontally redistributed in the photosphere (Vaz & Nordlund, 1985; Brett & Smith, 1993). For the models in the following sections, the entropy matching constraint has been applied.

The changes to the structure due to irradiation also affects the height (or extension) of the atmosphere. Without any hard boundaries for the atmosphere, the *extension* is usually defined as the difference between the radius at two reference optical depths; $H = R(\tau_{\rm std} = 0) - R(\tau_{\rm std} = 100)$. In figure 5.2, the variation of the atmospheric extension for a 3000K M dwarf with $\log(g) = 4.5$ is shown for various distances from a 20,000K WD. The extension nearly triples as the M dwarf is moved in from $5R_\odot$ to $1R_\odot$. About one half of the increase in H is due to an increase in the total radius of the star, $R(\tau_{\rm std} = 0)$.

5.2.1 The Incident Flux

In general, $f \equiv F_{\rm inc}/F_{\rm int}$ is a good measure of the overall importance of irradiation. However, as mentioned previously, the effective temperature of a WD ($T_{\rm wd}$) in a pre-CV can range from $\sim 10,000$K to higher than $100,000$K. Thus, two binaries may have very different values of $T_{\rm wd}$, but their orbital separations and radii are such that f is nearly the same for both. In such a situation, the total (λ integrated) incident flux will be comparable but the wavelength at which the incident flux is a maximum will be very different for the two secondaries. In order to test the importance of the energy distribution of the extrinsic flux, two pre-CVs have been modeled; one with

$T_{wd} = 50,000$K and the other with $T_{wd} = 10,000$K (R_{wd} is kept the same). In both cases, the secondary has $T_{int} = 3400$K, $\log(g) = 5.0$, and the orbital separations are such that $f = 0.1$. The incident fluxes for both binaries are compared in figure 5.3. The incident flux from the two WDs peak at different wavelengths and have very different energy distributions compared to each other and to that of a black body with the same temperature. The majority of the incident flux from the 50,000K WD occurs at wavelengths shorter than 1500Å and, compared to the 10,000K WD, produces very little incident optical to near-IR flux. The incident flux from the 10,000K WD peaks at 2000Å and there is a significant amount of incident optical flux but very little extreme UV incident flux. The resulting structures for the irradiated secondary in each case are also shown in figure 5.3 (inset). Since the flux from the hotter WD peaks in the EUV, the incident radiation is primarily absorbed in the upper layers, where most of the free metals (i.e. not in molecular form) are found. The result is a much steeper temperature inversion than found in the secondary irradiated by the cooler WD, which produces fewer photons at short wavelengths. The incident flux from the cooler WD, which is 25 times closer to the secondary than the hotter WD, provides much more flux at wavelengths greater that 5000Å, where molecular opacity dominates. Molecules like H_2, H_2O, and CO are the dominant species for $P_{gas} \geq 10^4$ dynes cm^{-2}. Consequently, the secondary irradiated by the 10,000K WD absorbs more extrinsic energy at larger optical depths, producing a much hotter temperature minimum than found in the secondary irradiated by the 50,000K WD. Note that the two temperature-pressure profiles intersect at roughly $P_{gas} = 10^4$ dynes cm^{-2}.

The structures of the M dwarf were also modeled using incident flux from blackbodies for both T_{wd} values. In figure 5.3, the blackbody spectra are shown to underestimate the amount of incident EUV flux and, consequently, the changes in the temperature structure of the upper atmosphere are also underestimated. For

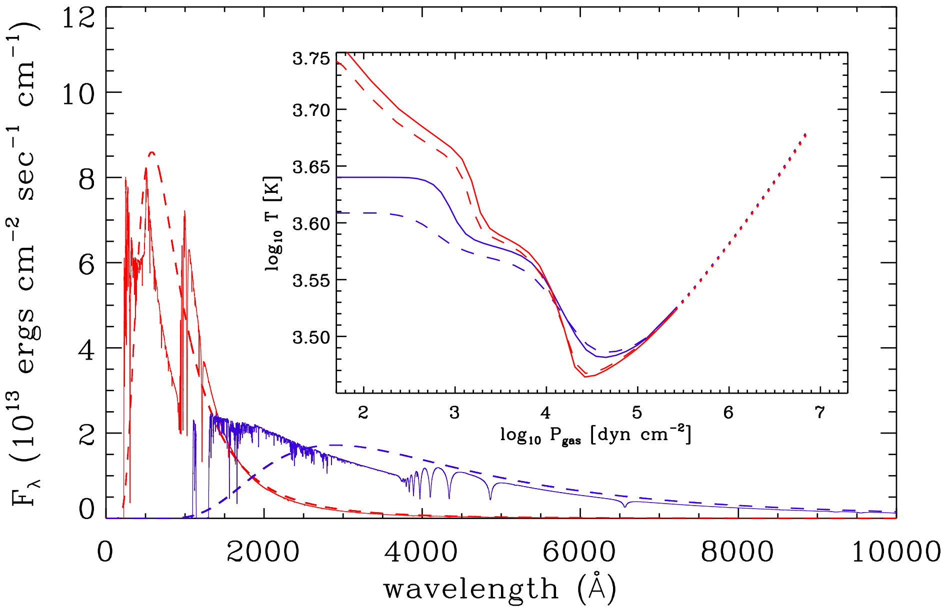

Figure 5.3: The spectra for a 50,000K (red) and a 10,000K (blue) WD both with $R = 0.015\mathrm{R}_\odot$, $\log(g) = 8.0$ and solar compositions. Dashed lines are blackbody flux distributions. Each flux distribution has been scaled by $(\frac{R_{wd}}{d})^2$, where $d = 10\mathrm{R}_\odot$ for the 50,000K spectra, $d = 0.4\mathrm{R}_\odot$ for the 10,000K spectra, and R_{wd} is the same for both, $0.015\mathrm{R}_\odot$. The inset shows the structures for a 3400K ($\log(g) = 5.0$) M dwarf atmosphere irradiated by each of the four flux distributions (dashed lines are for blackbody incident flux).

$\mathrm{T_{wd}} = 10,000\mathrm{K}$, the model irradiated by a blackbody is nearly 200K cooler than the model irradiated by the more realistic synthetic spectrum. Furthermore, in closely separated pre-CVs, one observes the combined flux from the WD and M dwarf and, therefore, it will always be necessary to included a realistic spectrum of the WD (especially in the optical) when modeling the total flux from a pre-CV.

5.2.2 Effects on Chemical Constituents

For M dwarfs with spectral types later than M3, the optical pseudo-continuum is almost completely determined by the TiO bands and many of the atomic features present at early spectral types are buried inside these molecular bands (e.g., the K I doublet at 7700Å and Ca II triplet near 8600Å). The Na doublet at 8200Å is the most prominent atomic feature in the near-IR that can be directly attributed to the secondary. Consequently, this doublet is often used to obtain orbital velocities for the secondary and to probe the conditions in the M dwarf photosphere.

In figure 5.4, the concentration of neutral sodium in the non-irradiated model is compared to the concentration in the irradiated model shown above in figure 5.1 (at 1 $R_\odot$ orbital separation). A significant reduction of neutral Na throughout the atmosphere is evident and roughly proportional to the temperature rise seen in figure 5.1. The decrease in the concentration of Na I and the presence of a temperature inversion produce a very different Na doublet feature (at 8200Å) compared to the spectrum of the non-irradiated model (see Fig. 5.4 inlay). The most noticeable effects on the doublet are the core emission lines which are due to the temperature inversion. The changes in the line wings of the doublet are primarily due to the reduced concentration of Na at large depths. The effects are similar for K (shown in the bottom half of fig. 5.4). However, in this case, an additional increase occurs in the pseudo-continuum flux around 7680Å due to a decrease in the TiO absorption that dominates the spectrum at these wavelengths.

The TiO bands, which are very sensitive to changes in $T_{\rm eff}$, play an important role in determining the spectral type of the secondary. In figure 5.5, the concentrations of the most abundant Ti bearing species (atomic and molecular) are shown for both the irradiated (at $1R_\odot$) and non-irradiated 3000K M dwarf models. In the non-irradiated M dwarf atmosphere, TiO and TiO_2 are the most abundant sources of Ti for $\tau_{\rm std} < 1.0$ while neutral atomic Ti I becomes more prevalent at $\tau_{\rm std} > 1.0$. In the irradiated atmosphere, there is a decrease in TiO for $\tau_{\rm std} < 1.0$ and a sharp decrease in *all* Ti bearing molecules for $\tau_{\rm std} < 10^{-2.5}$. As the Ti bearing molecules are dissociated in the upper layers, they are replaced by increased concentration

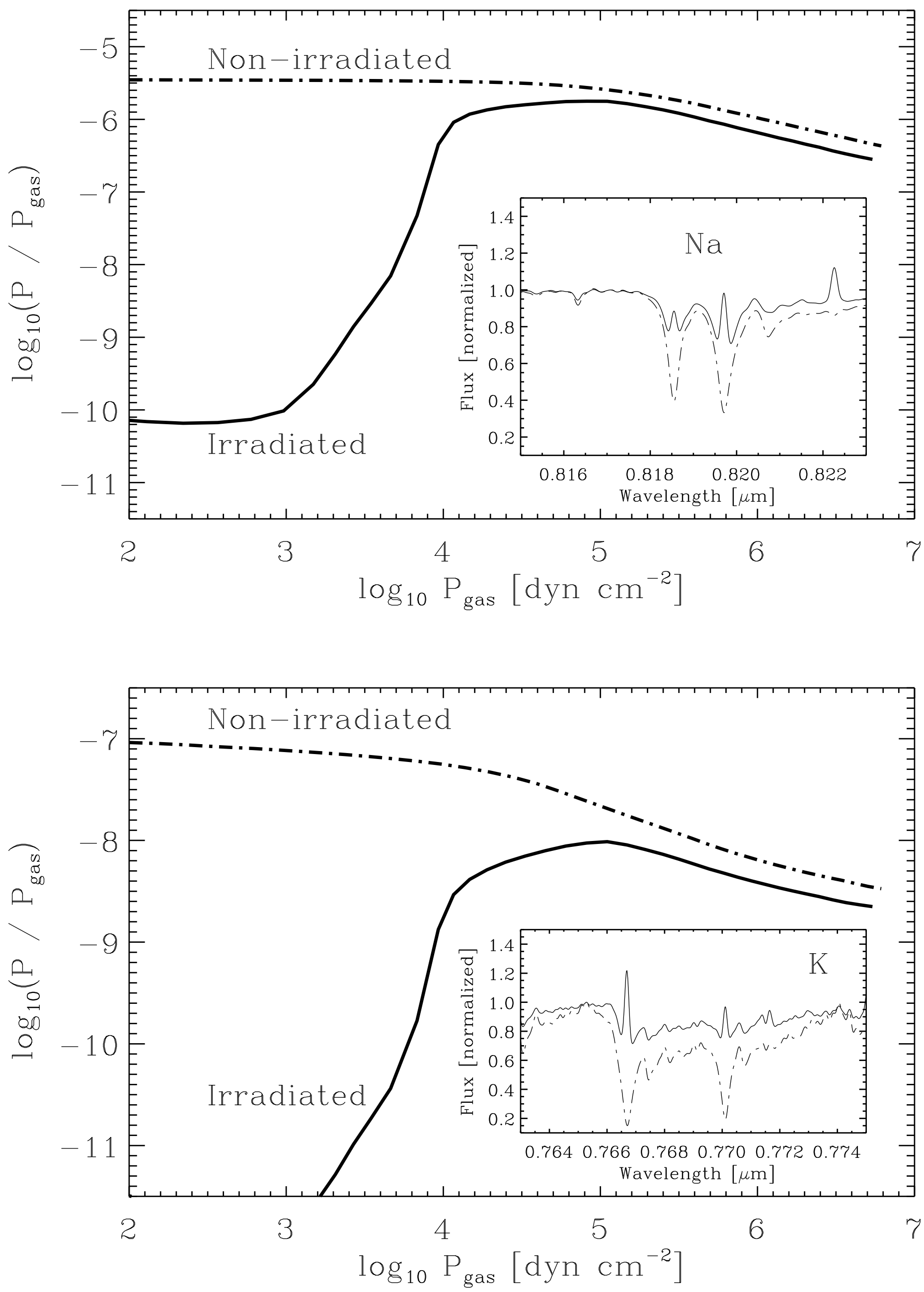

Figure 5.4: Top: Concentration of Na I in an irradiated (solid line) M dwarf with an orbital separation of 1 $R_\odot$ and non-irradiated (dash-dotted line) model (see text for details). Also shown, the change in a Na I doublet due to irradiation. Bottom: same, but for K I.

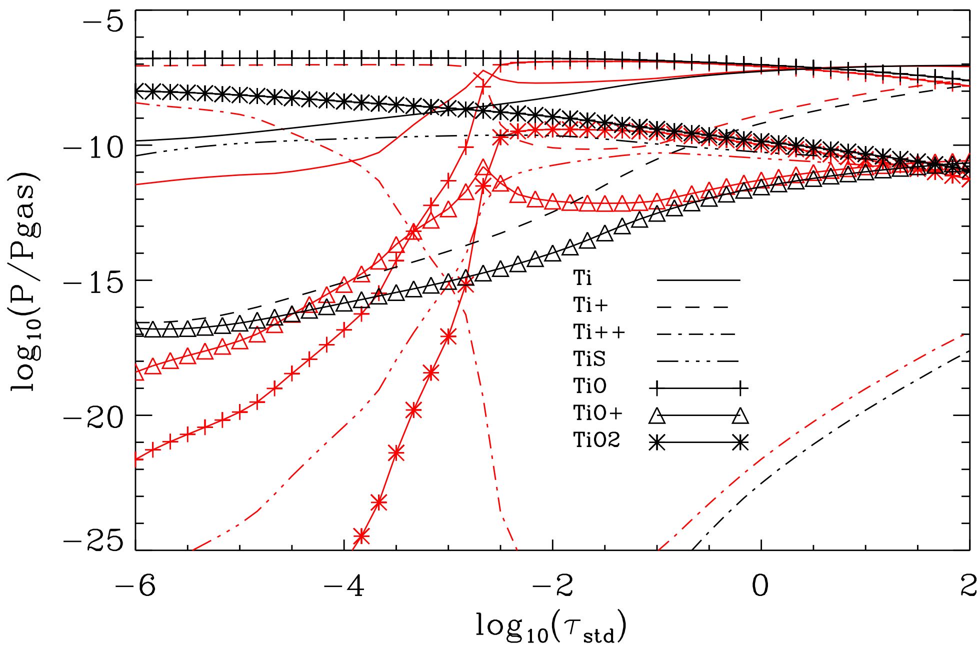

Figure 5.5: Concentrations of the 7 most important Ti bearing species in an irradiated (red) and non-irradiated (black) M dwarf model. $\tau_{\rm std}$ is the optical depth at 1.2μm.

of Ti II. In figure 5.6, the TiO concentrations and the TiO band between 8400Å and 8700Å are compared between the same irradiated and non-irradiated models. Notice that the Ca II triplet is strongly in emission amongst a collection of weaker Fe emission lines. In non-magnetic CVs, the Ca II triplet is usually dominated by double-peaked Ca II emission lines from the accretion disk. However, in pre-CVs, single peaked emission lines that originate from the illuminated hemisphere of the secondary are often observed (e.g., GD 448 and GD 245).

5.2.3 Determining Spectral Types

Since the TiO bands are altered by irradiation effects and the presence of the WD continuum, individual bands cannot be used to determine the spectral type of the

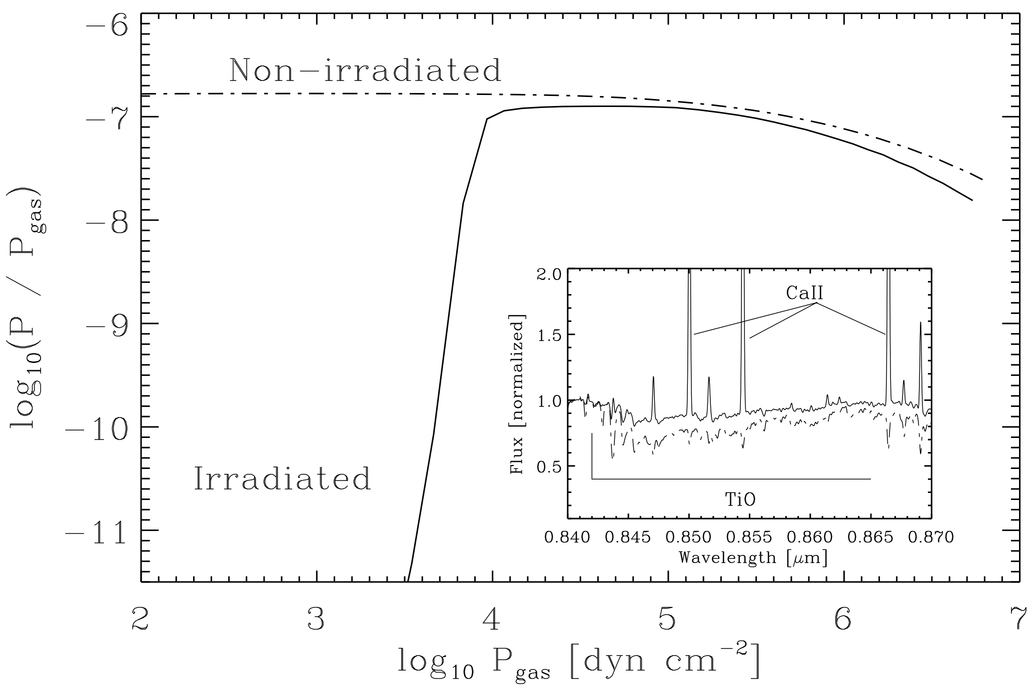

Figure 5.6: Similar to figure 5.4, but for the concentration of TiO. The inset demonstrates the difference between the spectra, centered on a TiO band, for an irradiated (solid line) and non-irradiated (dotted line) model. The three prominent emission lines are due to Ca II.

secondary. However, the ratio of the TiO band strengths at 7150Å and 7700Å has been demonstrated to be a good indicator of spectral type, which should not be affected by the WD continuum or irradiation because both bands are equally affected (Young & Schneider, 1981). This method has been used for several WD+dM pairs (e.g., Z Cha and HT Cas) and is generally assumed to be accurate to within 1 spectral type.

To test the accuracy of this method, a sequence of irradiated and non-irradiated models have been constructed spanning spectral subtypes M3.5 through M6.5. Each irradiated model includes incident flux from a 14,000K WD at an orbital separation of 1 $R_{\odot}$. In the top of figure 5.7, the irradiated and non-irradiated structures are compared. Above $\tau_{\rm std} = 10^{-4}$, all irradiated structures reach about the same temperature plateau, which approximately corresponds to the effective temperature of the incident flux (at the surface of the secondary) plus the intrinsic effective temperature of the M dwarf. The temperature minimum for each model increases and moves to slightly lower gas pressures as $\mathrm{T_{eff}}$ increases. The fact that a small portion of the incident flux reaches layers very near the radiative-convective boundary leads to a slight increase in the temperature at all depths in the convection zone. Therefore, to ensure that the irradiated and non-irradiated models for each spectral type represent the same star, $\mathrm{T_{int}}$ was reduced by $\sim$ 50K in the irradiated models to allow for entropy matching. The spectra for the irradiated models are also shown in the bottom of figure 5.7.

In all CV and pre-CV systems the flux from the primary and secondary (and disk, if present) cannot be separated, and only the combined flux is observed. Therefore, in order to approximate the real situation encountered by observers, the synthetic spectra of the WD, irradiated M dwarf, and non-irradiated M dwarf are combined to produce an orbit-averaged synthetic spectrum for each spectral type assuming an inclination of 90°.

Following the procedure outlined by Wade & Horne (1988) (a modified version of the procedure by Young & Schneider, 1981), two average flux deficits relative to a reference continuum have been calculated for the TiO bands at 7165Å and 7667Å (indicated in Fig. 5.7). For each band, the reference continuum, c_λ, is chosen to be a straight line best fitting the regions adjacent to the molecular bands. Using this reference continuum, the flux deficits were determined by the following equations:

$$\mathrm{TiO}(7165) = \frac{\int_{7140}^{7190} [c_\lambda - f_\lambda]\, d\lambda}{\int_{7140}^{7190} d\lambda} \qquad \mathrm{TiO}(7665) = \frac{\int_{7640}^{7690} [c_\lambda - f_\lambda]\, d\lambda}{\int_{7640}^{7690} d\lambda} \tag{5.1}$$

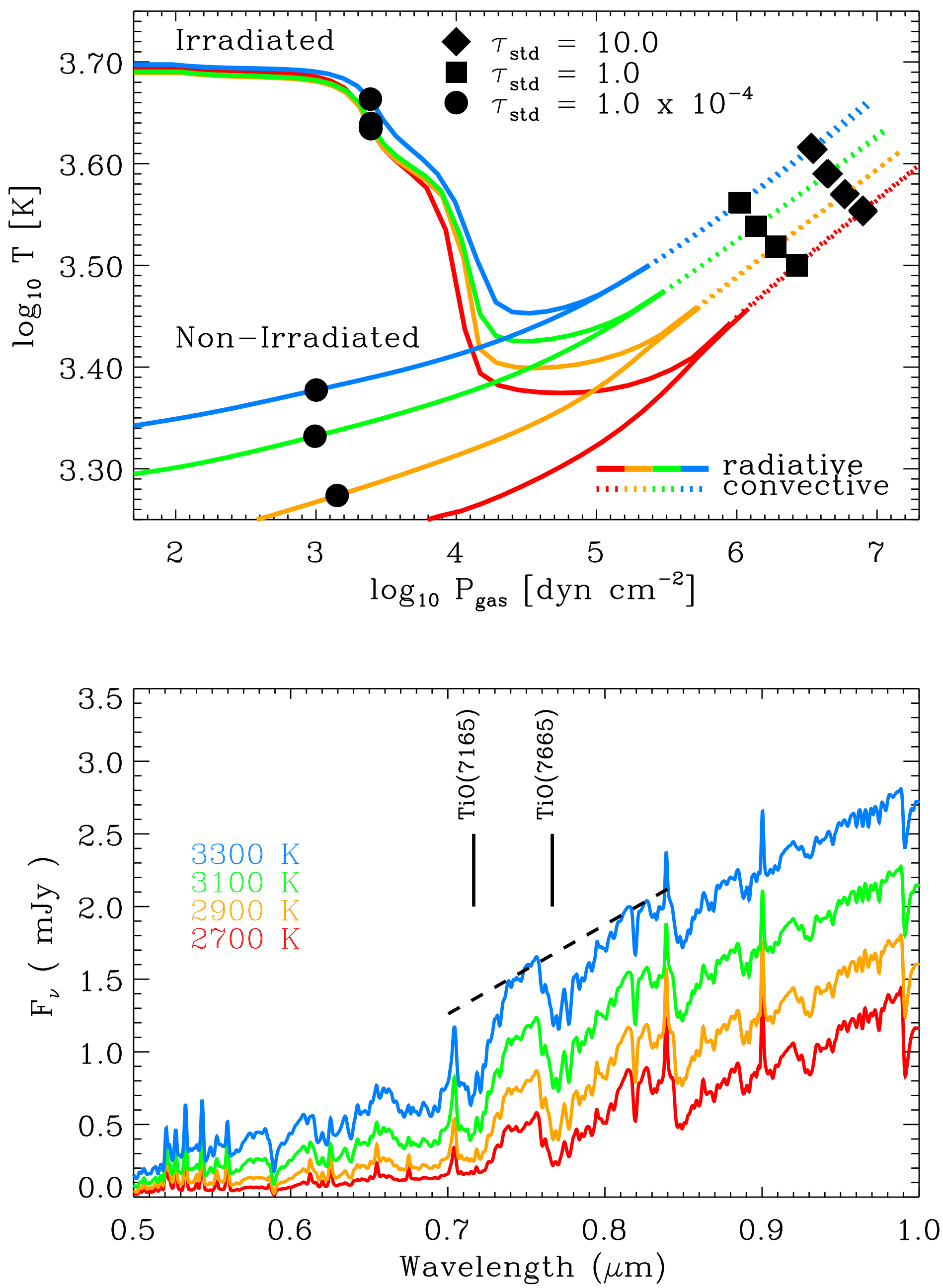

Figure 5.7: Top: non-irradiated and irradiated atmospheric structures are shown for M dwarfs with different effective temperatures (or spectral types). In each case, the same 14,000 K WD was placed 1 $R_\odot$ from the M dwarf. Bottom: the spectra corresponding to the irradiated models. The dashed line is a typical reference continuum used to measure the strength of the TiO bands (labeled) for the 3300K model.

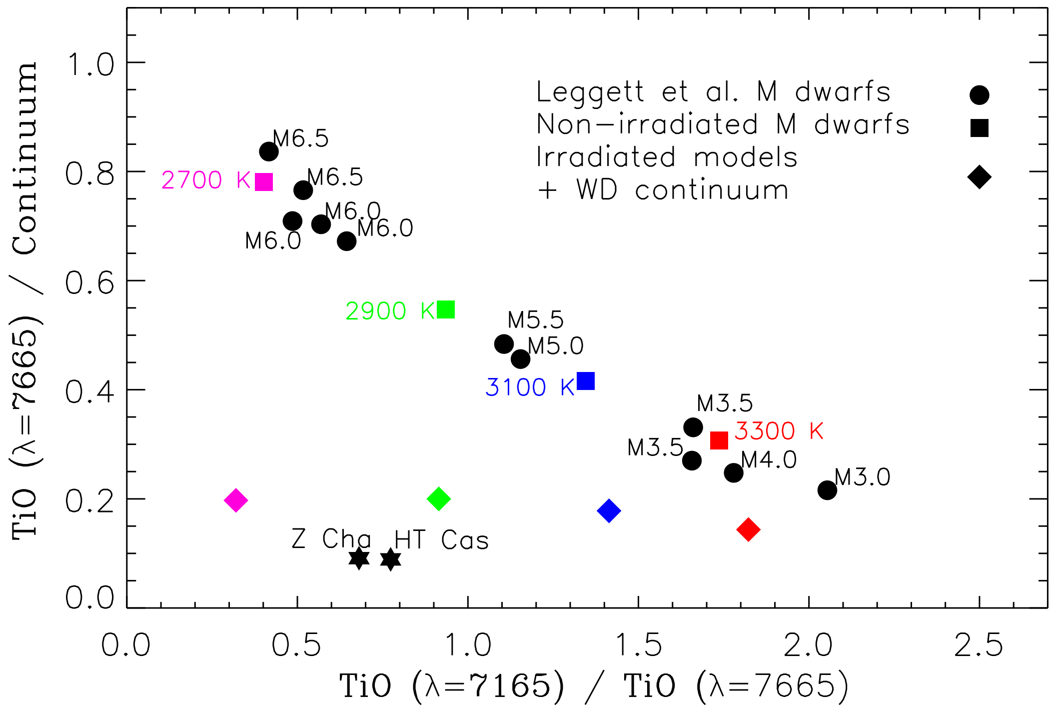

Figure 5.8: The strengths of two TiO bands for non-irradiated and irradiated models are compared to the TiO band strengths of isolated M dwarfs from the Leggett et al. (2000) survey (see text for details). Observed values for two CV secondaries, HT Cas and Z Cha, are indicated by star symbols. Each color indicates a particular T_{eff} value for the models.

The dashed line in figure 5.7 is a typical reference continuum for the TiO(7665) and M3.5 spectral type.

The TiO(7665) index relative to the continuum flux at 7665Å and the ratio TiO(7165)/TiO(7665) for the non-irradiated M dwarf models and several observed isolated M dwarfs from the Leggett et al. (2000) survey are shown in figure 5.8. Both the non-irradiated models and the real objects form a well-defined sequence of spectral types. The TiO indices for the orbit-averaged spectra from the sequence irradiated by a 14,000K WD (diamonds) are also shown in figure 5.8. Each of the irradiated models have nearly the same ordinate values (~ 0.2) due to the fact that the continuum at 7665Å is mostly determined by the WD flux, which was kept the same for each spectral type. However, the abscissa values remain roughly unchanged indicating that TiO(7165)/TiO(7665) remains a good indicator of spectral type. Observations for Z Cha (Wade & Horne, 1988) and HT Cas (Marsh, 1990) are also shown in figure 5.8 (stars). For these two objects, the spectral type was chosen to be that of an isolated M dwarf with the same TiO band ratio. The models presented here support the use of this technique, but they indicate that an error of about 0.5 in spectral subtype may result for the earliest and latest M dwarfs.

5.3 GD 245

GD 245 is a bright WD in the constellation Pegasus which was first shown to have a companion by Tytler & Rubenstein (1989). The presence of a companion was further supported by the observations of Schultz et al. (1993). The secondary was later classified as roughly a dM4 spectral type by Schmidt et al. (1995) using phase-resolved spectroscopy covering 0.35 to 1.0 microns. In the following sections, a model based on the system parameters (table 5.2) published by Schmidt et al. (1995) is compared to echelle spectra (also from Schmidt et al., 1995).

Schmidt et al. (1995) estimated that the secondary in GD 245 under fills its roche lobe by less than 25% and, therefore, does not have the characteristic tear-drop shape of roche lobe filling secondaries in CVs. Therefore, the secondary is assumed to be spherical and the non-uniformities over the surface are assumed to be due to irradiation. If a standard spherical coordinate system is adopted, with the origin located at the center of the secondary and positive z-axis intersecting the center of the primary, then lines of constant latitude (measured from the z-axis) receive the same amount of incident flux from the WD. Points near the terminator (which lies in the z=0 plane) receive less incident flux than the substellar point because of

Table 5.2: System parameters for GD 245

	Primary	Secondary
K (km s^{-1})	100 ± 6	216 ± 4
$\log(g)$	7.77 ± 0.02	
Mass ($M_\odot$)	0.48 ± 0.02	0.22 ± 0.02
Radius ($R_\odot$)	0.0150 ± 0.0005	0.27 ± 0.02
$T_{\rm eff}$ (K)	22170 ± 130	3560
Spectral Type	DA2	M3-5
Period	4.1679 ± 0.0003 hr	
Semimajor axis	1.17 ± 0.01 $R_\odot$	
Distance	61 ± 2 pc	
Inclination	$69^{\circ}{}^{+8}_{-7}$	

K is the radial velocity amplitude and g is the surface gravity in cgs units. The remaining quantities are either self-explanatory or defined in the text. All values are from Schmidt et al. (1995).

shallower incident angles and larger distances from the WD. Consequently, a single model atmosphere cannot be used to represent the entire irradiated face.

Following the suggestion made by Brett & Smith (1993), a grid of irradiated model atmospheres has been constructed with each model representing a specific latitude. Each model in the grid was calculated by solving the SSRTE. As mentioned in chapters 3 and 4 for EGPs, the PPRTE does not accurately treat radiation incident onto or emerging from regions near the limb. The SSRTE, however, ensures that the correct lower boundary conditions are met. Another major difference between the models in the grid and those presented above (Fig. 5.1), is that the incident radiation is *not* isotropic – extrinsic flux is only allowed to enter the atmosphere along a specific angle, θ (which roughly corresponds to the latitude being modeled). The temperature-pressure profiles corresponding to each latitude are shown in figure 5.9; the latitudes sampled by the grid are also shown, schematically, in figure 5.9.

The region near the substellar point shows a significant temperature inversion. As is expected, the strength of the temperature inversion decreases as θ approaches

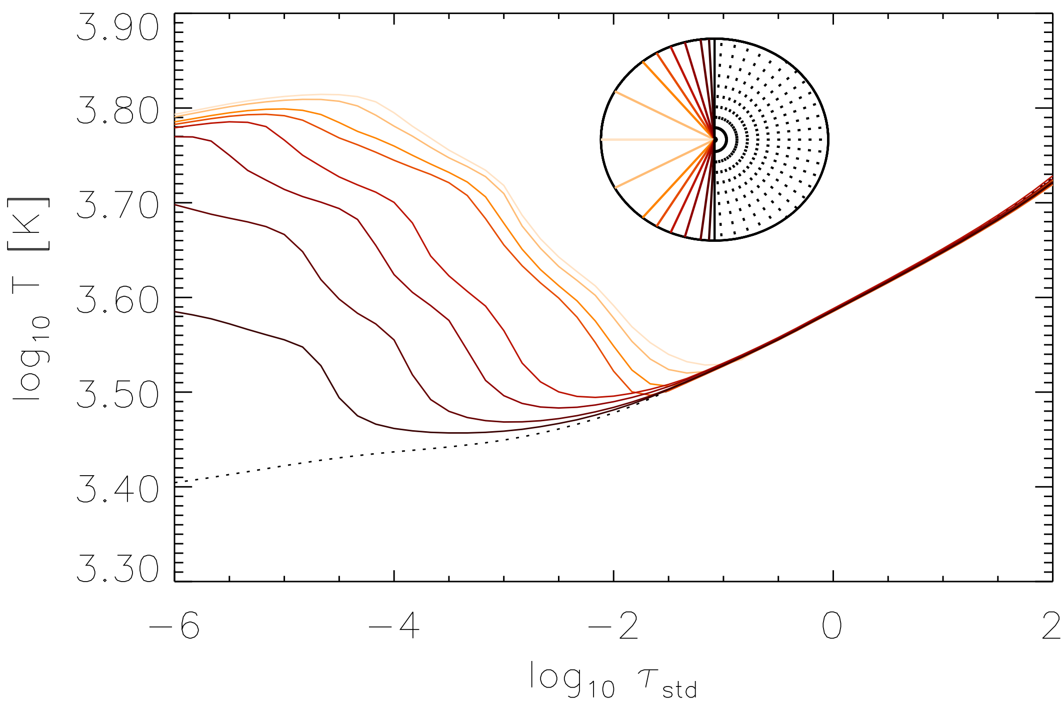

Figure 5.9: The structures used to construct the irradiated (solid lines) and non-irradiated (dotted line) hemispheres of GD 245 (parameters taken from table 5.2). The corresponding latitudes are, from top to bottom, $0°, 28°, 51°, 59°, 67°, 75°, 83°, 87°$. A single non-irradiated structure (dotted line) was used for all latitudes on the nightside hemisphere. The regions sampled by this sequence of models is shown, schematically, in the upper right-hand corner.

the terminator ($\theta = 90°$). For the reasons mentioned above, the entropy matching constraint was applied to the irradiated models. Only the models closest to the substellar point required changes to T_{int}. At the substellar point $\Delta T_{int} \sim 100$K; at $\theta = 28°$, $\Delta T_{int} \sim 50$K; and, for $\theta \geq 30°$, $\Delta T_{int} < 5$K. The structures in figure 5.9 also indicate that a steep horizontal temperature gradient will exist in the optically thin upper layers of the atmosphere of GD 245 and may lead to meridional circulations. Unfortunately, our 1-D models cannot address this issue in detail.

The monochromatic luminosity of the illuminated side of GD 245, based on the irradiated models shown in figure 5.9, is

$$L_{\mathrm{day},\lambda} = \sum_{i=1}^{N} F(\theta_i)_\lambda \delta A_i \quad \text{where} \quad \sum_{i=1}^{N} \delta A_i = 2\pi R_s^2. \tag{5.2}$$

In the equation above, R_s is the radius of the secondary and $F(\theta_i)_\lambda$ is the monochromatic flux from the irradiated model which corresponds to latitude θ_i and annular surface area δA_i. The luminosity of the unilluminated side is $2\pi R_s^2 F_0$, where F_0 is the flux from the non-irradiated model (dotted line in figure 5.9). At a particular phase (ϕ) and inclination (i), only a fraction (Ω) of the day side will be visible. Therefore, the flux from the secondary measured by an observer at distance d is,

$$F(\phi, i)_{\mathrm{2nd},\lambda} = \frac{1}{2\pi d^2} \left\{ \Omega(\phi, i) L_{\mathrm{day},\lambda} + \left[1 - \Omega(\phi, i)\right] L_{\mathrm{night},\lambda} \right\} \tag{5.3}$$

with

$$\Omega(\phi, i) = \frac{1}{2} \left[1 - \cos(\phi) \sin(i)\right]. \tag{5.4}$$

Before being compared to observations for at particular phase, $F_{\mathrm{2nd},\lambda}$ must be rotational broadened and Doppler shifted based on the velocities and radii given in table 5.2. To model the *combined* monochromatic flux from the binary system , the rotationally broadened flux from the WD (see parameters in table 5.2) must also be added to $F_{\mathrm{2nd},\lambda}$. The final flux that may be compared directly to the observations of GD 245 is,

$$F(\phi, i)_\lambda = \frac{1}{2\pi d^2} \left\{ \Omega(\phi, i) L_{\mathrm{day},\lambda} + \left[1 - \Omega(\phi, i)\right] L_{\mathrm{night},\lambda} + 2\pi R_p^2 F_{\mathrm{WD},\lambda} \right\}. \tag{5.5}$$

The combined flux from the WD+dM pair for GD 245 is shown in figure 5.10. The spectrum of the WD shows the characteristic hydrogen absorption lines and becomes nearly featureless in the IR. The total observed flux from the system is dominated by the continuum of the WD in the optical with only the very strong emission lines from the M dwarf present. Toward the near-IR and IR, the slope of the continuum

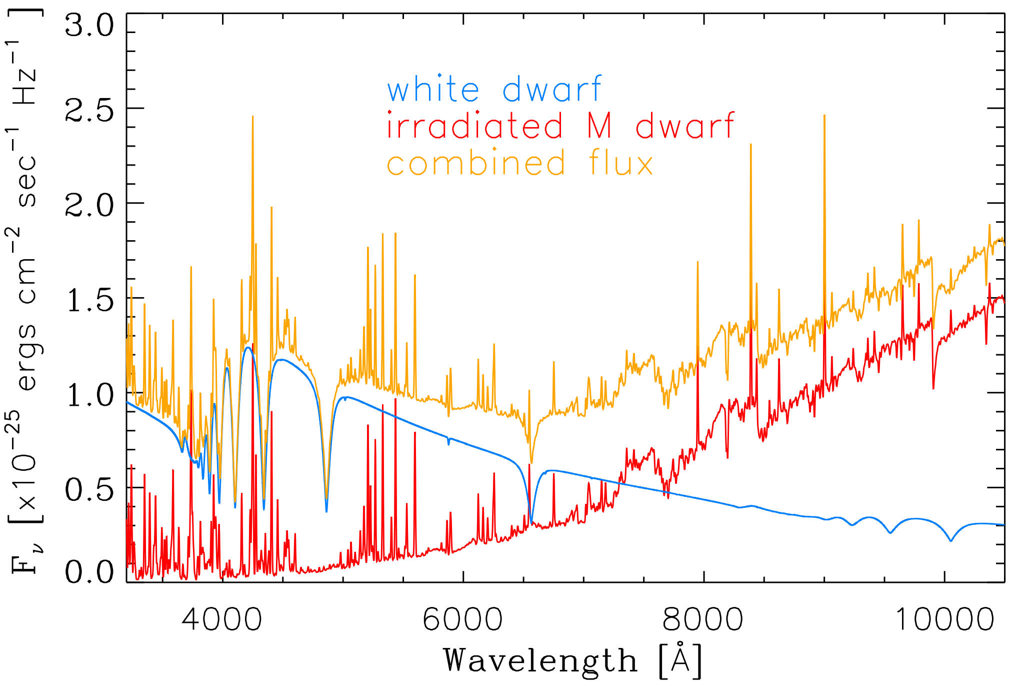

Figure 5.10: The synthetic spectra for a WD (22,000K) and irradiated M dwarf (3,500K) similar to those observed in GD 245. The combined WD+dM flux is also shown at phase 0 and 90° inclination.

changes sign as the M dwarf begins to dominate the total flux. For wavelengths longer than 7000Å, all of the spectral features are due to the M dwarf and the only contribution from the WD is to the continuum. Note that in figure 5.10, a phase of 0.0 (superior conjunction) and an inclination of 90 degrees have been assumed. The strength of the emission lines near inferior conjunction vary with the sine of the inclination and are often used to set a lower limit on the inclination.

Figure 5.11 shows the comparisons for H_α and H_β between the observed and synthetic spectra of GD 245 at phase 0.9 and inclination i = 62°. Note that the observed spectra could not be precisely flux calibrated and, therefore, the absolute flux in the continuum represents the observers "best estimate" (see Schmidt et al. (1995) for details). Given the approximations mentioned above, the fit is extremely good. The height of the H_α emission line and the continuum are well represented in the model. However, the FWHM is larger in the observations. In the case of H_β (bottom half of fig. 5.11), the model overestimates the strength of the emission line but reproduces the line wings very well. Note that the small emission "bumps" on the red wing are actually weaker emission lines from the irradiated hemisphere due to metals (Fe, Ni, etc.). The overall shape of the H_β line wings are fairly sensitive to the irradiation and the fraction of the dayside that is observable.

The discrepancies between the model and observation could be due to several factors. One important source of error is the averaging used to produce the flux from the secondary. A more realistic approach would be to integrate over only those *intensities* that would emerge from the secondary parallel to the observers line of sight. The method used above does not take into account the fact that the observable intensities from, for example, the substellar point emerge at different μ's depending on the phase. At phase 0.5 (or 0.75), when the line of centers is perpendicular to the line of sight, the substellar point is only partially visible and thus should not be weighted as heavily as the points near the terminator. The strength of the irradiation effect does not simply depend on the area of the dayside which is visible (as was assumed above) but also depends directly on the *orientation* of the observer and the dayside. Another complication results from the rotational broadening of the lines. Since rotational line broadening depends on the center-to-limb variation of the surface flux, the broadening of the synthetic spectrum must also account for the non-uniformities induced by irradiation. Obtaining this level of detail is, in theory, not difficult and will be done in the near future. Other factors, like NLTE effects are sure to play a role when analyzing high resolution spectra.

Another problem with analyzing spectra in the optical and near-IR is that this is exactly the region where the WD flux and M dwarf flux are comparable (see Fig. 5.10). Thus the shape of the pseudo-continuum is very sensitive to *all* of the

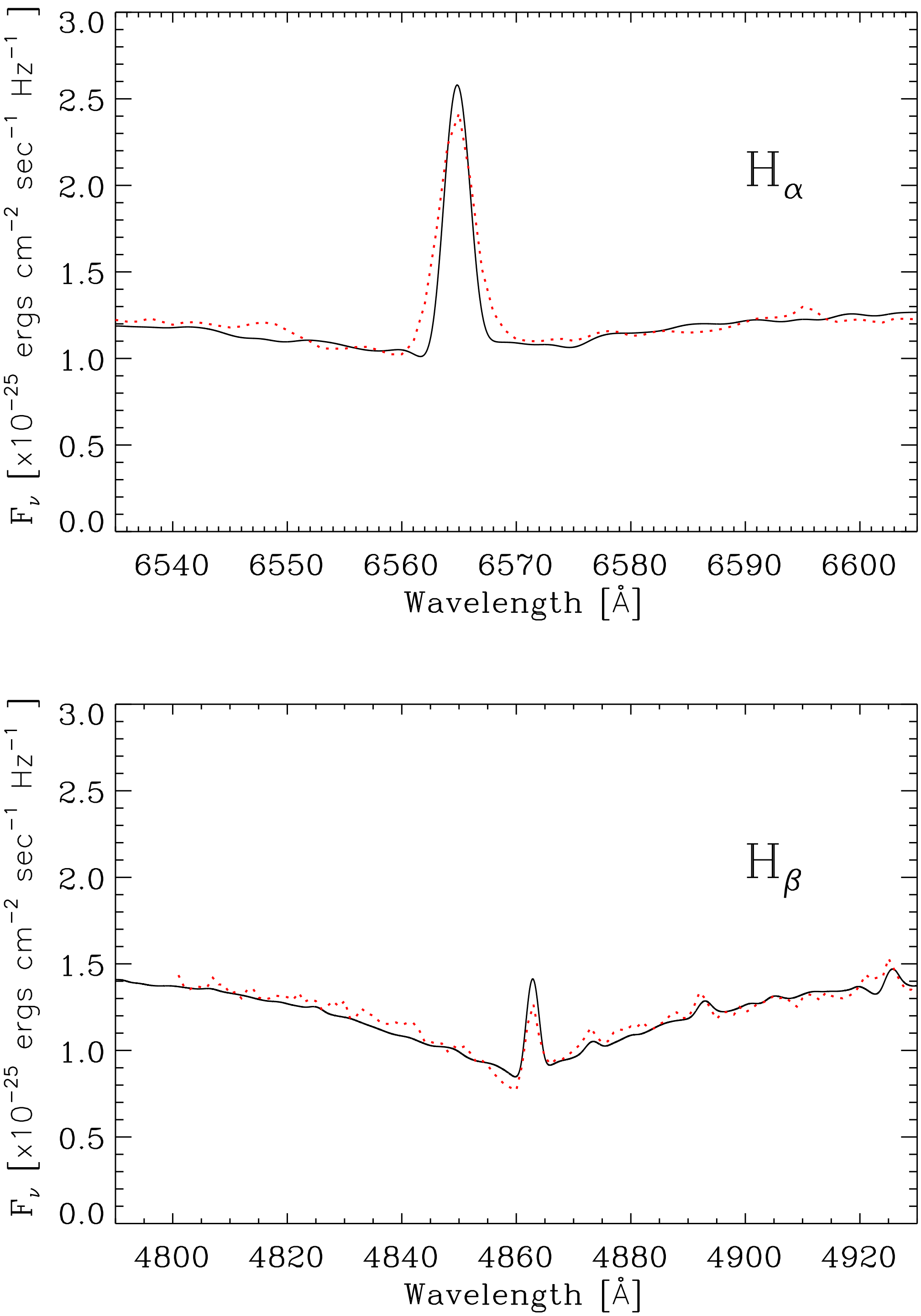

Figure 5.11: Fits to echelle spectra of GD 245 at phase 0.9 for H_α (top) and H_β (bottom). In both figures, the dotted line is the observed spectrum. The model parameters are list in table 5.2 (see text for more details).

parameters listed in table 5.2. The fact that Balmer lines from the WD flux are contaminated by the flux from the secondary reduces the accuracy of the measured effective temperature of the WD. Since the incident flux is proportional to T_{wd}^4, even small errors in T_{wd} can lead to large errors in the model of the irradiated secondary. A better approach would be to constrain the parameters of the WD with observations at UV and EUV wavelengths.

5.4 Conclusions

In agreement with earlier works (Brett & Smith, 1993; Nordlund & Vaz, 1990; Vaz & Nordlund, 1985), the models presented above demonstrate that the atmospheric structure of a pre-CV secondary undergoes dramatic changes when irradiated by a WD primary. These models also demonstrate that the changes to the structure of the secondary are sensitive to the spectral energy distribution of the incident flux and, therefore, a strong interdependence exists between the opacity sources present in the atmosphere of the secondary *and* the atmosphere of the primary. Approximating the incident flux with a blackbody spectrum not only misrepresents the spectrum of the WD, but also leads to incorrect predictions for the temperature structure of the irradiated secondary.

High resolution line-blanketed spectra have been produced for each of the atmospheric structures. These spectra clearly show that the day and night sides of the secondary can have very distinct spectra. Near the substellar point, a large temperature inversion, similar in appearance to a chromospheric transition region, forms in the upper atmosphere of the secondary. A direct consequence of this dayside temperature inversion is strong H and He emission at optical wavelengths along with many weaker emission lines due to metals. Also, many absorption features display core reversals.

The temperature increase in the upper atmosphere of the secondary is large enough to ionize many atomic species (e.g., Na and K) and dissociate important molecular opacity sources such as TiO. It is demonstrated in section 5.2 that for latitudes far from the substellar point, the temperature structure approaches that of the night side resulting in steep horizontal temperature and pressure gradients. Therefore, the strength of emission lines and changes in the chemical composition will vary across the surface. Surface inhomogeneities in the neutral Na concentration have been observed for several CV secondaries (Davey & Smith, 1992). It is now possible to model variations in the surface conditions by "patching" together multiple 1-D irradiated models (Brett & Smith, 1993).

Despite changes in the TiO absorption features, this work shows that the ratio of TiO band strengths in the near-IR remains a valuable indicator of spectral type for the secondary. In addition, it is now possible to accurately determine (or verify) the spectral type by making comparisons between the observed IR spectra from the dayside of the secondary and synthetic spectra from irradiated models.

Several authors have observed a few of the pre-CVs listed in table 1.2 at optical and near-IR wavelengths. In this part of the spectrum, a portion of both the WD continuum and the red dwarf continuum are visible. A preliminary comparison made between synthetic spectra and observed spectra for GD 245 shows very good agreement for two strong Balmer emission lines. The best fitting model parameters are in excellent agreement with those published by Schmidt et al. (1995). A more detailed modeling of the surface intensities for GD 245 will be published in a future paper along with an analysis of another pre-CV, GD 448.

The results presented in this chapter show that the conditions in irradiated objects can be inferred using synthetic spectra from irradiated models. Such models will be useful tools for furthering our understanding of PCEBs and post-CE evolution.

Chapter 6

Summary

This dissertation has focused on the effects of irradiation in stellar and substellar atmospheres. A temperature correction procedure was developed (see chapter 2) which is stable and allows energy conserving models to be produced even in the presence of strong extrinsic flux. With this temperature correction procedure and modifications to the upper boundary conditions, the `PHOENIX` atmosphere code was successfully adapted to model irradiated atmospheres and is now applicable to a wide variety of close binaries and planetary systems.

In agreement with earlier works, the models presented here demonstrate that irradiation plays a crucial role in determining the atmospheric structure and emerging spectra of extra-solar giant planets (EGPs) and of the secondaries in pre-cataclysmic variables (pre-CVs) that are located very near their primary star. This work also shows that irradiated atmospheres do not simply mimic non-irradiated atmospheres with higher effective temperatures and that it is crucial to explicitly include the extrinsic flux in the energy budget when solving a model atmosphere problem for irradiated objects.

Unlike previous work, the models presented here include the most up-to-date opacity sources and physics relevant to cool stellar and substellar irradiated atmospheres. The incident flux, taken from detailed atmosphere calculations which reproduce observed stars very well, is explicitly included in the solution of the radiative transfer equation for irradiated atmospheres. The resulting synthetic spectra are of sufficient detail and resolution to be directly compared to observations of irradiated objects. In the following sections, the results for EGPs and pre-CV secondaries are summarized and the prospects for future work are outlined.

6.1 Extrasolar Giant Planets

A large portion of this dissertation (see chapters 3 and 4) concerned the properties of giant planets (the size of Jupiter or larger) orbiting either a cool M dwarf star or a solar type star. EGPs with cool M dwarf primaries are not likely to show any observable effects due to irradiation unless they are found in very small orbits ($a < 0.05$AU). Therefore, objects like Gl 876b, which orbits a dM4 at 0.2 AU, will appear similar to an isolated Brown Dwarf or Jovian planet and will exhibit many deep molecular absorption features. However, planets that orbit solar type stars will have atmospheres significantly altered by irradiation even for orbits out to 1 AU.

The atmospheric conditions in EGPs strongly depend on the opacity sources present. In chapter 3, the effect of irradiation was tested for two limiting cases: efficient dust settling accounting for the depletion of elements by condensation (Cond) and complete cloud coverage (Dusty). Both Cond and Dusty models exhibit large amounts of reflected flux at optical wavelengths. The reflection in Dusty models is due to Mie scattering in the upper atmopshere and, therefore, many of the absorption features present in the incident spectrum will be present in the reflected sepctrum. On the contrary, reflection in Cond models is due to Rayleigh scattering throughout the atmosphere. Therefore, in cloud free atmospheres, the reflected light depends on the conditions deep within the atmosphere and, generally, will not resemble the incident spectrum. In either case, the reflected light makes the dayside of short period EGPs appear many orders of magnitude brighter than the nightside at optical wavelengths – a property that is currently being exploited by observers. The strong molecular bands (H_2O and CH_4) seen in the IR spectrum of Jovian planets and isolated BDs are greatly diminished on the dayside of planets located within 0.1AU from a solar type primary. The disappearance of molecular absorption features is due to the formation of a nearly isothermal structure and is not due to a depletion of water or methane in the atmosphere.

At small orbital separations ($a < 1$ AU), the inner layers of cloud free atmospheres experience considerable heating and a suppression of the radiative-convective boundary. However, the innermost layers of the Dusty models are essentially unaffected by the irradiation even for close orbits. The heating of the inner layers in the Cond limit can bring the temperatures at the bottom of the atmosphere close to those in the Dusty limit. This would suggest that, in certain situations, interior models would no longer depend on the Dust-Cond uncertainty discussed by Chabrier et al. (2000).

The comparison made in chapter 2, between a Cond model and the structure of Jupiter obtained by the Galileo probe, indicates the level of accuracy obtained in the Cond limit. Although the inner atmosphere ($P_{gas} > 0.1$ bars) is very well reproduced by an *isolated* Cond model, an irradiated Cond model only reproduces the upper atmosphere ($10^{-6} < P_{gas} < 10^{-2}$ bars) and is too hot at deeper layers. This discrepancy between the irradiated cond model and the Galileo data is not too surprising since Jupiter obviously has cloud coverage and these clouds are *not* homogeneously distributed over the surface. Unlike our simplified Dusty models, clouds form in thin decks and any condensation occurring at the uppermost layers would soon "rain" out onto the lower atmosphere possibly instigating a cascade of diffusive settling (Encrenaz, 1999). Until a self-consistent treatment of gravitational settling has been added to `PHOENIX`, the Cond and Dusty models should, at least, constrain the properties of irradiated EGPs.

Material in cool stellar and substellar atmospheres is often assumed to be in local thermodynamic equilibrium (LTE). However, neutral Na in the upper atmosphere of irradiated EGPs is far from being in LTE even when an upper limit is placed on the collisional rates (see chapter 4). For planets that transit their parent star, it is possible to measure additional absorption in the stellar light that is transmitted through the planet's limb. Such observations will be very sensitive to the conditions in the upper atmosphere of irradiated EGP where departures from LTE are greatest. The results presented in chapter 4 suggest that recent HST observations of Na absorption in the limb of HD209458b may be explained by non-LTE effects.

6.2 PRE-CVs

Pre-CVs were also modeled with `PHOENIX`. The results presented in chapter 5 demonstrate that dramatic changes occur in the atmosphere of a pre-CV secondary due to the incident flux from a WD primary. A very large temperature inversion, similar in appearance to a chromospheric transition region, forms in the upper atmosphere of the secondary. Also, the atmospheric extension of an M dwarf located 1 $R_\odot$ from a hot white dwarf will increase by nearly a factor of 3 (for $\log(g) = 4.5$) compared to a similar isolated M dwarf.

Ionization of atomic species and dissociation of molecules (e.g., Na, K, and TiO) in the dayside atmosphere are direct consequences of the large increase in temperature. These effects vary across the surface of the secondary leading to distinct spectra at different orbital phases and inclinations. The spectrum of the dayside exhibits many emission lines and reduced equivalent widths of atomic and molecular absorption features. Unlike EGPs, the changes to spectral features are primarily due to the temperature inversion and, in many cases, a reduction in concentration of the species responsible for the feature. This work has also demonstrated that, despite changes in the TiO absorption features induced by irradiation, the ratio of TiO band strengths remains a valuable indicator of spectral type for the secondary.

Because pre-CVs are much brighter and easier to observe than EGPs, the accuracy of the models can be tested by making direct comparisons between synthetic and real spectra. An object well suited for testing purposes is GD 245, a fairly bright short period pre-CV containing a 22,000K WD and a cool ~dM4 secondary. The orbital separation for GD 245 is ~ 1 $R_\odot$ and prominent irradiation induced emission lines have been detected by several observers (Schultz et al., 1993; Schmidt et al., 1995). In order to model the flux from the combined WD+dM system for arbitrary inclinations and phase, a grid of irradiated spherically symmetric models was produced to simulate the nonuniform heating of the secondary's surface. The grid of models (see fig. 5.9) demonstrates that the temperature inversion decreases near the day-night border and that steep pressure and temperature gradients form on the surface of irradiated secondaries.

A synthetic spectrum for the pre-CV binary system was constructed, accounting for the fraction of the day and night side visible to an observer, using the fluxes from the model grid, a non-irradiated M dwarf model, and a WD model (see section 5.2). This synthetic spectrum was then compared to the two most prominent hydrogen emission lines (H_α and H_β) observed at phase 0.9. The fit (see fig. 5.11) was extremely good and, within the error bars, confirms the results of Schmidt et al. (1995). The ability to fit the observations of GD 245 indicates that irradiation effects are well modeled by `PHOENIX`. However, there are several improvements that need to be made to the models before a detailed analysis of GD 245 is carried out. The construction of the synthetic spectrum can be improved by a better mapping of the surface intensities and non-LTE effects should be included. Also, the lines are broadened due to large rotational velocities. Since rotational line broadening depends on the variation of surface intensities (usually due to limb darkening for isolated stars), the broadening of lines originating from the illuminated face of the secondary will be affected by limb *brightening*.

6.3 Future Work

As mentioned in the introduction, a self-consistent evolution model for irradiated EGPs has yet to be calculated. The atmospheric structure regulates the release of energy from a stellar or substellar object and sets the upper boundary condition for models of the interior. Therefore, evolution calculations for the secondary in close binaries must use atmospheric models which correctly account for irradiation. As demonstrated in chapter 3 (and for pre-CVs in chapter 5), if the extrinsic flux penetrates deep enough, the inner adiabatic temperature gradient will change corresponding to a different entropy in the interior. Such changes in the deep layers of the atmosphere will slow the cooling rate and corresponding contraction of EGPs as they evolve (Guillot et al., 1996). The extent to which the interior is insulated depends on the strength of the incident radiation which, in turn, depends on the orbital separation. Therefore, migration from large to small orbital separations will also affect the evolution of EGPs. In order to test these ideas, Baraffe et al. (2002) are currently working on evolution calculations which make use of irradiated models produced by `PHOENIX`.

The rapid development of new techniques and instruments will soon allow detailed observations of EGP atmospheres. The interpretation of these observations will benefit greatly from detailed model atmosphere calculations such as those presented here. However, transmitted and phase dependent spectra for the wide variety of EGPs listed in table 1.1 need to be produced. Modeling phase dependent spectra will require the development of detailed surface intensity maps that predict the day to night variation in the thermal and reflected spectrum.

Non-LTE effects should be explored further in both EGP and pre-CV atmospheres for a large number of atomic and molecular species. Large non-LTE effects could significantly alter the structure of the upper atmosphere and, therefore, alter the appearance of many spectral lines. Also, a solar metal abundance has been assumed for each of the models in this work. A reduced metal abundance would allow the UV-EUV radiation to penetrate deeper into the atmosphere resulting in a greater suppression of the radiative-convective boundary. Also, as mentioned in chapter 4, photoionization would extend deeper into the atmosphere. An increased metallicity would likely have the opposite effect. Such changes could alter the temperature and pressure at the bottom of the atmosphere and consequently affect evolution calculations in a similar manner as mentioned above.

Many of the PCEBs listed in table 1.2 have already been observed, and the analysis of this data would benefit greatly from models similar to those presented in chapter 5. The effects of meridional circulations and zonal flows on the surface of irradiated M dwarfs can also be tested by making comparisons between model grids that sample many latitudes on the irradiated surface (like that produced for GD 245) and observations which measure inhomogeneities in the surface abundance of Na (Davey & Smith, 1992).

A number of other close binary systems have measurable effects due to irradiation. As mentioned in chapter 5, non-magnetic CVs have luminous accretion disks and magnetic CVs have bright spots on the WD surface that can exceed 100,000K. Therefore, CVs are interesting systems for studying the effects of irradiation by a complex source. The changes induced on the M dwarf surface by the intense irradiation during a nova event should be explored. Algol binaries and Symbiotic stars are additional examples of stellar systems where irradiation and reflection effects are observed. Also, the giant planets in our own solar system currently provide the best observations of irradiated giant planets. The high quality data taken by the

Galileo probe provides an excellent opportunity to compare irradiated atmospheric models simultaneously to observed spectra *and* observed structure data. Jupiter is the only object, stellar or substellar, for which such a dual comparison is possible. The other gas giants in our solar system (Neptune, Uranus, and Saturn) should also be modeled.

This dissertation has only studied a small number of the many interesting phenomena that exist in the strongly irradiated atmospheres of EGPs and pre-CV secondaries. A great deal of work remains to be done for these objects and many other types of close binary systems. The limitations of models, the questions that remain unanswered, and the exciting new observations only amplify the rewarding nature of this field.

Bibliography

Allard, F., Hauschildt, P. H., Alexander, D. R., Tamanai, A., & Schweitzer, A. 2001, ApJ, 556, 357

Allard, F., Hauschildt, P. H., & Schwenke, D. 2000, ApJ, 540, 1005

Allen, C. W. 1973, Astrophysical Quantities, 3rd edn. (London: Athlone Press)

Andretta, V., Doyle, J. G., & Byrne, P. B. 1997, A&A, 322, 266

Appleby, J. F. 1990, Icarus, 85, 355

Auer, L. H. 1971, JQSRT, 11, 573

Baraffe, I., Chabrier, G., Allard, F., Barman, T., & Hauschildt, P. 2002, in prep.

Barman, T. S., Hauschildt, P. H., & Allard, F. 2001, ApJ, 556, 885

Barman, T. S., Hauschildt, P. H., Short, C. I., & Baron, E. 2000, ApJ, 537, 946

Bautista, M. A., Romano, P., & Pradhan, A. K. 1998, ApJS, 118, 259

Borysow, A. & Frommhold, L. 1986a, ApJ, 311, 1043

—. 1986b, ApJ, 303, 495

—. 1986c, ApJ, 304, 849

—. 1987a, A&A, 320, 437

—. 1987b, ApJ, 318, 940

Borysow, A., Jorgensen, U. G., & Cheng. 1997a, A&A, 324, 185

—. 1997b, A&A, 324, 185

Borysow, A. & Tang. 1993, Icarus, 105, 175

Brett, J. M. & Smith, R. C. 1993, MNRAS, 264, 641

Brown, T. M., Charbonneau, D., Gilliland, R. L., Noyes, R. W., & Burrows, A. 2001, ApJ, 552, 699

Bruls, J. H. M. J., Rutten, R. J., & Shchukina, N. G. 1992, A&A, 265, 237

Burrows, A., Hubbard, W. B., Lunine, J. I., & Liebert, J. 2001, Review of Modern Physics, 73, 719

Butler, R. P., Marcy, G. W., Fischer, D. A., Vogt, S. S., Tinney, C. G., Jones, H. R. A., Penny, A. J., & Apps, K. 2001, in Planetary Systems in the Universe: Observations, Formation and Evolution, in press

Cameron, A., Horne, K., Penny, A., & James, D. 1999, Nature, 402, 751

Cannon, C. J. 1973, ApJ, 185, 621

Catalán, M. S., Schwope, A. D., & Smith, R. C. 1999, MNRAS, 310, 123

Chabrier, G., Baraffe, I., Allard, F., & Hauschildt, P. 2000, ApJ, 542, 464

Charbonneau, D., Brown, T. M., Latham, D. W., & Mayor, M. 2000, ApJ, 529, L45

Charbonneau, D., Brown, T. M., Noyes, R. W., & Gilliland, R. L. 2002, ApJ, in press

Charbonneau, D., Noyes, R. W., Korzennik, S. G., Nisenson, P., Jha, S., Vogt, S. S., & Kibrick, R. I. 1999, ApJ, 522, L145

Chase, M. W., Davis, C. A., Downey, J. R., Frurip, D. J., McDonald, R. A., & Syverud, A. N. 1985, J. Phys. Chem. Ref. Data, 14, Sup.1

Claret, A. & Gimenez, A. 1992, A&A, 256, 572

Davey, S. & Smith, R. C. 1992, MNRAS, 257, 476

de Kool, M. & Ritter, H. 1993, A&A, 267, 397

Delfosse, X., Forveille, T., Beuzit, J. ., Udry, S., Mayor, M., & Perrier, C. 1999, A&A, 344, 897

Drawin, H. W. 1961, Zs. f. Phys., 164, 513

Eddington, A. S. 1926, MNRAS, 86, 320

Encrenaz, T. 1999, A&A Rev., 9, 171

Goukenleuque, C., Bézard, B., Joguet, B., Lellouch, E., & Freedman, R. 2000, Icarus, 143, 308

Grossman, L. 1972, Geochim. Cosmochim. Acta, 38, 47

Gruszka, M. & Borysow, A. 1997, Icarus, 129, 172

Guillot, T. 2000, in IAU Symposium, Vol. 202, E19

Guillot, T., Burrows, A., Hubbard, W. B., Lunine, J. I., & Saumon, D. 1996, ApJ, 459, L35

Guillot, T. & Showman, A. 2002, A&A, in press

Gustafsson, B., Bell, R. A., Eriksson, K., & Nordlund, A. 1975, A&A, 42, 407

Hauschildt, P. H. 1992, JQSRT, 47, 433

Hauschildt, P. H., Allard, F., Alexander, D. R., & Baron, E. 1997, ApJ, 488, 428

Hauschildt, P. H., Allard, F., & Baron, E. 1999, ApJ, 512, 377

Hauschildt, P. H. & Baron, E. 1999, JCAM, 102, 41

Henry, G. W., Marcy, G. W., Butler, R. P., & Vogt, S. S. 2000, ApJ, 529, L41

Henry, T. J. 1998, in ASP Conf. Ser. 134: Brown Dwarfs and Extrasolar Planets, 28

Hickey, M. P., Walterscheid, R. L., & Schubert, G. 2000, Icarus, 148, 266

Hillwig, T. C., Honeycutt, R. K., & Robertson, J. W. 2000, AJ, 120, 1113

Hubeny, I. 1988, Computer Physics Comm., 52, 103

Husson, N., Bonnet, B., Scott, N., & A., C. 1992, JQSRT, 48, 509

Jørgensen, U. G. 1994, A&A, 284, 179

Koch, D., Borucki, W., Webster, L., Jenkins, J., Dunham, E., Jordan, S., & The Kepler Team. 2001, in Astronomische Gesellschaft Meeting Abstracts, Vol. 18, 406

Kurucz, R. L. 1993, Molecular Data for Opacity Calculations, Kurucz CD-ROM No. 15

—. 1994, Atomic Data for Fe and Ni, Kurucz CD-ROM No. 22

Kurucz, R. L. 1996, in ASP Conf. Ser. 108: M.A.S.S., Model Atmospheres and Spectrum Synthesis, 160

Kurucz, R. L. & Bell, B. 1995, Atomic Line List, Kurucz CD-ROM No. 23

Leggett, S. K., Allard, F., Dahn, C., Hauschildt, P. H., Kerr, T. H., & Rayner, J. 2000, ApJ, 535, 965

Lucy, L. B. 1964, in Harvard-Smithsonian Conference on Stellar Atmospheres, Proceedings of the First Harvard-Smithsonian Conference on Stellar Atmospheres (Smithsonian Astrophysical Observatory), 53

Marcy, G. W., Butler, R. P., Fischer, S. A., & Vogt, S. S. 2000, in IAU Symposium, Vol. 202

Marcy, G. W., Butler, R. P., Vogt, S. S., Fischer, D., & Lissauer, J. J. 1998, ApJ, 505, L147

Marley, M. S., Gelino, C., Stephens, D., Lunine, J. I., & Freedman, R. 1999, ApJ, 513, 879

Marsh, T. R. 1990, ApJ, 357, 621

—. 2000, New Astronomy Review, 44, 119

Marsh, T. R. & Duck, S. R. 1996, MNRAS, 278, 565

Mathisen, R. 1984, Photo Cross-sections for Stellar Atmosphere Calculations — Compilation of References and Data, Inst. of Theoret. Astrophys. Univ. of Oslo, Publ. Series No. 1.

Maxted, P. F. L., Marsh, T. R., Moran, C., Dhillon, V. S., & Hilditch, R. W. 1998, MNRAS, 300, 1225

Mayor, M. & Queloz, D. 1995, Nature, 378, 355

Mazeh, T., Naef, D., Torres, G., Latham, D. W., Mayor, M., Beuzit, J., Brown, T. M., Buchhave, L., Burnet, M., Carney, B. W., Charbonneau, D., Drukier, G. A., Laird, J. B., Pepe, F., Perrier, C., Queloz, D., Santos, N. C., Sivan, J., Udry, S. ., & Zucker, S. 2000, ApJ, 532, L55

Mihalas, D. 1970, Stellar Atmospheres, 1st edn. (New York: W.H. Freeman)

Nisenson, P. & Papaliolios, C. 2001, ApJ, 548, L201

Nordlund, A. & Vaz, L. P. R. 1990, A&A, 228, 231

Ollivier, M., Mariotti, J., Sekulic, P., Michel, G., Leger, A. M., Bouchareine, P., Brunaud, J., Coude du Foresto, V., Mennesson, B. P., Borde, P. J., Amy-Klein, A., Vanlerberghe, A., Lagage, P., Artzner, G. E., & Malbet, F. 2000, in Proc. SPIE Vol. 4006, p. 354-358, Interferometry in Optical Astronomy, Pierre J. Lena; Andreas Quirrenbach; Eds., Vol. 4006, 354–358

Olson, G. & Kunasz, P. 1987, JQSRT, 38, 325

Oppenheimer, B. R., Kulkarni, S. R., Matthews, K., & Nakajima, T. 1995, Science, 270, 1478

Orosz, J. A. & Hauschildt, P. H. 2000, A&A, 364, 265

Orosz, J. A., Wade, R. A., Harlow, J. J. B., Thorstensen, J. R., Taylor, C. J., & Eracleous, M. 1999, AJ, 117, 1598

Paczynski, B. 1976, in IAU Symp. 73: Structure and Evolution of Close Binary Systems, Vol. 73, 75+

Partridge, H. & Schwenke, D. W. 1997, J. Chem. Phys., 106, 4618

Perryman, M. A. C. 2000, Reports of Progress in Physics, 63, 1209

Ragent, B., Colburn, D. S., Rages, K. A., Knight, T. C. D., Avrin, P., Orton, G. S., Yanamandra-Fisher, P. A., & Grams, G. W. 1998, J.Geophys.Res., 103, 22891

Ritter, H. & Kolb, U. 1998, A&AS, 129, 83

Rothman, L. S., Gamache, R. R., Tipping, R. H., Rinsland, C. P., Smith, M. A. H., Chris Benner, D., Malathy Devi, V., Flaub, J.-M., Camy-Peyret, C., Perrin, A., Goldman, A., Massie, S. T., Brown, L., & Toth, R. A. 1992, JQSRT, 48, 469

Rybicki, G. B. & Hummer, D. G. 1991, A&A, 245, 171

Samuelson, R. E., Nath, N., & Borysow, A. 1997, Planetary & Space Sciences, 45/8, 959

Saumon, D., Hubbard, W. B., Burrows, A., Guillot, T., Lunine, J. I., & Chabrier, G. 1996, ApJ, 460, 993

Schmidt, G. D., Smith, P. S., Harvey, D. A., & Grauer, A. D. 1995, AJ, 110, 398

Schubert, G., Hickey, M. P., & Walterscheid, R. L. 2001, AAS/Division for Planetary Sciences Meeting, 33

Schultz, G., Zuckerman, B., Becklin, E. E., & Barnbaum, C. 1993, American Astronomical Society Meeting, 25, 824

Schwank, M., Schmutz, W., & Nussbaumer, H. 1997, A&A, 319, 166

Schweitzer, A. 1995, Master's thesis, M.A. thesis, Univ. Heidelberg (1995)

—. 1999, Ph.D. Thesis

Schweitzer, A., Hauschildt, P. H., Allard, F., & Basri, G. 1996, MNRAS, 283, 821

Schweitzer, A., Hauschildt, P. H., & Baron, E. 2000, ApJ, 541, 1004

Schwenke, D. W. 1998, Chemistry and Physics of Molecules and Grains in Space. Faraday Discussion, 109, 321

Seager, S. & Sasselov, D. D. 1998, ApJ, 502, L157

—. 2000, ApJ, 537, 916

Seager, S., Whitney, B. A., & Sasselov, D. D. 2000, ApJ, 540, 504

Stromovsky, L. A., Collard, A. D., Fry, P. M., Orton, G. S., Lemmon, M. T., Tomasko, M. G., & Freedman, R. S. 1998, J.Geophys.Res., 103, 22929

Sudarsky, D., Burrows, A., & Pinto, P. 2000, ApJ, 538, 885

Tytler, D. & Rubenstein, E. 1989, in IAU Colloq. 114: White Dwarfs, 524

Unwin, S. C. & Shao, M. 2000, in Proc. SPIE Vol. 4006, p. 754-761, Interferometry in Optical Astronomy, Pierre J. Lena; Andreas Quirrenbach; Eds., Vol. 4006, 754–761

Van Regemorter, H. 1962, ApJ, 136, 906

Vaz, L. P. R. 1985, Ap&SS, 113, 349

Vaz, L. P. R. & Nordlund, A. 1985, A&A, 147, 281

Verner, D. A. & Yakovlev, D. G. 1995, A&AS, 109, 125

Wade, R. A. & Horne, K. 1988, ApJ, 324, 411

Wilson, R. E. 1990, ApJ, 356, 613

Wolszczan, A. & Frail, D. A. 1992, Nature, 355, 145

Young, P. & Schneider, D. P. 1981, ApJ, 247, 960